

Nano-Biophotonics

Submitted by Natalie Garrett

to the University of Exeter
as a thesis for the degree of

Doctor of Philosophy in Physics

April 2010

This thesis is available for Library use on the understanding that it is copyright material and that no quotation from the thesis may be published without proper acknowledgment.

I certify that all material in this thesis which is not my own work has been identified and that no material has previously been submitted and approved for the award of a degree by this or any other University.

.....

Natalie Garrett

Abstract

Photonic techniques are the methods of choice for probing biological systems, as they are non-invasive, non-ionising, inexpensive, and are ubiquitous. When applied to the treatment and prevention of disease and for pathology in general, biophotonics offers a means to bridge the gap between understanding of molecular structures and their role in physiological functions. There is a wide range of such techniques used in imaging, assaying, bio-sensing, optical diagnosis, each of which has limitations as well as benefits. The experiments outlined in this thesis use nanotechnology to overcome the limitations of resolution, contrast and chemical specificity with photonic techniques in biology.

The experimental work outlined in this thesis is divided over three chapters, the first of which is concerned with nanostructured metallic surfaces for use in surface enhanced Raman scattering (SERS) for protein assay applications. This chapter gives details of the methods used to produce and characterise SERS substrates using gold and silver thermally evaporated onto butterfly wing sections, together with the protocols developed for manufacturing biomimetic analogues of these naturally occurring nanostructures. The conjugation system designed to modify the metal surfaces for use in an avidin/biotin model protein binding assay is described, together with an account of the efficacy of the final assay. The results obtained show that such naturally occurring nanostructures, and their biomimetic analogues, are suitable for use as SERS substrates for wet protein binding assays. This work represents a major advance in the field of SERS assay.

The next experimental chapters describe experiments that use coherent Raman scattering (CRS) methods to probe the interactions between nanoparticles and live cell cultures, as well as provide chemically selective images of tissue samples. Chapter 6 gives an account of work undertaken to investigate gold nanoshells, novel nanoparticles comprising spherical silica cores surrounded by a layer of gold, whose plasmon resonance wavelength may be tuned by altering the shell thickness and core diameters. Gold nanoshells exhibit unique optical properties arising from this plasmon resonance, and their ability to rapidly heat under exposure to light at this resonant wavelength has been used for photodynamic therapy of tumours in mice, in one instance with white

blood used cells to carry gold nanoshells to the site of the tumour. Although previous photothermal experiments involving tumour destruction using nanoshells have given promising results, they largely ignored the interactions between single cells and the gold nanoshells. The experiments in this chapter probe these interactions, using coherent Raman scattering (CRS) microscopy.

CRS is a chemically-selective multiphoton modality that can be used to image live cells noninvasively and with excellent chemical specificity and contrast. To determine the extent to which CRS microscopy-induced heating of gold nanoshells would affect live cells, macrophage cells were induced to phagocytise gold nanoshells prior to exposure to CRS. A trypan blue vital staining technique was used to determine cell survival rates after exposure to a range of laser powers. The photoluminescent qualities of gold nanoshells were also exploited as a marker for phagocytosis, the rate of which was investigated using CRS, as a function of the concentration of two different H₂S donors in the cell medium.

The final experimental chapter investigates the ability of CRS to image organic nanoparticles within cells and tissues. Two varieties of nanoparticles and cell lines were used in this chapter: dendrimer/plasmid DNA nanoparticles with human skin cancer cells and apo lipoprotein E (APOE) conjugated to albumin nanoparticles with human brain endothelial cells. Dendrimer nanoparticles have been shown to exhibit characteristics that make them efficient potential candidates for gene therapy, since they are able to spontaneously bind to DNA and deliver it across cell membranes. Before this gene delivery vector is used in humans it is important to investigate the distribution of these nanoparticles as they pass inside cells, using a non-invasive imaging technique that provides sufficient spatial resolution and chemical selectivity. APOE-conjugated albumin nanoparticles have been found to cross the blood-brain barrier, and hence their uptake by brain endothelial cells is of great relevance for engineering drugs to treat brain disease.

The potential of SRS microscopy to image the blood vessels within the brain was investigated using slices of mouse brain. This provided clear images of the blood-brain barrier, a selectively permeable membrane comprising endothelial cells lining the blood vessels innervating the brain. The BBB effectively blocks access to over 95% of drugs

from entering the brain, targeted engineering of drugs to cross this barrier is necessary in order to treat diseases of the brain. Therefore, the images provided in these brain imaging experiments have demonstrated the potential for coherent Raman scattering microscopy in quantifying drug nanoparticle uptake within dosed animal brains.

The interaction between ApoE-albumin nanoparticles and brain endothelial cells was investigated in using coherent Raman scattering. Signal intensity from three stimulated Raman scattering microscopy images of endothelial cells exposed to nanoparticles was colocalised using the relative intensity of signal probing three Raman bands identified in spontaneous Raman scattering spectra of the nanoparticles. The pump wavelengths used were 813 nm, 821 nm and 938.9 nm and the Stokes wavelength was 1064 nm in each case. The data obtained showed that ApoE-albumin nanoparticle signal associated with the cells was overlapped by signal from CH₂ within the sample, indicating the involvement of lipid-rich structures within the cells in receptor membrane endocytosis.

Acknowledgements

Throughout my PhD I have been supported and encouraged by a large number of people without whose help and friendship the project would not have been so successful. Firstly, my thanks go to my supervisor, Julian Moger, for his enthusiasm, insight, support and hilarious anecdotes at conferences. His drive to establish Exeter University's Biomedical Physics group as an internationally acclaimed multiphoton imaging research centre has been truly inspirational and I am very grateful for the opportunity to work with him. Peter Winlove deserves a special mention, as the leader of my research group and my second supervisor. It seems there is no area of Physics in which he is not only an expert, but is also in possession of at least half a dozen relevant lewd anecdotes. His wealth of remarkably detailed knowledge is matched by his contagious enthusiasm for the topic – I blame him almost entirely for my decision to undertake this PhD!

I would also like to thank Ellen Green and Dick Ellis for their patience and wisdom while training me during my first forays into wet lab experimentation, and for loaning me innumerable books and obscure items of experimental paraphernalia. It is one thing to read about a technique in a book, but quite another to have such experienced experimentalists show you how it's really done. Andy Murray, James Parsons and Piers Andrew have all helped me get to grips with evaporating techniques and using the SEM as well as the darkfield flow cell, while Cierán Stewart assisted me with the AFM calibration of my samples – thanks guys! Thanks must also go to John Meakin and the workshop boys for all their help with the nuts-and-bolts of designing, maintaining and ordering kit. As a technical support team, they are second to none. Dave Colridge deserves my deep gratitude for enduring my conversation during lunch breaks, and for continually coming to my rescue whenever Microsoft Works shows itself to be an oxymoron.

I am deeply indebted to several collaborators for all their help. Evgeny Sirotkin, Pete Vukusic and Feodor Ogrin were excellent collaborators for the butterfly wing paper. Maria de la Fuente of the London School of Pharmacy gave me excellent training in cell culture and has gone above and beyond the call of duty to supply me with materials, including dendrimer nanoparticles, plasmid DNA and skin cancer cell lines. She has

cycled to work through snow drifts and even when ill, all to make sure my reagents would be posted on time. Thank you, Maria! Special thanks must also go to Larisa Mihoreanu and David Begley of Kings College London for their advice, good humoured support and the numerous samples they've supplied me with. Other scientists who have very kindly supplied me with samples are Alex Kendall (thank you for the LPS!) and Matt Whiteman (thank you for the NaHS and GYY4137) both of Exeter's Peninsula College of Medicine and Dentistry (PCMD).

I was very grateful to receive support from Mohit Chopra (also from PCMD) for cryogenically storing my cell lines under liquid nitrogen. Without his help in this respect, my cell culturing experiments would have been nigh on impossible and I wouldn't have had the opportunity to pretend that Martin Smith and I were characters in Jurassic Park. Thanks also to John Hale, who teamed with Martin to provide the ultimate cautionary tale to all Physics PhD students – you guys have left very big shoes to fill (metaphorically anyway). And a noose (literally).

GP forever has my gratitude for our innumerable fascinating and inspirational discussions during our mentor meetings. He has taught me many things, but one lesson in particular will stay with me forever: I shall never attempt to make grape jam in a pressure cooker. I must also give my thanks to: the motley crew of PhD students in the Biomedical Physics research group (past and present), the late-night workers, the Christmas “meeting”/Summer ball jesters, the coffee-time philosophers and the Friday pub gang, who have all helped to make my time here at Exeter very enjoyable and “educational”. Thanks to the photonics crew for welcoming me with open arms and readily proffered Rubik's cubes, iPhones and crosswords. In particular, thanks to Tom Constant for preventing my auto-defenestration. You happy now, Tom?

My family has given me a great deal of support throughout my PhD and I owe them a great debt of thanks; in some cases I also owe a great debt of money. In particular, my lovely husband Simon has been wonderfully supportive, and I thank him from the bottom of my heart. Si – without you, not only would this thesis not have been possible, but not much else that I cherish in life would be possible either. With a love that will echo through the ages, Simon, I dedicate this thesis to you!

List of Abbreviations

CARS – coherent anti-Stokes Raman scattering
CRS – coherent Raman scattering
DMEM – Dulbecco’s modified Eagle’s medium
DMSO – dimethyl sulphoxide
DPBS – Dulbecco’s phosphate buffered saline
EDC - ethyl dimethylaminopropyl carbodiimide
EDTA - ethylenediaminetetraacetic acid
ELISA - enzyme-linked immunosorbent assays
EM – electromagnetic
FBS – foetal bovine serum
FWM – four wave mixing
GNS – gold nanoshells
LSP – localised surface plasmon
MPA – 3-mercaptopropanoic acid
NHS – N-hydroxy succinimide
NIR – near infrared
OPO – optical parametric oscillator
PBS – phosphate buffered saline
PMMA - poly(methyl methacrylate)
SAM – self assembled monolayer
SEM – scanning electron microscope
SERDS – shifted excitation Raman difference spectroscopy
SERS – surface enhanced Raman spectroscopy
SPP – surface plasmon polariton
SRG – stimulated Raman gain
SRL – stimulated Raman loss
SRS – stimulated Raman scattering
TEM – transmission electron microscope

Table of Contents

Nano-Biophotonics	1
Abstract.....	2
Acknowledgements.....	5
List of Abbreviations	7
Table of Contents.....	8
List of Figures	11
1. Introduction	15
1.1. The History of Photonics in Biology	15
1.2. Emerging Photonic Techniques in Biology.....	27
1.2.1. Coherent Raman Scattering	27
1.3. Thesis Aims.....	28
1.4. Overview of Thesis.....	29
2. Background and Literature Review of Raman-based Biophotonics	31
2.1. Nanotechnology in Biophotonics.....	31
2.2. General Cell Structure.....	35
2.3. Chemical Assay.....	36
2.4. Raman Scattering	39
2.5. Surface Enhanced Raman Scattering	42
2.6. SERS Substrates.....	45
2.6.1. Gold Nanoshells	48
2.7. Coherent Raman Scattering.....	51
2.8. Contribution of this Thesis to the field	56
3. Theory	57
3.1. Theory of Raman Scattering.....	57
3.2. Surface Enhanced Raman Scattering Theory.....	62
3.2.1. Electromagnetic Contribution to Surface Enhanced Scattering	62
3.2.2. Chemical Enhancement in SERS.....	64
3.3. Photoluminescence.....	65
3.4. Plasmon Wavelength Tuning in Gold Nanoshells	66
3.4.1. Dielectric Function of Particles of Gold in the Mie Regime	66
3.4.2. Absorption, Scattering and Extinction	69

3.5. Coherent Raman Scattering	70
3.5.1. CARS Theory	70
3.5.2. Stimulated Raman Scattering Theory	79
3.5.3. Application of CRS to Biophotonics	82
4. Instrumentation	83
4.1. Raman Laser Microspectrometer	83
4.2. Coherent Raman Scattering Setup.....	84
4.3. Spectrometer	91
4.4. Metal Evaporators	92
4.5. Scanning Electron Microscope.....	93
4.6. Ultraviolet Curing System	93
4.7. Cell Culture.....	94
5. Surface Enhanced Raman Scattering Using Biological & Biomimetic Nanostructures.....	95
5.1. SERS Protein Assays	95
5.2. Materials and Methods.....	98
5.2.1. Preparation of natural nanostructure substrates.....	99
5.2.2. Fabrication of biomimetic nanostructures	102
5.2.3. Imaging and Spectroscopy	102
5.2.4. Thiophenol Monolayers.....	102
5.2.5. Bioconjugation for Model “Immunoassay” System.....	103
5.3. Results.....	106
5.3.1. SEM Imaging of Substrates	106
5.3.2. Enhancement factors	108
5.3.3. Bioconjugation	111
5.3.4. Normal Raman Spectra	113
5.3.5. SERS Assay.....	114
5.4. Discussion and Conclusions	116
6. Biophotonic Applications of Gold Nanoshells.....	118
6.1. Introduction	118
6.1.1. Nanoshells in Photodynamic Therapy.....	118
6.1.2. Photoluminescence of Nanoshells.....	119
6.1.3. Nanoshells in this Thesis	120
6.2. Experimental	120
6.2.1. Manufacturing Process of Metal Nanoshells.....	120
6.2.2. Characterisation of Gold Nanoshells by SEM.....	121

6.2.3. Determining the Plasmon Characteristics of aged Nanoshells	122
6.2.4. Verifying CARS Signal/Enhancement from Gold Nanoshells	127
6.2.5. Mouse Macrophage Cell Culturing Protocols	128
6.2.6. Cell Counting and Viability Staining Methods.....	130
6.2.7. Nanoshells as Contrast for CARS Microscopy	134
6.2.8. Ablation Study.....	136
6.2.9. Monitoring the Effects of Hydrogen Sulphide on Phagocytosis using GNS Contrast	138
6.3. Discussion and Conclusions	143
7. Label-free Imaging of Organic Nanoparticles	148
7.1. Introduction	148
7.2. Experimental	151
7.2.1. Comparison of Brain Tissues with SRS and CARS.....	151
7.2.2. Brain Cell Culturing Protocols	156
7.2.3. Albumin Nanoparticles.....	156
7.2.1. Cancer Cell Culturing Protocols.....	164
7.2.2. Dendrimer Nanoparticles.....	164
7.3. Discussion and Conclusions	172
8. Conclusions and Suggestions for Further Work.....	176
8.1. SERS Using Biological and Biomimetic Nanostructures	177
8.1.1. Summary	177
8.1.2. Future Work.....	178
8.2. Biophotonic Applications of Gold Nanoshells.....	180
8.2.1. Summary	180
8.2.2. Future Work.....	182
8.3. Label-free Imaging of Organic Nanoparticles	182
8.3.1. Summary	182
8.3.2. Future Work.....	183
9. References	185
10. Publications, Conference Proceedings & Academic Achievements.....	200
Publications.....	200
Conference Proceedings	200
Academic Achievements.....	201

List of Figures

Fig. 1.1 Depth of field ranges for lenses of high and low numerical apertures [5].	18
Fig. 1.2 The anatomy of an animal cell [7]	19
Fig. 1.3 Schematic cross-sectional structure of the cell membrane [8]	20
Fig. 1.4 Endothelial cells under the microscope. Nuclei are stained blue with DAPI, microtubules are marked green by an antibody and actin filaments are labelled red with phalloidin [12].	22
Fig. 1.5 A schematic diagram of a confocal microscope [14]	23
Fig. 1.6 White light microscopy images of an animal cell. (A) was imaged using bright-field optics, (B) with phase-contrast optics and (C) was imaged with differential interference-contrast optics [15]	24
Fig. 1.7 Comparison of images produced with TEM and SEM [16]	25
Fig. 2.1 A schematic diagram of an antibody [39]	38
Fig. 2.2 Spontaneous Raman spectrum of the P22 virus, exhibiting the characteristic Raman modes typically observed in biological samples [44]	41
Fig. 2.3 Molecular energy level schematic for CARS and SRS depicting the interaction between the pump (ω_p), Stokes (ω_s) and anti-Stokes (ω_{AS}) beams. The dashed lines denote virtual states while the energy difference between the ground state ($V=0$) and first excited state ($V=1$) corresponds to a Raman resonance (Ω_R).	53
Fig. 3.1 Extinction spectra of nanoshells with varying shell thicknesses [95].	69
Fig. 3.2 The resonant, non-resonant and mixed contributions to the CARS signal as a function of detuning Δ , calculated using the equations in section 3.5.1, with a Lorentzian bandwidth Γ of 10 cm^{-1} .	74
Fig. 3.3 The overall CARS signal intensity as a function of detuning Δ , calculated using the equations in section 3.5.1, with a Lorentzian bandwidth Γ of 10 cm^{-1} .	75
Fig. 3.4 Energy level diagram for (a) spontaneous Stokes Raman scattering, (b) general four wave mixing processes, (c) SRS, (d) resonant CARS, (e) nonresonant CARS from an electronic contribution, (f) the phase matching condition in CARS. The dashed lines denote virtual vibrational states.	77
Fig. 3.5 Spectral profile for SRS, adapted from [112]	81
Fig. 4.1 The Coherent Raman scattering system at the University of Exeter.	85
Fig. 4.2 Schematic diagram of the CARS microscope [138]	86
Fig. 4.3 Schematic diagram of the optical bench	87
Fig. 4.4 Transmission profile for Chroma Z850rdc-xr long pass dichroic filter, data supplied by the manufacturers	88
Fig. 4.7 Custom-built SRS detector	91
Fig. 4.8 Transmission of the grating in CARS spectrometer, data supplied by manufacturers.	92

Fig. 5.1 Schematic diagram illustrating the formation of a self assembled monolayer (SAM) of thiophenol on a gold surface.	99
Fig. 5.2 Regions of interest on <i>Graphium weiskei</i> butterfly wings.....	101
Fig. 5.3 A schematic diagram depicting the chemical conformation of <i>gauche</i> and <i>trans</i> configurations of 3-mercaptopropanoic acid and cysteamine.	105
Fig. 5.4 SEM images of: the <i>G. weiskei</i> nano-cone arrays (A) and the biomimetic substrate (B), with nano-cone heights of 524nm peak-to-peak distances of 390nm.	107
Fig. 5.4 SEM images of green regions on <i>G. weiskei</i>	108
Fig. 5.5 SERS spectra of a thiophenol monolayer on a butterfly wing coated with 70nm silver (left) and an un-enhanced Raman spectrum of neat thiophenol in solution (right).....	109
Fig. 5.6 Enhancement factor of metalized wing nanostructures as a function of metal deposition thickness: ■ data points correspond with silver, ▲ with gold.	110
Fig. 5.7 Graph depicting SERS spectra of MPA on gold-coated butterfly wings as a function of deposition times. The red, black and blue lines correspond with deposition times of 1 hour, 2 hours and 18 hours respectively.....	112
Fig. 5.8 SERS spectra of MPA a) prior to activation with EDC/NHS, b) after activation	112
Fig. 5.9 SERS spectra of avidin bound to gold-coated wing (b) and the avidin-biotin complex bound to gold-coated wing (a).	113
Fig. 5.10 SERS spectra of metalized wing-bound avidin exposed to a range of Biotin solution concentrations.....	114
Fig. 5.11 Ratios of the heights of the peaks at 975 cm^{-1} (peak 1) and 1000 cm^{-1} (peak 2) in the SERS spectra of the avidin-biotin complex for gold-coated butterfly wings for a range of concentrations of biotin in buffer solution.....	115
Fig. 6.1 SEM images of seeded gold nanoshells (left) and fused nanoshells with incomplete shells (right)	121
Fig. 6.2 SEM image of a single, complete nanoshell. The scale bar is 200 nm.	122
Fig. 6.3 Darkfield microscopy image of gold nanoshells annealed to a glass coverslip, in air; the green and the purple box represent the flow cell experiment locations for spectra 1 and 2 respectively.....	124
Fig. 6.4 Scattering profile for GNS 1. The dashed lines denote the theoretical calculation, the solid lines are the experimental result: black is for GNS surrounded by air, red is for GNS surrounded by culture medium	125
Fig. 6.5 Scattering profile for GNS 2. The dashed lines denote the theoretical calculation, the solid lines are the experimental result: black is for GNS surrounded by air, red is for GNS surrounded by culture medium.	125
Fig. 6.6 Extinction spectrum of fresh gold nanoshells (nanoComposix)	126
Fig. 6.7 Theoretical extinction spectrum of gold nanoshells, silica core radius 60nm gold shell thickness 15nm, in phosphate buffered saline calculated based on Mie scattering theory, with the peak intensity scaled to match [130]	127

Fig. 6.8 Emission spectra of gold nanoshells under excitation from Stokes (black) and pump and Stokes simultaneously (red).....	128
Fig. 6.9 Schematic diagram outlining the Neubauer Improved haemocytometer [177]	133
Fig. 6.10 Epi- (left) and forwards- CARS (right) images of gold nanoshells suspended in agarose gel. Images were obtained using pump and Stokes wavelengths of 918 nm and 1265 nm respectively. Each image width is 260 μm	135
Fig. 6.11 CARS and white light microscopy images of macrophage cells, with and without GNS. Left to right: before exposure to CARS, CARS image and after exposure to CARS and trypan blue staining. The top row corresponds with undosed cells and the bottom row with cell exposed to GNS. The CARS excitation wavelengths were tuned to the CH resonance for the F-CARS (red) and off this resonance for the epi-CARS (blue).....	136
Fig. 6.12 Graph depicting the percentage of photothermally ablated macrophage cells as a function of laser energy at the sample (red line). The baseline mortality exhibited by both GNS-containing cells unexposed to CARS, and GNS-free cells exposed to CARS up to 35 J laser energy at the sample is also shown (blue line).....	137
Fig. 6.13 Effect of H ₂ S donors on macrophage uptake of GNS.....	140
Fig. 6.14 Forwards-CARS (grey) and epi-CARS (red) signal obtained from mouse macrophages containing gold nanoshells. The excitation wavelengths used were: $\lambda_p = 924 \text{ nm}$ $\lambda_s = 1064 \text{ nm}$ (A), $\lambda_p = 919 \text{ nm}$ $\lambda_s = 1263 \text{ nm}$ (B), $\lambda_p = 912 \text{ nm}$ $\lambda_s = 1278 \text{ nm}$ (C), $\lambda_p = 924 \text{ nm}$ $\lambda_s = 1255 \text{ nm}$ (D).....	141
Fig. 6.15 Forwards CARS (grey) overlapped with epi-CARS (red) of A431 cancer cells incubated with nanoshells and varying concentrations of GYY excited at $\lambda_p = 924 \text{ nm}$ $\lambda_s = 1255 \text{ nm}$. Concentrations of GYY for each image: A = 10 μM , B = 100 μM , C = 0.5 mM, D = 1.0 mM	142
Fig. 7.1 Schematic diagram detailing the blood-brain barrier and its transport mechanisms, adapted from [182, 183].....	149
Fig. 7.2 CARS (left) and SRS (right) images of a mouse brain perfused with FD4 fluorescein isothiocyanate-dextran, with pump and Stokes wavelengths at 816.....	152
Fig. 7.3 SRS image of an undosed, “blank” mouse brain (left), the red blood cells from which are isolated for clarity in the right image. Scale bar = 40 μm	153
Fig. 7.4 Three dimensional analysis using ImageJ Volume Viewer of a stack of images obtained with SRS of an undosed brain, imaged using pump and Stokes wavelengths of 816 nm and 1064 nm respectively. The depth of the stack is 13 μm	154
Fig. 7.5 Three dimensional rendering using ImageJ Volume Viewer, of a blood vessel in a blank mouse brain, imaged using SRS pump and stokes wavelengths of 813 nm and 1064 nm respectively. The stack depth is 24 μm	155
Fig. 7.6 Spontaneous Raman spectrum of ApoE-albumin.....	158
Fig. 7.7 Spontaneous Raman spectrum of PEG-albumin.....	158
Fig.7.8 A comparison of spontaneous Raman spectra of ApoE-albumin and PEG-albumin nanoparticles dried onto aluminium-coated microscope slides.	159

Fig. 7.9 Epi-CARS images of nanoparticles. The left-most image illustrates thresholding at 1 standard deviation above the mean pixel intensity value; the right-most image illustrates thresholding at 2 standard deviations above the mean pixel intensity value.	160
Fig. 7.10 A comparison of colocalisation parameters on images of brain endothelial cells devoid of nanoparticles. In A, the colocalisation intensity threshold was set to the mean intensity, giving false-positive nanoparticle signal. In B, the intensity threshold was set to the mean + 1 standard deviation, which effectively screened out all false positive signal. The scale bar is 40 μm	161
Fig. 7.11 CARS image of human brain endothelial cells inoculated with ApoE-albumin nanoparticles incubated for 45 minutes (left) and 15 minutes (right). Scale bars are both 40 μm	162
Fig. 7.12 CARS image of brain endothelial cells inoculated with PEG-albumin nanoparticles for 45 minute incubation (left) and 15 minute incubation (right). Scale bars are 40 μm (left) and 20 μm (right).	163
Fig. 7.13 Molecular structure of DAB16.....	165
Fig. 7.14 Spontaneous Raman spectrum of DAB, with no background subtraction	168
Fig. 7.15 Spontaneous Raman spectrum of pDNA, with no background subtraction.....	168
Fig. 7.16 Spontaneous Raman spectrum of DAB/pDNA nanoparticles, with no background subtraction	169
Fig. 7.17 SRS and CARS images of cancer cells with and without dendrimer nanoparticles. Top row: undosed cancer cell, bottom row: cancer cell dosed with a high concentration of DAB/pDNA nanoparticles (200 μL per culture dish). SRS image at 813 nm and 1064 nm (left), EPI-CARS image at the same pump and Stokes wavelengths (middle) and SRS at 921 nm and 1064 nm (right). Each image is of a sample area 30 μm across.	170
Fig. 7.18 SRS images of confluent cancer cells with dendrimer/pDNA nanoparticles at a low concentration (100 μL per dish). Scale bar = 50 μm . Top row: RGB merged images of three confluent cancer cell regions imaged at 813 nm and 1064 nm (red), 938.9 nm and 1064 nm (green) and 821 nm and 1064 nm (blue); the white pixels marked with arrows indicate signal from nanoparticles. Bottom row: greyscale images of the same three regions, imaged at 813 nm and 1064 nm, for comparison.	171

1. Introduction

INVESTIGATION INTO THE INTERACTION of nano-scale structures and biological samples using light microscopy and spectroscopy techniques is part of a relatively new and rapidly developing field of research known as nano-biophotonics. The development of powerful new chemically-specific multiphoton imaging techniques in particular has broadened the scope of the field of nano-biophotonics and provided the motivation for much of the work presented in this thesis. The aim of this thesis is to deepen our understanding of biological specimens by using Raman scattering techniques to probe the interactions between proteins, cells and tissue with both organic and metallic structures.

In this introductory chapter, the outline of the thesis will be presented together with some historical context of the field of nano-biophotonics.

1.1. The History of Photonics in Biology

Biophotonics concerns the detection, imaging and manipulation of biological samples using light. Various biophotonic methods for investigating organs, tissues and cells have been developed which can be used to characterise different attributes of the sample, all of which rely on microscopy to some degree. A few common examples of applications of such methods include: microspectroscopy, confocal microscopy, fluorescence microscopy and optical diagnosis of diseases. As the resolving power of microscopes has improved, so too has the level to which we can characterise biological samples, hence the techniques that rely upon microscopy have become more precise. However, there are limits to how much the resolving power may be improved for light microscopy, which may be put into context when the history of the microscope is considered.

The term microscope is derived from the Greek *mikrós*, meaning “small” and *skopeîn*, “to view”, and is used to describe instruments designed to enable observation of such miniscule objects that would be otherwise invisible to the naked eye. The existence of

intricate works of art, such as engravings too small to be seen with the naked eye, dating from the Roman and ancient Greek periods indicate that magnifying lenses have been in use for at least two thousand years. In spite of this, credit for the invention of the first microscope is generally given to a team of Dutch eyeglass makers who are believed to have produced it between 1590 and 1608 [1]. Their designs relied on using a single movable lens, set inside a “copper tube six feet long and one inch in diameter” [1]. Although these devices provided hitherto unparalleled magnification of objects, they needed to be positioned very accurately since they contained but one lens, and this made them cumbersome to use. In spite of this practical limitation, some remarkable discoveries were made, most notably by Antoni van Leeuwenhoek when he reported the discovery of micro-organisms (so called “animalcules”) in 1676 [2]. Using microscopes containing single lenses, he was the first scientist to observe red blood cells, spermatozoa, bacteria and even cellular organelles.

The first microscope that made use of more than one lens (the compound microscope) was developed by Robert Hooke in around 1665, providing a more workable microscope setup, with up to 30 times magnification. Hooke’s illustrated work *Micrographia*, published in 1667, detailed many of his discoveries and led to a marked increase in the popularity of the microscope. Hooke also devised the first and simplest means to calculate the magnification using a graticule. The level of magnification Hooke obtained was overtaken by a compound microscope developed by Jan Swammerdam around 1675, providing magnifications of up to 150 times. The basic compound microscope design pioneered by these scientists is still very similar to microscopes in use today, although numerous improvements have been made, primarily in England and Italy during the 17th and 18th centuries.

The main limitations to the early compound microscopes were not a result of low magnification; in principle, by using more lenses the magnification of a compound microscope may be increased indefinitely. It is the resolving power of the microscope, the minimum lateral distance between two points that can be resolved, that limits the quality of the images obtained. Aberrations within the microscope decrease its resolving power; these aberrations may be greatly reduced by grinding the lenses appropriately and spacing them correctly within the microscope. The first complex lens was developed by Chester Moor Hall in 1733 using lenses with lead-containing flint

glass and the standard crown glass. The refractive indices of these two types of glass were sufficiently different to each other that the complex lens was found to greatly reduce chromatic aberration. This development paved the way for further complex lens designs that have continually reduced chromatic and spherical aberrations. The diffraction within the microscope is thus the main limiting factor to improving the resolving power.

In spite of the significance of the development of the compound microscope to science, initially it was regarded by many as merely an expensive toy, and since publications detailing the microscopic discoveries were only available to a few wealthy enthusiasts, it is perhaps unsurprising that the use of microscopes was not more widespread. It wasn't until 1841 that the full implications of the microscope as an aid to diagnosing disease were fully appreciated, when the Council of the Royal College of Surgeons established a Professorship of Histology. The Council also collected histological preparations of animal and plant tissues, both healthy and diseased, in order to provide a library of reference material. From these beginnings, histological anatomy thus became an important subject in medical science.

Modern light microscopy is undertaken with compound microscopes containing many complex optical elements to obtain the high magnification and achieve the optimum possible resolution. In spite of these advances, there is still a minimum distance between two points at which they may be resolved. This optical resolution is often defined using the Rayleigh criterion, stating that two components of equal intensity should be considered as resolved when the principle intensity maximum of one component coincides with the first minimum of the second. When considering a classical description of the focal field produced by a high numerical aperture lens for an N th order optical process, the lateral and axial limits of resolution, r_0 and z_0 respectively, are found to be:

$$r_0 = \frac{0.61\lambda_0}{\sqrt{NNA}}, \quad z_0 = \frac{2n\lambda_0}{\sqrt{N}(NA)^2}, \quad (1.1)$$

where λ_0 is the wavelength of light in vacuum, NA is the numerical aperture and n is the refractive index of the medium [3]. Although useful for estimating the theoretical limit

of resolution, equation (1.1) is based upon a number of theoretical factors to account for the behaviour of high numerical aperture lenses and hence should not be considered to provide absolute values from a general physical law.

Equation (1.1) leads to a lateral object resolution of about $0.3 \mu\text{m}$ for first-order processes at wavelengths of light around $0.5 \mu\text{m}$. When using the shortest wavelengths of light that are still practical for light microscopy with the highest possible numerical aperture optics, the smallest experimentally obtainable value of r_0 is about $0.2 \mu\text{m}$ [4]. It is at this length scale that cell dynamics start to become very interesting, for instance white blood cells are typically $\sim 20 \mu\text{m}$ in diameter (requiring a minimum magnification of $\sim 3.6 \times$ to resolve them) and DNA molecules are typically 2 nm in diameter (requiring a minimum magnification of $40,000 \times$ to be resolved). The depth of field can be reduced by using higher numerical aperture lenses, as illustrated in Fig. 1.1, as well as by using a confocal set-up.

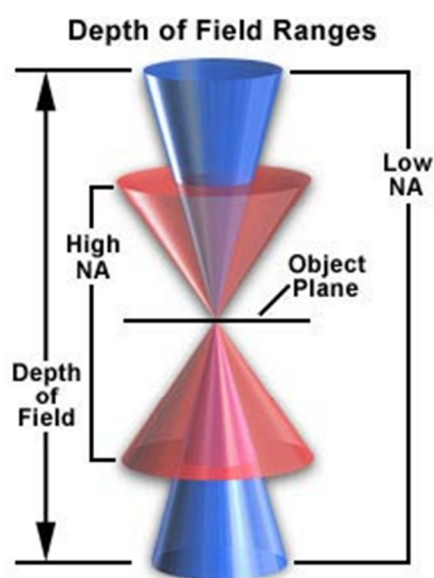


Fig. 1.1 Depth of field ranges for lenses of high and low numerical apertures [5].

In order to better understand the practical limitations involved in microscopy of biological samples, it is helpful to consider the structure of the cell. Since animal and plant cells vary in size from $1 - 100$ micrometres, they may only be visually studied in detail with the aid of a microscope [6]. Cells are divided into two classes; prokaryotic (cells that lack a membrane-bound nucleus, as found in bacteria and cyanobacteria) and eukaryotic (cells that have a membrane-bound nucleus and organelles, as exhibited by

animals, plants, fungi and protists). In general, animal cells may be thought of as fluid-filled phospholipid bilayer sacs, although the exact components of the cells vary depending on their function. The generalised anatomy of an animal cell is detailed in Fig. 1.2 and a more detailed description of cells, their contents and functions is given in Chapter 2.

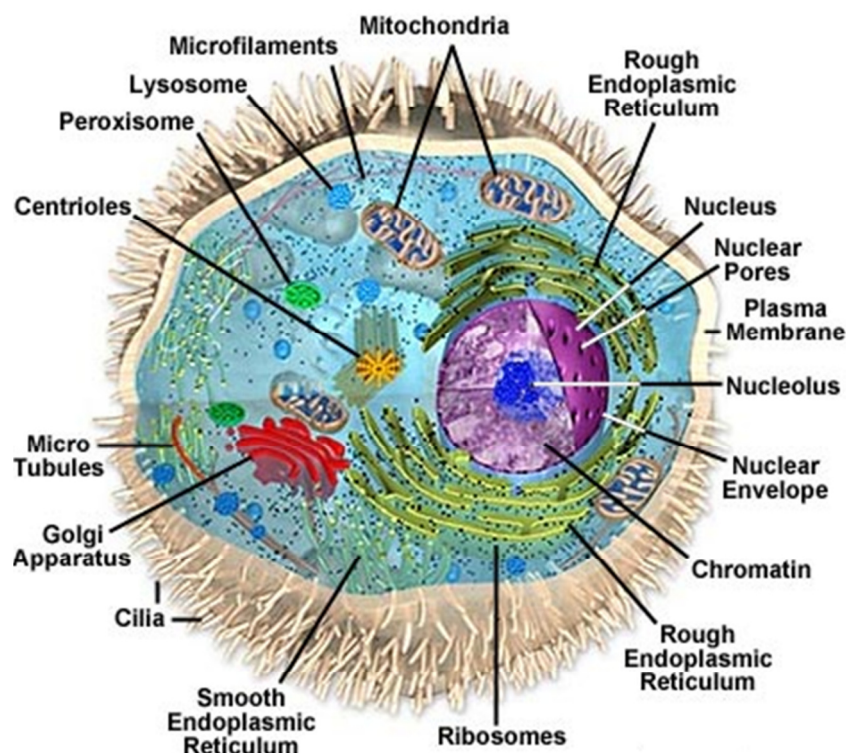


Fig. 1.2 The anatomy of an animal cell [7].

The most abundant components of the plasma membrane are the phospholipids. These have hydrophobic lipid “tails” and hydrophilic negatively charged phosphate “heads”, which prevent the uncontrolled loss or uptake of water; the layers internal and external to the cell are water-soluble whereas the middle region of the bilayer is hydrophobic. In addition to the phospholipid “water barrier”, the plasma membrane contains specialised proteins, which enable it to be selectively permeable. In order to provide greater strength to the cell, animals developed complex carbohydrate, sugar, lipid and protein networks, whereas plants developed rigid cellulose cell walls [4, 6].

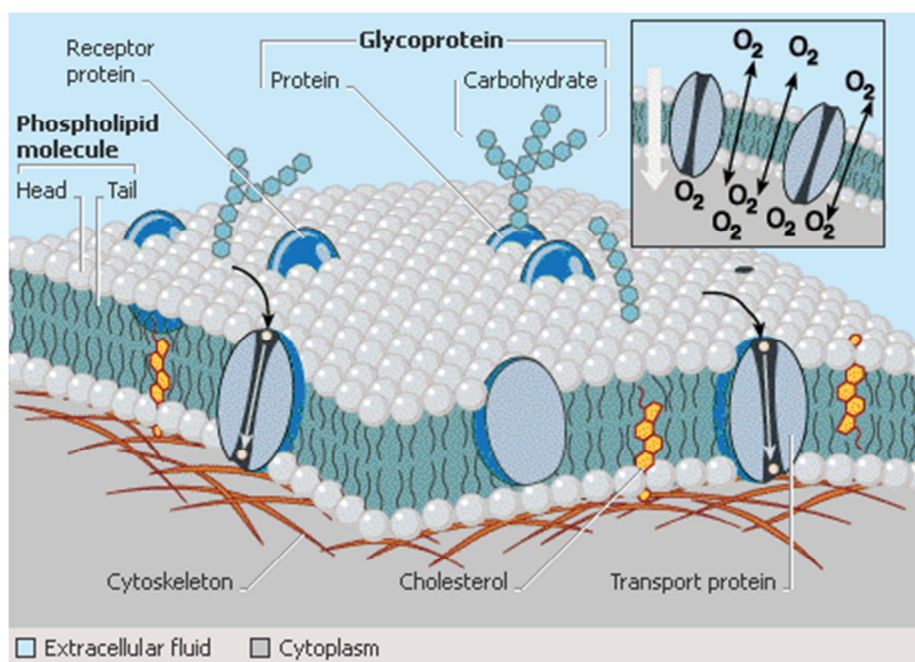


Fig. 1.3 Schematic cross-sectional structure of the cell membrane [8].

In spite of the wide variety of organelles and different molecules comprising cells, their contents are all generally transparent to light to the same degree, hence obtaining clear images of their internal structures poses a challenge for white light microscopy. This is also an issue for obtaining images of histological sections of tissues, since it can be difficult to distinguish between tissue types within the section. These limitations can be overcome to an extent by using certain sample preparation protocols, at the expense of maintaining the sample in a natural state.

When preparing cells or histological sections of tissues for imaging, samples may be stained and fixed in a solution containing alcohol or formaldehyde, and in the case of tissues, embedded in a material such as paraffin wax or plastic. A wide variety of stains have been developed for different applications; for instance, some are able to indicate the presence of certain ions within a sample, while others will only permeate cells with damaged membranes [9].

After staining and embedding, tissues are sliced to a required thickness, and mounted on a glass microscope slide, whereas fixed cells are generally kept on the coverslips they were grown on. The fixative acts to denature enzymes and causes covalent bonds between amine groups to form, thus stabilizing the samples by preventing decomposition and degradation. Fixative also prevents cells from migrating within the

focal area during imaging, which enables detailed images to be obtained over long periods of time. However, investigation of a fixed sample can only yield information about its static state; cellular dynamics and molecular interchanges in the sample cannot be probed in real-time using this technique.

As microscopy techniques improved, less invasive imaging methods suitable for use with live cells have been developed. Live cell imaging has traditionally been a specialised technique used by biologists, but has rapidly become a new exploratory science that combines many scientific disciplines. More recently, biological systems in cells have been tagged with fluorescent biological markers and imaged, with ever increasing resolution.

The first microscope capable of imaging fluorescence was invented in 1904, and the first fluorescently-labelled antibodies were introduced to the field in 1941 [9]. However it wasn't until the 1970's that the two were used together effectively, perhaps as a result of the misconception that antibodies were only of use when investigating infection. Antibodies were first raised against the "normal" proteins tubulin and actin in 1974 [10]. As news of this discovery spread among cell biologists in the late 70's, it wasn't long before fluorescently labelled antibodies were applied to cells, revealing the intricate architecture of the cytoskeleton [10]. Concurrently, fluorescent stains were developed to respond to important intracellular parameters, such as calcium ion concentration. These developments led to a rapid increase in the use of fluorescent microscopes in cell biology, to the point where perhaps half of all published work in this field in the early 1980's relied on fluorescence microscopy [10, 11].

Perhaps the most significant marker used is green fluorescent protein (GFP), an autofluorescent molecule extracted from jellyfish which fluoresces green under blue light. Molecular cloning methods allow the fluorophore moiety to be fused to a large range of enzyme and protein targets, enabling cellular processes within both live and fixed cells to be monitored using various microscopy techniques. Genetic mutants of GFP have been produced, which exhibit different colours or shifted excitation peaks. Other unrelated markers include red fluorescent protein (RFP), and these may be directly injected into cells [4, 6, 9].

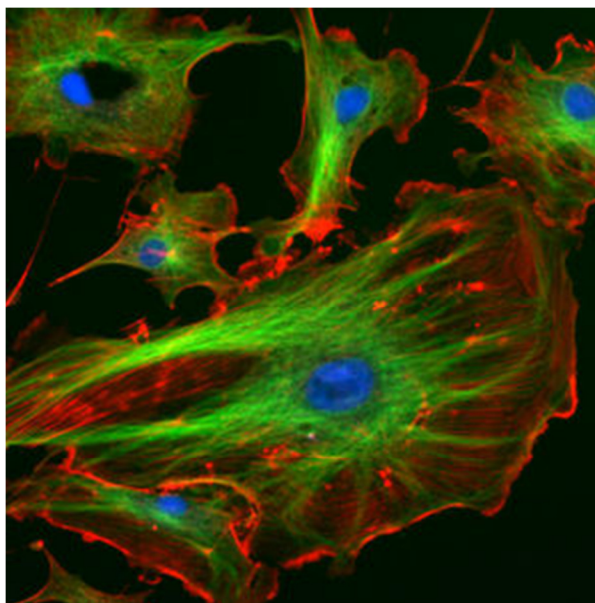


Fig. 1.4 Endothelial cells under the microscope. Nuclei are stained blue with DAPI, microtubules are marked green by an antibody and actin filaments are labelled red with phalloidin [12].

However, by 1984 it had become clear that the principle limitation of the fluorescence microscope came about from the large depth of focus [10]. The regions of thick specimens that were out-of-focus gave a uniform background glow which prohibited fine detail being distinguished. This problem prevented detailed investigation into all but thin, flat cell lines.

The invention of the confocal microscope by Minsky in 1955 proved to provide a means of blocking light from out-of-focus regions of the sample. The term “confocal” was first used by Brakenhoff in 1979 to describe a microscope which provided illumination confined to a diffraction-limited spot in the sample, and with an aperture in front of the detector in such a position as to optically conjugate the focussed spot [13]. By using pinholes to reject the out-of-focus light in this manner as illustrated in Fig. 1.5, the measured intensity from a fluorescent point object decreases with distance from the plane of focus according to an approximately inverse fourth-power rule. Using laser light as the source of illumination in coherent microscopy provides a tightly collimated, coherent beam, capable of “optically sectioning” thicker samples to provide three dimensional images with most of the out-of-focus glare being completely eliminated [11].

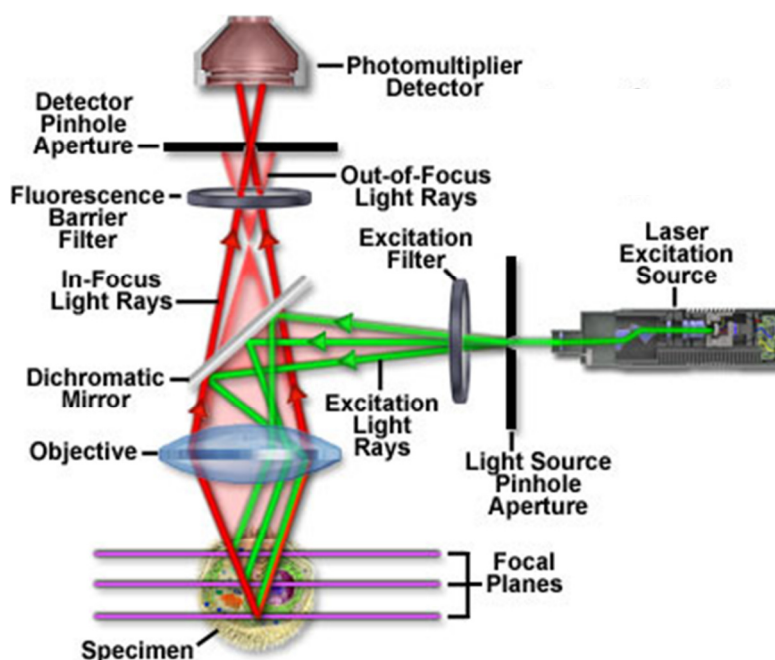


Fig. 1.5 A schematic diagram of a confocal microscope [14].

Although the technique of fluorescent tagging is useful, it is somewhat limited. The fluorescent tags have to be chosen carefully, so that they adhere to three requirements: that the tag will remain stable in the cellular environment; that the act of binding won't alter the target molecule to an unacceptable degree; the tag must bind in the expected manner. The act of binding a fluorescent tagging molecule to a cellular protein frequently alters the target protein's configuration and function. Other drawbacks to fluorescent microscopy arise from the potential for cell damage. Cells are susceptible to photo damage, especially when fluorophores are used, since they release free radicals during photo bleaching; this limits the time over which tagged cells may be imaged. Confocal fluorescence microscopy also suffers from a limited depth penetration; only thin samples can be investigated using this set-up.

Other techniques for distinguishing between the components of the cell and to provide better contrast between cells and their surroundings, have used phase contrast imaging techniques. The human eye is sensitive to differences in light amplitudes and wavelengths, but not to differences in phase. In brightfield microscopy, there is little contrast between biological structures in tissues and cells which exhibit similar transparency to light; phase contrast microscopy exploits the variations in the refractive indices of the sample's components. The small phase shifts in the light passing through the samples are converted to contrast changes in the resulting image, as shown in

Fig.1.6. The ability to image cell contents using phase contrast microscopy has been of great use, particularly when the cell cycle was studied in detail using phase contrast microscopy [9].

Although this technique is useful for studying live cells without the need for exogenous fluorophores or other tags that might alter the chemical environment, it is not without its limitations. Phase contrast may result in a reduction of resolution, since the phase-annulus used in the condenser limits the angle of admittance and hence the numerical aperture is limited. Another limitation is that it is only suitable for use with thin objects that do not result in major changes in absorption of light; for tissues and very large cells, phase contrast produces distorted images. In addition, phase contrast images are frequently surrounded by “halos”, optical artefacts which may obscure the boundaries of details in the image.

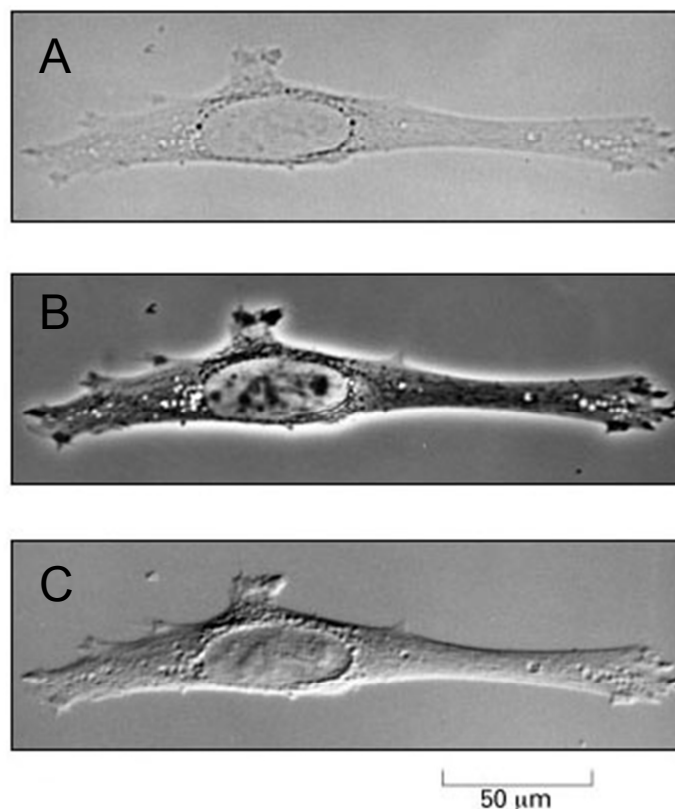


Fig.1.6 White light microscopy images of an animal cell. (A) was imaged using bright-field optics, (B) with phase-contrast optics and (C) was imaged with differential interference-contrast optics [15].

An alternative to optical microscopy for imaging biological samples is electron microscopy. Electron microscopes have been used by biologists to image the cell organelles that are otherwise too small to resolve using light microscopes, and they have the advantage of being suitable for use with thin sections of tissue as well as with cells. Images are produced electronically after detecting electrons which have interacted with a sample inside a vacuum chamber. In Transmission Electron Microscopy (TEM), electrons are fired at the sample, and the transmitted beam is collected and magnified. The sample may be treated with heavy metal-containing stains in order to improve the degree to which electrons are scattered in the sample. In traditional Scanning Electron Microscopy (SEM), three-dimensional images are made by collecting secondary electrons produced by the metal-coated sample under excitation from the incident electron beam.

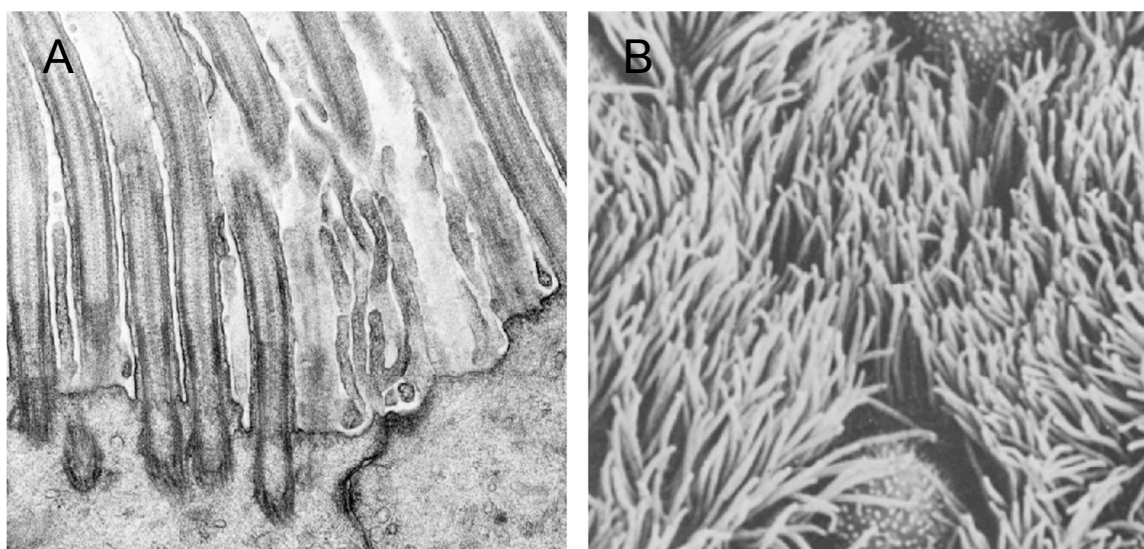


Fig. 1.7 Comparison of images produced with TEM and SEM [16]

A - Transmission electron microscope image of human tracheal epithelium in cross-section, B – Scanning electron microscope image of human tracheal epithelium as viewed from above.

Although electron microscopes provide very high resolutions (by 2009 the highest resolution obtainable for SEM was 0.4 nm at 30 kV with the Hitachi S-5500, while for TEM resolutions of up to $\sim 0.2 - 0.5$ nm are possible [6, 17, 18]), they have small fields of view, which can limit their imaging capabilities for larger samples. Also, they are much more time consuming and expensive to run than light microscopes, which makes them less convenient for spontaneous sample imaging. More major setbacks arise from

their inability to be used to image live cells as they require the samples to be fixed and dehydrated in order to be imaged in a vacuum. Some of the pre-treatment may also damage delicate samples and have the potential to produce artefacts.

Imaging of samples is not always necessary, especially for assay techniques where it is the detection and quantification of a particular analyte that is required. Assaying is just as important an application of photonics in biology as imaging, and contrast is just as fundamental to assaying processes. The majority of assaying techniques rely on the detection of a binding event between the analyte and a substrate, in such a manner as to enable quantitative conclusions to be drawn about the concentration of the analyte.

Many different approaches have been successfully exploited for the detection of molecular binding events, such as: scintillation counting, fluorescence, absorption, electrochemistry, chemiluminescence, radiometric tagging, Rayleigh scattering and Raman scattering [19, 20]. Among these, fluorescence has been the most widely used readout method for industrial application, frequently in enzyme-linked immunosorbent assays (ELISA) [20], since high sensitivity is critical for the immunoassay detection. However, fluorescence based readouts rely upon exogenous fluorescent labels that can alter binding interaction and can be unreliable when assaying in the presence of autofluorescent or scattering compounds [21]. In addition, the risk of photobleaching of the fluorophores used can limit the applications of such fluorescent-based assays. Multiphoton detection techniques offer reduced photodamage and photobleaching with an improved depth penetration as compared with confocal microscopy assaying techniques. Raman-based assaying techniques offer the advantage of label-free chemical specificity, which may be enhanced using the surface plasmon resonance of nano-scale metallic substrates to provide sub-diffraction limited resolution of binding events.

Techniques for detection and analysis of molecules in biological samples have become increasingly widespread in recent years as forensic, medical and analytical chemistry techniques have advanced. Cellular imaging and analysis techniques now enable inter- and intra-cellular processes to be studied in detail. The potential applications of these techniques include the study of: the interaction between therapeutic drugs and cells, the effects of disease on cells, the detection of low concentrations of chemicals within a

sample, development of biological probes and sensors, and other biotechnological applications. As a result, drug design and delivery techniques, medical screening, forensic detection of evidence at crime scenes, detection of chemical/biological weapons and many more areas of science have the potential to become much more efficient.

1.2. Emerging Photonic Techniques in Biology

This thesis concerns the recently developed multiphoton imaging techniques known as coherent anti-Stokes Raman scattering (CARS) and stimulated Raman scattering (SRS). These are label-free techniques based on vibrational spectroscopy which rely on exciting intrinsic chemical bonds within the sample. As such, these techniques do not rely on extrinsic fluorophores, thus reducing the perturbation of the local chemical environment of the sample. Since live cell cultures may be imaged in real-time using these techniques, it is possible to probe the molecular machineries at work. The multiphoton nature of the excitation provides high spatial resolution, 3D sectioning capabilities without the requirement for a confocal setup, providing exquisitely clear images of tissues and cells.

1.2.1. Coherent Raman Scattering

In order to perform vibrationally selective imaging using CARS and SRS, it is first necessary to perform spontaneous Raman spectroscopy of the sample of interest. In Raman spectroscopy, the intensity of light scattered from a sample is measured as a function of the energy shift (Raman shift) with respect to the incident beam, in units of wavenumbers (cm^{-1}). The scattered light's energy is shifted with respect to the incident beam as a result of interactions with Raman-active chemical bonds within the sample; the Raman spectrum therefore is populated by narrow peaks which correspond to particular chemical bonds, and is therefore a unique “fingerprint” of the particular sample. The intensity of the Raman scattered light is directly proportional to the number of vibrationally active chemical bonds, which often allows straightforward quantitative analysis. By identifying peaks of interest in the Raman spectrum, it is therefore possible to tune the laser wavelengths in CARS and SRS to match these

chemical bonds and provide a “map” of particular molecular species within a given sample. This can therefore be used to provide detailed, high-resolution images of chemical species of interest within biological samples, as well as potentially identify drug molecules within a sample.

Since spontaneous Raman scattering is a relatively weak process, enhancement mechanisms employing nanostructured metallic substrates are used in surface enhanced Raman spectroscopy (SERS). These techniques exploit the altered Raman cross section and enhanced local electromagnetic field in the vicinity of such metallic features which are a result of surface plasmon resonances and dense grouping of electric field lines in the vicinity of sharp geometric features.

This thesis explores the interaction of tissues and live cell cultures with both organic and metallic nanoparticles using CARS and SRS, and gives details of a highly biocompatible SERS substrate based on a naturally occurring nanostructured surface.

1.3. Thesis Aims

The first limitation posed to biophotonics that is addressed in this thesis, is the issue of spatial resolution. The diffraction limit prevents detailed investigation of structures that are under $0.2\ \mu\text{m}$ and it is at this level that cellular and molecular dynamics become most interesting [4]. The diffraction limit also impinges on photo-therapy and assaying techniques, since the size of the typical biological or drug molecules and phototherapeutic particles of interest is much lower than $20\ \mu\text{m}$, hence the signal obtained would be the average of many molecules within the diffraction-limited area. By using nanotechnology, it is possible to confine the signal obtained from a sample to sub-diffraction limited regions and hence overcome the issue of spatial resolution.

The next issues that this thesis will address arise from contrast and chemical specificity. Traditional biophotonics methods have used stains and extrinsic tags to provide contrast within biological samples and to detect specific chemical species, or have investigated the intrinsic structural features by detecting scattering, absorption, reflection and

diffraction of light impinging upon the sample. Staining and tagging samples alters their chemical environment and hence can lead to erroneous conclusions about the processes under investigation, while using structural features for contrast doesn't provide any chemical information. The experiments in this thesis probe intrinsic chemical bonds to both provide contrast and chemical specificity using Raman scattering-based modalities for imaging and assaying, without the need for extrinsic tags, or stains. Since spontaneous Raman scattering is a weak process, this thesis makes use of nanotechnology and coherent enhancement mechanisms to enhance the signal.

1.4. Overview of Thesis

In order to better appreciate the context of the work within this thesis, Chapter 2 gives an outline of the historical context of Biophotonics, with particular emphasis on Raman-based spectroscopic methods, as well as a general introduction to the history of cellular biology and biological assays. The theoretical background of spontaneous and coherent Raman scattering, as well as the mechanisms of surface enhanced Raman scattering and photoluminescence theory, are given in Chapter 3. The experimental instrumentation used in this thesis is described in Chapter 4.

The efficacy of naturally occurring nanostructures and their biomimetic analogues for use as surface enhanced Raman scattering substrates in protein binding experiments is investigated in Chapter 5. The experiments undertaken in this chapter aim to produce a model protein assaying system based on avidin and biotin, using the metal-coated sub-diffraction limited chitinous surface features of butterfly wings and nanostructured metal-coated polymers as substrates. The results obtained showed that these substrates not only provide a suitable topography for SERS, but that SERS signals can still be obtained whilst the substrate is immersed in a droplet of saline. This is a major advance in the field of SERS assay, since previous substrates have required desiccation of the sample, which leads to protein denaturation. Our assay proved to be sensitive to biotin in solution in volumes of 30 μL over a wide range of concentrations (0.12 ng/mL – 0.24

$\mu\text{g/mL}$), which would prove to be especially advantageous in applications where small sample volumes are required.

Metallic and organic nanoparticles for use as coherent Raman scattering contrast agents and as therapeutic agents are investigated in chapters 6 and 7 respectively. The metallic nanoparticles used are gold nanoshells, whose plasmonic characteristics were exploited in Chapter 6 for use as photo-thermal ablation agents of live cells, and later as contrast agents in macrophage phagocytosis experiments.

The two types of organic nanoparticle investigated in Chapter 7 were dendrimer nanoparticles combined with plasmid DNA, and albumin conjugated to Apo lipoprotein E (APOE). The dendrimer nanoparticles have been reported as promising gene therapy agents in cancer cells, while the APOE-conjugated albumin particles are of interest in investigating drug transport across the blood-brain barrier. Methods for imaging and identifying these particles within live cells using coherent Raman scattering were devised. Since the ultimate application of these drug nanoparticle detection methods would be to quantify the concentration of drug entering the brain, coherent Raman scattering microscopy was also employed to determine the extent to which the blood brain barrier could be imaged in brain tissue slices.

2. Background and Literature Review of Raman-based Biophotonics

IN ORDER TO APPRECIATE the relevance of the work undertaken in this thesis to enhance Raman techniques in biology, it is important to consider the discoveries already made in this field. To that end, the historical context of photonics in biological research will be given in this chapter, together with a brief overview of the structure of cells. The application of photonics to the field of assaying is described, followed by a brief history of Raman scattering, from its discovery to present-day applications. From this point, it is natural to progress to the topic of surface enhanced Raman scattering (SERS) and so the discovery and application of SERS to biological problems is outlined in section 2.6, together with an overview of a particular case of a SERS substrate, the gold nanoshell. Finally, the history of coherent Raman scattering is summarised, together with a brief statement of the contribution this thesis aims to make to the field of nano-biophotonics.

2.1. Nanotechnology in Biophotonics

Natural history and medicine have been studied since the ancient Greco-Roman world but it wasn't until the 19th Century that the Biological sciences arose as a single coherent field [6]. Biological systems in nature were identified, classified and studied for centuries before the notion that “all organisms are composed of cells derived from other cells” was proposed as a theory in the mid-1800s [22]. It was the invention of microscopes that enabled this theory to be developed, combined with a paradigm shift in the approach of biologists from being purely observational to seeking a more fundamental understanding of the behaviour of the systems they were describing [6].

Cells were first described by Hooke in 1665 when he thinly sliced pieces of cork with a penknife and examined them using a microscope he had built himself. Hooke's microscope could only magnify objects 30-fold and since his samples were desiccated and dead, his observations were limited to a description of the empty box-like

compartments made by cell walls which he named *cellulae*. In spite of this early discovery, the true nature of cells, even the fact that they are alive, could not be determined until the resolving power and magnification provided by microscopes was improved sufficiently for the cellular components to be observed [6, 22].

Sufficient evidence that all cells are derived from other cells wasn't obtained until the discovery of the nucleus and chromosomes that enabled cell multiplication to be understood. Since then the modern discipline of cellular biology has advanced rapidly, combining cytology, which deals with the structure of cells, biochemistry, which concerns the chemistry of biological structure and function, and genetics, which covers the "information flow" of genetic material from one generation to the next. All three of these sub-disciplines of cellular biology have advanced as imaging techniques have progressed, to the point where subcellular components are now routinely investigated in great detail [22-25].

Confocal microscopy is currently the standard technique used for imaging both cells and tissues. It provides a slight improvement to the resolution due to the use of pinholes to exclude light from above and below the focal plane. However, images may only be obtained with thin samples at low powers, and fluorescent or other labelling systems are required for chemical specificity, otherwise the images produced are merely analogous to reflectance microscopy. One major difficulty of imaging cells and their contents arises from the inherent lack of contrast between the organelles when imaged using light microscopy. Various methods for staining and tagging cellular components have enabled this problem to be overcome and this has vastly increased our understanding of cellular dynamics [9, 24, 25]. However, staining and fluorescent tagging of cellular components can perturb the local chemical environment and hence alter the system under investigation, so these methods are unsuitable for experiments that involve the detailed chemistry of living cellular dynamics [24-26]. In addition, photobleaching of fluorophores may prohibit dynamic time-lapse imaging, resulting in images that only provide a "snap-shot" of the sample.

The final limitation of light microscopy was insurmountable by the addition of stains, or by the improvement of optical components: the theoretical limit of resolution

prohibits the visualisation of cellular components which are smaller than half the wavelength of the light used to image them. This problem can be overcome by using electrons to image the sample, rather than photons, in electron microscopy. Scanning Electron Microscopy (SEM) and transmission electron microscopy (TEM) are both powerful methods for imaging; their limits of resolution are respectively 0.4 nm and ~ 0.2 – 0.5 nm 0.1 - 0.2 nm, which compares favourably with 200 – 300 nm for the light microscope [18, 22, 27, 28]. However, the processes required for preparing the sample for the vacuum chambers in SEM or TEM involve fixing and dehydration, thus dynamic cellular processes cannot be investigated using these methods.

More recent advances in the field of nanoscience have enabled researchers to obtain optical signals from nanoparticles within regions of their sample that are smaller than the optical wavelength. Such contrast agents include quantum dots, which are semiconductors that can emit light over a range of wavelengths, depending on their size; quantum dots are typically of the order of 5 nm to 100 nm [29, 30]. The larger quantum dots emit redder fluorescence, while the smaller quantum dots emit bluer fluorescence. The light produced by quantum dots is typically of much greater intensity than traditional fluorophores and their resistance to photobleaching make them very attractive candidates for use in cell imaging [30]. However, they have been shown to be highly cytotoxic, and their perturbation of the local chemical environment is a drawback for investigation of chemical processes within biological specimens [31].

Other techniques for sub-wavelength resolution include surface plasmon resonance (SPR) spectroscopy, for a review of surface plasmon sensing techniques see [32]. In this technique, the localised plasmon resonance of noble metal nanostructures is used to detect the refractive index changes arising from molecular adsorption/desorption events at the metal's surface. The binding events may be detected by measurement of the resonance angle shift, by measuring the wavelength shift (FT-SPR), by imaging or microscopy. In resonance angle shift and wavelength shift measurements, the reflectivity of light from the metal surface is measured as a function of either angle of incidence (with constant wavelength) or wavelength (with constant angle of incidence). The imaging method uses light of both constant wavelength and incident angle to interrogate a two-dimensional region of the sample, mapping the reflectivity of the

surface as a function of position. The detection mode used depends on the substrate; suspensions of nanoparticles and planar nanostructured surfaces require different SPR detection modalities.

While SPR spectroscopy offers the potential for highly sensitive detection of binding events at low molar concentrations, it relies on the assumption that there is no nonspecific adsorption. Additionally, its range is highly dependent on the adsorption isotherm. The technique is also limited by the resolution, sensitivity and sample characteristics of the SPR/LSPR substrate used, which can lead to low throughput. In addition, shifts in the refractive index of the substrate may prove to be insufficiently sensitive for detecting subtle differences in chemicals adsorbed to the substrate. Additional complications that affect the sensitivity of SPR spectroscopy for techniques relying on detection of changes in the refractive index arise from the practical setup. Since biological experiments require the use of an aqueous environment, changes in the refractive index due to pressure and thermal fluctuations, combined with pH variations can all affect the detection limit.

However, there exist a variety of other spectroscopic methods using scattering of light for distinguishing between similar chemicals. This thesis is concerned with application of one technique in particular, Raman scattering, to a variety of biological problems. A different application of surface plasmons to spectroscopy has utilised the enhanced local electromagnetic field associated with SPRs and localised SPRs (LSPR, a localised variation of SPR which occurs when the surface plasmon is confined to a nanostructure smaller than the wavelength of incident light), to greatly increase the Raman scattering effect [32]. This enhancement of Raman scattering, dubbed SERS (surface enhanced Raman scattering) brought about by metallic nanostructures was first discovered by accident in Raman spectroscopy of Pyridine molecules adsorbed on chemically roughened silver electrodes [33]. Since that time, the mechanisms causing the enhancement have been investigated although not entirely explained [34, 35]. This surface enhanced technique offers chemical specificity, thus potentially eliminating the issue of nonspecific binding errors.

2.2. General Cell Structure

All cells, whether they contain a nucleus (prokaryotic) or not (eukaryotic) share some common features. They each comprise a phospholipid bilayer outer membrane, known as the plasma membrane, which in addition to phospholipids also contains a variety of proteins and other molecules that help it in its function as a selective barrier between the cell and its surroundings. The cell contains a variety of organelles, specialised subunits within the cell which carry out specific functions and are usually separately enclosed within their own lipid bilayer membranes, suspended in a fluid called cytosol. The organelles (excluding the nuclear region, or the nucleus), the cytosol and the particulates suspended therein are referred to collectively as the cytoplasm.

In eukaryotes, the internal organelles have their own highly specialised membranes which enable them to migrate, absorb nutrients, excrete waste materials, communicate with other cells/parts of the cell etc. The cell's outer membrane also performs these functions and many more besides, in spite of a deceptively simple structure. The cell membrane facilitates a multitude of highly specialised functions, including but not limited to: anchoring to the cytoskeleton, attachment to the extracellular matrix, transportation of chemicals via protein channels and pumps, participation in enzymatic activity, chemical-receptor-facilitated intercellular communication, self-recognition for the immune system etc. [7, 24, 25]. Better understanding of cell membranes, and the processes involved in the chemical reactions undertaken within it, would have a great impact on biotechnology, medicine and drug-delivery techniques.

Other components of the plasma membrane include carbohydrate, cholesterol and glycoproteins. These components are combined in different proportions to provide the unique mechanical properties exhibited by specialised cells, e.g. biconcave red blood cells, phagocytes whose membranes can identify “non-self” or damaged cells/particles and engulf them, bacteria whose cell membranes put out “feelers” which they use to pull themselves along etc. [6, 36].

One of the most important components of cells is DNA, which is contained in one or more chromosomes. In prokaryotes, this material is located in a non-membrane bound

nuclear region, whereas in eukaryotes the membrane-bound structure known as the nucleus contains the DNA. Cell nuclei are generally distinguishable in light microscopy.

Other structures of interest within the cell include: vesicles, single membrane-enclosed compartments within the cell used for transport of materials within the cell; mitochondria, double-membrane enclosed structures containing some of their own DNA that are responsible for energy production; Golgi apparatus, single-membrane enclosed structures that are involved in sorting and modification of proteins. Although this is not an exhaustive list of the organelles, it gives some indication of the complex interplay of a variety of specialised structures within cells. A more complete appreciation of how each of these structures works to maintain normal and abnormal cell function would have great implications for our ability to treat disease. However since organelles and their contents are generally smaller than the diffraction limit of light, it is not possible to probe these dynamics using white light microscopy.

2.3. Chemical Assay

In drug development, medical diagnostics, forensic science, security technology, cell culture and many other scientific disciplines, it is frequently necessary to screen samples to determine the concentration of a chemical. The procedures for testing the quantity or biological activity of drugs or biochemicals in a biological or organic environment are referred to as assays. The ideal assay would screen for a chemical of interest over an unlimited concentration range, and would perform equally efficiently under all required experimental conditions. For biological applications, it is particularly advantageous if the assay can be performed under conditions that are comparable to the biological system in hand. For instance, when screening for a protein binding event with a protein normally found in hen egg white, assaying with an aqueous sample at pH 7 would be ideal. There exists a wide range of different procedures for assays of this nature, each of which has its own advantages and drawbacks which depend upon the circumstances in which the assay is used.

Assaying using protein binding is a powerful analytical tool that has found a wide range of applications across many market sectors. These include clinical diagnostics, pharmaceuticals, forensic and environmental evaluation and biochemical studies [19, 37, 38]. Advances in biochemistry biosensing processes have made assaying common place; for example, home pregnancy, blood glucose, and allergy testing kits are all based upon antibody assay technology. In spite of this progress, there are still significant requirements for improvements to current assay methods used in industry. The demand for improved sensitivity, through-put, specificity, and cost efficiency in industry constantly drive advances in assay technology.

Several protein assaying methods use spectrophotometry, where the concentration of the analyte is determined by performing a chemical reaction with the protein of interest and undertaking colorimetric analysis of the solution's absorption spectrum. The most common assays of this type include the bicinchoninic acid (BCA) assay, the Bradford assay, the Lowry assay and ultraviolet absorbance of aromatic amino acid. These assays rely on the formation of a well-defined complex between the protein of interest and a chemical which produces a distinct colour change to the absorption peak upon binding. For instance, in the BCA assay, the protein of interest forms a complex with Cu^{2+} under alkaline conditions, after which the Cu^{2+} is reduced to Cu^+ , thus forming a purple complex which has an absorbance peak at 562 nm. The number of chemical species reduced, and hence the absorbance, is directly proportional to the amount of cysteine, cystine, tryptophan, tyrosine and peptide bonds present in the protein, so this method enables quantitative determination of the amount of protein in the sample provided the chemical composition of the protein is well known.

The major drawback of these spectrophotometric methods lies in the nature of their method of detection: they all screen for quantities of particular amino acids as opposed to whole proteins. Therefore, they are subject to false-positives when samples are used which are not purified and are also subject to significant protein-to-protein variation.

One way to screen for whole molecules rather than quantifying specific amino acids is to use antibody/antigen interactions. Antibodies (immunoglobulins) are complex proteinaceous structures produced in response to interactions between an organism's

white blood cells and microbes introduced to the blood stream. Proteinaceous biological markers (antigens) found on the microbes' outer membranes stimulate the production of antibodies by the humoral immune system. The antibodies enable identification and ultimately destruction of the microbes they were engineered to attach to. Antibodies have a “Y”-shape, with a heavy protein chain (the Fc domain) and two light chains (Fab domains) which terminate in structures called paratopes that bind to regions (epitopes) on specific antigens [6, 36, 39]

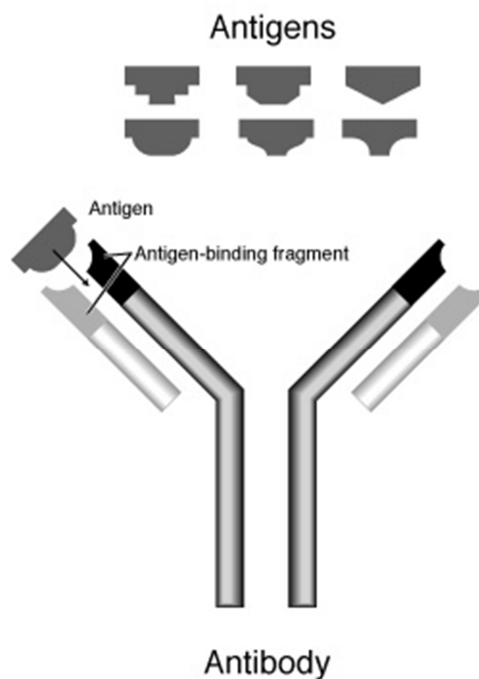


Fig. 2.1 A schematic diagram of an antibody [39].

Since antigens are present on all cell membranes and some are cell-specific, it is possible to use them to facilitate cell detection. Some protein assays involve binding the chemical of interest to a substrate (e.g. via antibody/antigen binding) and subsequently detecting the binding event. Pregnancy tests, for example, detect a hormone in urine secreted by the body during pregnancy called human chorionic gonadotropin (hCG) using a monoclonal antibody (MAb) protein conjugated to colloidal particles; any binding events between MAb and hCG result in aggregation of the particles, leading to a colour change indicative of a positive result [30, 48]. This method is more qualitative than quantitative, although advances in technology are now enabling an estimate for the stage of pregnancy to be given with the result.

Antibodies can be monoclonal, whereby every antibody is identical and binds to the same binding site on the antigen, or polyclonal, where a range of antibodies is raised against the same antigen resulting in binding to more than one binding site on the antigen. For some applications, monoclonal antibodies are preferable since they are so specific and well characterised, but for others polyclonal antibodies are more suitable, for instance when experimenting over a wide pH range for which different antibody/antigen binding sites are required.

Spectral analysis of antibodies bound to two-dimensional substrates can be problematic as they are such large proteins. It can be difficult to obtain very uniform arrays of antibodies and nonspecific binding to substrates is commonplace. To reduce the effect of this issue, the smaller Fab domains can be cleaved from the Fc regions of the antibody via the sulphur bonds. This is preferable since the Fab domains may be more readily bound to a substrate (they exhibit less steric exclusion) and exhibit less nonspecific binding. For SERS, smaller molecules are preferable as they yield less noisy spectra due to the reduction in the number of Raman bands which aren't involved in the binding event, as well as an increased signal due to the closer proximity of the binding site to the enhanced EM field of the metallic substrate.

A well-established protein binding system that is analogous to this kind of binding system is provided by avidin and biotin. Biotin is the water-soluble vitamin B-complex, also known as vitamin B₇, with a molar mass of 244.31 g/mol. Avidin is a small quaternary protein estimated as being 66 – 69 kDa in mass. It is isolated from hen egg white, which binds to biotin with one of the strongest non-covalent bonds in existence. Due to its high degree of symmetry, large number of binding sites, established structure and strong affinity for biotin, avidin is ideal for use when investigating the suitability of a SERS substrate for protein binding assays.

2.4. Raman Scattering

The Raman effect was first described by C. V. Raman [40] and since this time has been used as a very valuable tool in spectroscopy. Raman spectroscopy differs from other

spectroscopic techniques in that it is concerned with scattered rather than absorbed/transmitted light. The Raman-scattered photons either gain or lose energy during their interactions with the sample's molecules, depending on what vibrational state the molecules were in. A Raman spectrum is produced by plotting the scattered intensity as a function of the Raman shift (the frequency difference between incident and scattered light, measured in wavenumbers, cm^{-1}).

Laser light of a known frequency and polarization is used, since an intense and collimated beam allows smaller Raman shifts to be measured while allowing for improved spatial resolution. For a condensed material with a typical Raman cross section, only 1 in 10^6 incident photons undergo Raman scattering for each centimetre of material [41], thus intense laser light sources are required to provide an adequate signal-to-noise ratio in Raman spectroscopy.

Peaks in Raman spectra correspond with the Raman-active modes within the sample, which are a direct measure of the sample's vibrational energies. This means that the Raman spectrum for any sample is a unique "fingerprint", the features of which depend on the environment which the sample is in, e.g. what molecules it is bound to, the temperature of the sample etc. The chemical composition, and sometimes the molecular structure of any sample may therefore be determined using Raman spectroscopy. Since the Raman cross-section for water is sparsely populated [42], Raman spectra from wet biological samples may be taken.

Information about the chemistry of the sample being irradiated, such as its pH, may be gathered from analysis of its Raman spectrum, since a molecule's Raman spectrum will be altered depending on what chemicals it is in close proximity with [43]. The Raman band intensities are dependent only on the initial number of molecules occupying each different vibrational state. Raman scattering from molecular vibrations in the lowest state (Stokes scattered light) will produce a more intense spectrum than that scattered from higher energy molecular vibrations (anti-Stokes scattering) since more molecules occupy the lower state at room temperature. The ratio of the intensities of the anti-Stokes and Stokes spectra gives a measure of temperature; anti-Stokes scattering is used for contactless thermometry.

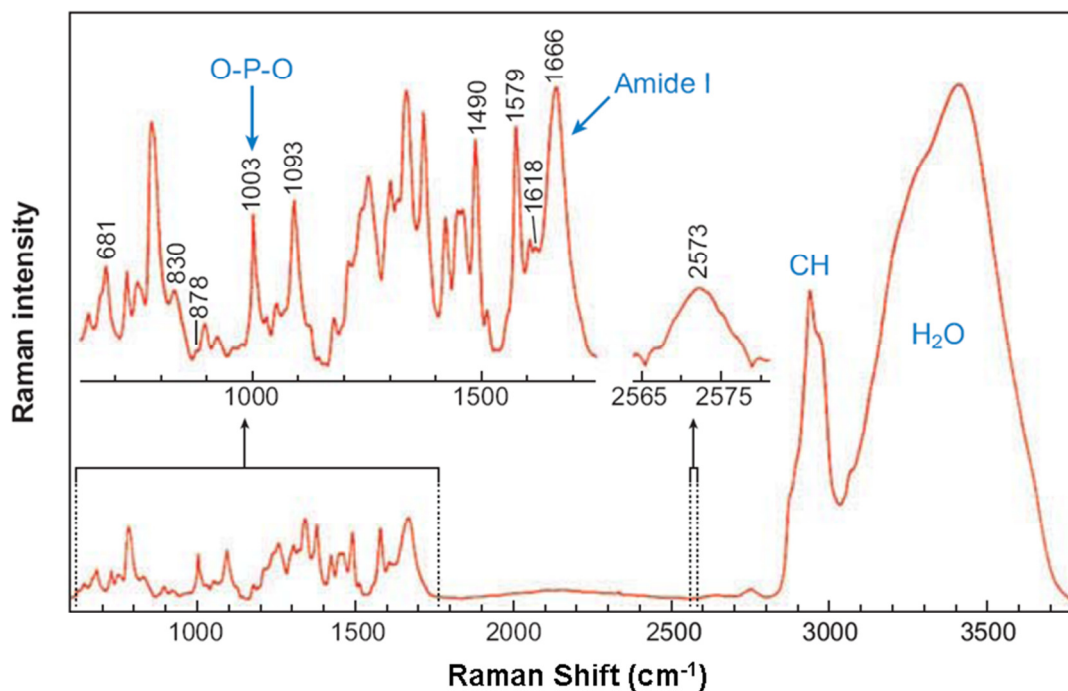


Fig. 2.2 Spontaneous Raman spectrum of the P22 virus, exhibiting the characteristic Raman modes typically observed in biological samples [44].

A typical spontaneous Raman spectrum of a biological sample is shown in Fig. 2.2. Raman spectra of biological samples exhibit a “silent region” between $\sim 1800\text{ cm}^{-1}$ and 2700 cm^{-1} where no Raman-active modes are present. The H_2O -stretching vibrations of water may be used for investigation of flow and density of water. The O-P-O stretching vibrational mode arises in this case from the DNA backbone. The CH-stretching band at around 2800 cm^{-1} is typically indicative of lipids and proteins. By deuterating compounds for use with biological samples, it is possible to obtain a C-D peak that is shifted away from the C-H peak, and into the “silent region”, at 2100 cm^{-1} . This can be particularly useful in mapping the location of specific compounds as a function of time within a sample, since there are typically no other modes present at this wavenumber range, however deuteration of compounds is very costly. The “fingerprint region” of the Raman spectrum for organic molecules falls between $\sim 500\text{ cm}^{-1}$ and 2000 cm^{-1} . This region is so-called because it typically contains the majority of the peaks that are used to determine the chemical makeup of a sample. The fingerprint region is often densely populated with peaks which may overlap, and hence is frequently spectrally congested. This can present a problem when attempting to resolve individual peaks; hence peak fitting algorithms are often employed.

Raman scattering has been used not only for spectroscopy, but also for vibrational imaging [45, 46]. However, this process is generally too slow to provide dynamical information on unfixed samples. Other biomedical applications of Raman scattering utilise its chemical specificity to distinguish between healthy and diseased tissues [47, 48]. Although very useful for determining information about a sample, Raman spectroscopy has several limitations. Firstly, in order for a chemical bond to be Raman active, it must satisfy the selection rules, which require the bond in question to have a non-zero polarisability derivative with respect to the normal coordinate. The selection criteria are discussed in more detail in Chapter 3, section 3.1. As a result of these selection rules, not all bonds will be Raman active and so this technique is limited to samples whose bonds of interest obey the criteria. For a chemical bond to be infrared (IR) active, the bond is required to have a non-zero dipole moment derivative with respect to the normal coordinate: hence, Raman and IR spectra are complementary.

Secondly, the Raman scattering cross section for most materials is relatively low and leads to signals that are typically 10^6 times lower than those obtained from fluorescence [41] so a large photon flux or laser scan time is required to achieve high signal-to-noise in the Raman spectra. This is unsuitable for samples which may photobleach or become damaged by exposure to high intensities of laser light. This is especially true for biological samples, whose structure may alter substantially under protein denaturation [38]. In this thesis, several methods for overcoming the limitations to Raman scattering are investigated. These include metal enhancement of the signal from Raman scattering (surface enhanced Raman scattering, SERS), coherent anti-Stokes Raman scattering (CARS) and stimulated Raman scattering (SRS). The historical context of the SERS effect will be explained in the following section.

2.5. Surface Enhanced Raman Scattering

Since the turn of the 20th Century, interesting optical effects from optically small metal interfaces and structures have been the subject of much scrutiny. Molecules adsorbed onto rough metal surfaces, particles or island films exhibit dramatically different optical

properties to those of the free molecules [49]. Perhaps the most widely known effect of this nature is surface enhanced Raman scattering (SERS) where the Raman signal from molecules adsorbed onto suitable metallic substrates can be millions of times stronger than that from the free molecule. The SERS effect has found wide application in biology, medicine, electrochemistry and materials science through such techniques as SERS of single molecules, nanostructures and transition metals, tip-enhanced Raman Scattering (TERS), surface-enhanced hyper-Raman scattering (SEHRS), ultraviolet-excited SERS (UV-SERS) [32]. Other examples of such metal enhancement exist, such as surface-enhanced infrared absorption [49] and plasmon enhanced spectroscopy [32].

The Raman scattering effect has been found to be greatly enhanced, by factors of up to 10^{14} in single-molecule SERS when compared with non-resonant Raman, although enhancement factors of between 10^4 - 10^6 are more commonly observed [50-52] when the sample is placed close to a metal surface exhibiting nanometre-scale structures. The greatest SERS enhancement comes from noble metal surfaces, such as gold and silver, since they have an abundance of free electrons which may become polarised in resonance with the incident radiation and molecules of interest. The factors contributing to SERS are described in more detail in Chapter 3, section 3.2.

The SERS effect was first discovered in 1974 by Fleischmann *et al.* whilst attempting to develop a chemically specific spectroscopic probe which could be used to study electrochemical processes *in situ* [53]. By roughening a silver electrode, they intended to increase the surface area available for molecular adsorption and hence obtain a larger Raman scattered signal. However, the signal they detected for pyridine adsorbed to the electrode was much larger than expected; the signal was a factor of $\sim 10^6$ larger than that measured in spontaneous Raman scattering [53]. Both Jeanmaire and Van Duyne [54] and Albrecht and Creighton [33] independently verified that this increased signal intensity could not be accounted for by the increased number of scatterers present alone. Instead, they proposed that when in the adsorbed state, there was an enhancement of the scattered intensity.

The causes that Jeanmaire and Van Duyne tentatively proposed for this surface enhancement were electric field enhancement mechanisms [54] whereas Albrecht and

Creighton posited that resonance Raman scattering from molecular electronic states broadened by their interaction with the metal surface might be the mechanism responsible [33]. Although the surface-enhancement effect of Raman scattering has now been known of for over 30 years, there is still much debate about the physical processes behind it. The explanations offered by Jeanmaire and Van Duyne and Albrecht and Creighton were found to be correct in concept, but not in detail. In the years following the discovery of SERS, research in this field accelerated dramatically until by 1985 it was generally accepted that electromagnetic and chemical enhancement were two of the most important processes involved in SERS [35, 42, 51, 55, 56].

The chemical enhancement mechanism is estimated to increase the surface enhancement by a factor of ~10-100 [34]. It is believed to involve the creation of “new electronic states due to adsorbate-substrate bonding interactions” leading to an increased absorption coefficient [34, 57]. The electromagnetic contribution to the SERS effect is thought to have a much higher contribution to the SERS effect, and is believed to be a result of surface plasmons. The first experiments involving surface plasmons [58] involved reflection of polarized light from a mirror with a diffraction grating on its surface. In 1907 Lord Rayleigh attempted to explain this experiment mathematically but his investigation gave “no hint of the enhanced reflection observed in certain cases by Professor Wood” [59]. A comprehensive explanation of the effect was finally given by Otto in 1968 [60].

Early suggestions by Moskovits and Chen *et al.* in 1985 that incident light waves impinging on rough or spherical metal surfaces can produce very large electric field amplitudes by exciting localized collective surface plasmon polaritons (LSPs) have led to thorough investigations into this electromagnetic mechanism of enhancement in SERS substrates [35, 51, 56, 61, 62]. The EM mechanism is believed to contribute to the enhancement via an increased local electric field at the surface of the metal which strongly polarises the adsorbed molecules on the metal’s surface. The Raman-shifted photons are also assumed to undergo a similar enhancement which combines with the direct field enhancement, leading to an enhancement factor of the order of 10^4 or above [62].

The SERS enhancement factor for a substrate may be calculated in a straightforward manner, provided the laser focal area/volume dimensions and the number of molecules in the focal volume can be calculated. An established method for determining the enhancement factor of SERS substrates made using metals that can form covalent bonds with sulphur, involves first taking a normal Raman spectrum of the liquid benzene thiol [63-66]. The Raman spectrum of benzene thiol is well characterised, with prominent bands at: 1583 cm^{-1} (C-C stretching), 1091 cm^{-1} (in plane C-C-C stretch and C-S stretching); 1001 cm^{-1} and 1025 cm^{-1} (out-of-plane C-C-C stretch) [64, 67]. Since the number of acquired counts for any given Raman band is directly proportional to the number of chemical bonds undergoing Raman scattering, it is possible to determine the number of counts per molecule.

Next, the procedure is repeated for the SERS substrate, once a self-assembled monolayer of benzene thiol has been formed on its surface. The calculated number of molecules of benzene thiol adsorbed onto the metal surface in the laser focal area is then used to determine the number of SERS counts produced by each molecule. A lower laser power and shorter scan time is used for SERS substrates than for normal Raman acquisitions, so the number of counts per molecule will have to be normalised against the parameters used in the normal Raman scan. By dividing the number of SERS counts per molecule by the number of Raman counts per molecule, the enhancement factor is determined. Since the density of the self-assembled monolayers are well characterised, this allows for a good estimate of the counts per minute from the sample.

2.6. SERS Substrates

Although the potential application of SERS in bio-chemistry is great, SERS substrates which yield consistently high signals have not been successfully developed until relatively recently [32, 68-70]. Metallic substrates with nanostructures suitable for use in Raman surface enhancement may be manufactured using a variety of techniques; oxidation/reduction roughening, vapour deposition of “island films”, cold-deposition of films, lithography, ion bombardment, acid etching, colloid formation etc.

A known requirement for SERS is that the frequencies of the incident radiation and scattered radiation must overlap the substrate's surface plasmon resonance frequency [71]. Much of the early work on SERS involved varying the incident laser's frequency in order to overlap the incident and scattered light's frequency with that of the substrate's surface plasmon resonance frequency. However, variation of the substrate's surface plasmon resonance frequency has been made possible by altering the metal thickness and the properties of the substrate's nano-topography [71].

A variety of production methods for macroscopically two dimensional SERS substrates have been developed, including chemical etching, electron-beam lithography, colloid immobilization, annealing of metal ion-implanted silicon, and nanosphere lithography [42, 69, 72, 73]. The substrates produced using these techniques provide reproducible SERS enhancement factors of the order of $10^5 - 10^7$. These production methods are generally prohibitively expensive, complex and ultimately unsuitable to mass production. Since the substrates' nanostructures are too delicate to withstand cleaning, they are only suitable for single use. For these reasons, cheaper, faster and more reproducible manufacturing processes are therefore required.

In search of more suitable methods for SERS substrate production, in recent years scientists have taken inspiration from nanostructures found in nature. One such investigation into the optical properties of cicada wings found that the "quasiperiodic" nanostructured anti-reflective coating on the chitinous wing surfaces provided an excellent SERS substrate, with enhancement factors of approximately 10^6 [74]. In chapter 4 of this thesis, details of our work investigating metal coated butterfly wing nanostructures for use as SERS substrates are given [75].

In order for the substrates to be suitable for use in SERS experiments, the nanostructures should ideally be regular and reproducible, however for high-throughput applications where 100,000 measurements are taken each day, the techniques required to produce such nanostructures tend to be prohibitively time consuming [19]. Commercially available SERS substrates are often manufactured using an ion beam lithographic method and are intended for single-use only, as their nanostructures are too

delicate to be cleaned. Due to the time consuming and specialised nature of the manufacturing process, substrates such as this can be prohibitively expensive for high throughput applications.

If a sample may be suspended in solution, colloidal gold and silver particles with diameters ranging from 10-100 nm are by far the easiest traditional means of providing surface enhancement, with enhancement factors of $>10^{12}$, since they may be manufactured using rapid, well-established reduction reactions [76, 77]. However, the colloidal particles need to aggregate in order to produce the surface enhancement, and nucleation during colloid preparation often inhibits control of particle size; hence reproducibility is difficult to achieve with colloids [35, 50, 78-80].

The surface enhancement effect is selective to molecules adsorbed on or near to the metal surface and hence neglects molecules in the bulk solution [42, 57]. This feature may be exploited using specific antibodies functionalised to the metal surface; any cell/molecule containing the complementary antigen will preferentially bind to the antigen, and hence provide a SERS signal.

Other, more recently developed approaches towards producing metallic substrates suitable for surface enhancement of molecules within a solution involves the use of a variety of novel nanostructures, including nanostars, nanorice, nanorods and nanoshells, which have diverse potential medical applications. These applications include: drug-delivery platforms, enhanced image contrast agents, chip-based nanolabs capable of monitoring and manipulating individual cells and nanoscale probes that track the motion of cells and individual molecules [78, 81-89]. These particles offer the benefit of a highly reproducible substrate combined with the ability to obtain SERS from solutions [90-92]. The nanoscale size of these structures enables them to readily interact with molecules in cells, often in ways which do not alter the cell's biochemical properties [29, 93]. Of these recently developed metallic nanoparticles, it is perhaps nanoshells that show the most promise for use in biophotonics since they are highly reproducible and biocompatible. In this thesis, nanoshells were used as contrast agents in live cell imaging and for photothermal ablation of cells. The method for production and the origin of gold nanoshell contrast are discussed in the following section.

2.6.1. Gold Nanoshells

Naomi Halas first discovered the photonic properties of silica spheres coated with gold shells in 1998 [78]. These gold nanoshells exhibit remarkable chemical, physical and optical properties which have been exploited for use in cancer treatment, cellular imaging and medical biosensing [94]. They have diameters ranging from 10 nm to 200 nm which increases the potential applications within the body for therapeutic purposes. Their optical properties arise predominantly from their nanoscale resonance profiles, which makes them ideal imaging contrast agents. By altering their shell thickness to dielectric core diameter ratio, the plasmon resonances of gold nanoshells may be tuned to preferentially absorb or scatter light of specific wavelengths in the desired regions of the spectrum. Thus, they can be manufactured to absorb or scatter light in the visible and near infrared regions of the spectrum, which enables exploitation of the NIR “tissue window” of optimal light penetration into tissue.

Gold nanoshells which are tuned to absorb NIR light efficiently convert the absorbed radiation into heat and are stable at therapeutic temperatures; hence they have been found to be particularly useful mediators of photothermal cancer therapy [89, 94, 95]. In treating cancers and for biosensing applications, the gold surface of the nanoshells may be functionalised to target tumours using monoclonal antibodies or other biomolecules. However, gold nanoshells have been found to accumulate at the site of tumours even when not conjugated in this manner, both as a result of their uptake into macrophage cells and direct deposition by the blood stream as a result of the leaky vasculature surrounding tumours [96]. The inert gold coating of the nanoshells also provides other benefits, including biocompatibility and nontoxicity [29].

Many researchers developing nanosphere experiments produced their own dielectric cores (e.g. silica, polystyrene etc.) for nanospheres, by the Stöber method [97]. This method enables nanospheres of the desired density and radii to be manufactured cost-effectively. Silica cores are also available commercially from a variety of companies which specialise in nanotechnology; in order to guarantee regular core diameters. Metallic shells may be grown on dielectric cores using a “seeding” method; the lone electron pairs of amine groups added to the dielectric core enable colloidal metal to

coordinate to them when added in solution with an appropriate reducing agent, producing small regular metallic deposits to form. These metallic “seeds” can act as nucleation sites when metal salt is added with more reducing agent (commonly citrate, or formaldehyde [81]), causing metal to build up and coalesce on the core’s surface ultimately resulting in a complete shell.

Using a method given by Mie scattering theory, one can calculate the absorption spectrum of any given sphere or core/shell composite, provided the refractive indices and thicknesses of the core and shell are known [78, 83, 88, 90]. Hence, the required shell thickness can be estimated from the peaks of absorption spectra. The Mie scattering theory is a solution to Maxwell’s equations for the scattering of electromagnetic radiation by small spherical particles. The calculated absorption spectra are valid for perfect spheres, however in practise they have shown good correlation with the measured spectra of “rough” nanoshells [78, 83, 88-90]. It is possible to “tune” the absorption peak for a nanoshell by altering the shell thickness: core diameter ratio [95].

Nanoshells have a wide range of potential medical applications, since they may be tailored to many specifications. Nanoshells that are smaller than 20nm in diameter have been found to cross the blood/brain barrier, and permeate through blood vessel walls, making them ideal to use as markers for medical imaging since traditional markers are simply too large to perform this task [29].

The nanoshell surface may be functionalised with a variety of chemical, molecular or biological entities, including antibodies, antigens, magnetic/radioactive markers, cell-specific drugs etc. This provides a means of controlling the nanoshells’ solubility, which in turn makes them excellent drug delivery platforms; therapeutic drugs which would be otherwise insoluble in the blood may be administered to patients via nanoshells functionalised with hydrophilic polymers to overcome the solubility barrier [29].

Chemotherapeutic chemicals may be delivered to tumours using nanoshells as “couriers”. Another use of nanoshells in tumour eradication uses lasers; the nanoshells’

surface plasmon wavelengths are tuned to the laser wavelength, and functionalised to be preferentially absorbed by cancerous tissue [89]. When laser light is shone on the tumour, the nanoshells within it cause it to heat more rapidly than surrounding healthy tissue, and thermal ablation occurs with minimal damage to non-cancerous tissues. The thermal profile of individual nanoshells embedded in a dried lipid bilayer has been monitored by Clarke *et al.* [98]. They found that under NIR excitation, the nanoshell heating caused a lipid phase transition which induced local liposome budding.

Although generally very thermally stable, when exposed to lasers of high fluence rates, nanoshells may undergo irreversible damage. The damage threshold of gold nanoshells tuned to an 800 nm resonance was investigated by Park *et al.* in the context of two photon imaging studies [99]. They found that under exposure to multiple Ti : sapphire 300 fs laser pulses at an average fluence rate of $9.06 \times 10^5 \text{ W cm}^{-2}$, nanoshells in solution remained intact. When the fluence rate was increased by a factor of three to $2.71 \times 10^6 \text{ W cm}^{-2}$, TEM images of the nanoshells revealed damage. An important point to note is that the laser fluence rates required for two photon imaging ($0.8 - 5 \times 10^5 \text{ W cm}^{-2}$) were found to be significantly lower than the damage threshold, thus enabling two photon imaging of the nanoshells without damaging the sample.

Further damage threshold experiments performed by Aguirre *et al.* using single pulses on nanoshells tuned to an 800 nm resonance, provided insight into the mechanisms responsible for nanoshell damage [100]. They found that the damage mechanism and threshold were dependant on the pulse duration and energy. For 9 ns pulses, total destruction of the nanoshells only occurred at energies above 0.005 mJ. This photo-fragmentation came about by excess positive charge resulting from ejection of electrons from the gold shell, which led to explosion of the shell due to Coulombic repulsion. For 300 fs pulses, at energies above 1.2 μJ the nanoshells were observed to melt; the energy absorbed from such a pulse corresponds with a lattice temperature of 1064 °C, which is the melting point of gold. Since heat diffusion is limited in the fs time regime, much lower energies are needed to destroy nanoshells under fs pulses as compared to ns pulses.

Another application for gold nanoshells involves their photoluminescent qualities. The luminescent properties of gold nanoshells have been found to compare favourably with those of standard quantum dots and fluorophores [94]. Park *et al.* performed photoluminescence studies in which they found that 120 nm gold nanoshells and 50 nm (long axis) gold nanorods were 140 times brighter than 100 nm fluoresceinated polystyrene beads, which are commonly used in biological imaging applications [101]. Wu *et al.* found the absorption of a single 20 nm diameter nanoshell to be equal to the absorption of 40,000 molecules of a photosensitizer, indocyanine green, used in photodynamic therapy.

A large number of biomedical applications have exploited the unique physical characteristics and benign toxicity profile of gold nanoshells. In cancer targeting, imaging and therapy, gold nanoshells have been shown to have great potential [89, 94]. Their photoluminescence properties have enabled them to be used for detection and imaging of individual cancer cells *in vitro* and in solid tumours *in vivo* [94]. The emission of heat by gold nanoshells under excitation by NIR light has been used successfully in animal studies to induce thermal necrosis of tumours [89, 92, 95], while their potential for use as thermal drug delivery agents has been demonstrated in temperature-sensitive hydrogels. In this thesis, gold nanoshells have been utilised as contrast agents within a variety of cell lines imaged using CARS. In addition, a laser power study was undertaken to determine the effect upon ablation of live cells.

2.7. Coherent Raman Scattering

The weak signal associated with Raman scattering may be enhanced by coherent excitation of vibrational modes within a sample. In this thesis, CARS and SRS are used as coherent mechanisms for providing enhanced signal from live cell lines and tissue samples in coherent Raman scattering microscopy experiments. Coherent anti-Stokes Raman scattering (CARS) is a third order nonlinear four-wave mixing process that was first reported by Maker and Tehune, at the Scientific Laboratory at the Ford Motor Company in 1965 [102]. Maker and Tehune investigated the third order response of several materials using two beams of light in a series of experiments they dubbed “three

wave mixing experiments”. A pulsed ruby laser provided light at ω which was passed through a Raman shifter to create a second beam at $\omega - \omega_v$. Both beams were directed onto the sample simultaneously; Maker and Tehune demonstrated that the intensity of the blue-shifted signal at $\omega + \omega_v$ increased significantly when the difference frequency, ω_v matched a Raman frequency of the sample. It wasn't until 1974 that the term coherent anti-Stokes Raman scattering was applied to this process [103]. Although discovered in 1965, it was not until 1999 with the work of Zumbush *et al.* and advances in ultrafast laser technology over the last ten years which have made the technology accessible.

CARS enhances Raman signals via nonlinear and coherent effects. A summary of the principles behind CARS are now given, although detailed explanation of the theory behind CARS is given in Chapter 3. In CARS, three coherent light beams referred to as the pump, probe and Stokes beams at frequencies ω_p , ω_{pr} and ω_s are used, although it is convenient to use the same laser for ω_p and ω_{pr} in what is known as “degenerate CARS”, to drive the Raman vibrational mode whose frequency is given by $\omega_R = \omega_p - \omega_s$ [102] producing an anti-Stokes photon with frequency $\omega_{AS} = 2\omega_p - \omega_s$. The interaction between these beams is shown schematically in Fig. 2.3. CARS produces signals about 10^5 times stronger than spontaneous Raman spectroscopy [102, 103] without the need to increase the laser power or scan times, although as a nonlinear form of enhancement it requires short pulses at high intensities. This is ideal for biological applications for which photodamage can be a major issue, provided that the non-linear mechanisms for photodamage are negligible. The CARS signal is proportional to the square of the modulus of the third order nonlinear susceptibility, $\chi^{(3)}$, as will be explained in Chapter 3, section 3.5.1.

Since $\chi^{(3)}$ is directly proportional to the number of oscillators, the CARS signal is therefore proportional to the square of the number of active chemical oscillators in the focal volume [104]. This leads to strong a signal from abundant chemical species such as CH_2 in lipid-rich structures. This is particularly useful for biological applications, since the cell membrane is predominantly composed of lipids. Other molecules with high bond repetitions are also excellent candidates for providing CARS signal.

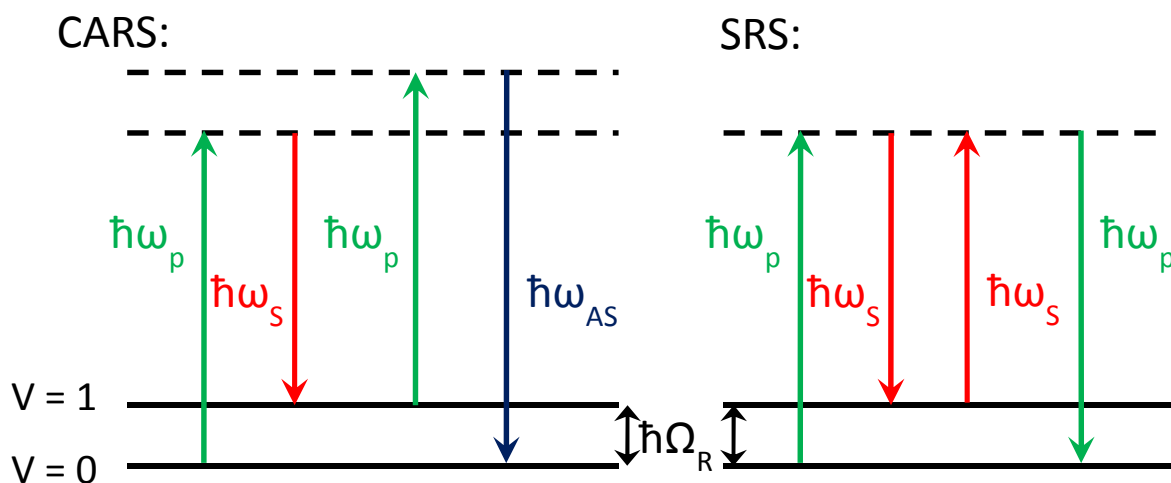


Fig. 2.3 Molecular energy level schematic for CARS and SRS depicting the interaction between the pump (ω_p), Stokes (ω_s) and anti-Stokes (ω_{AS}) beams. The dashed lines denote virtual states while the energy difference between the ground state ($V=0$) and first excited state ($V=1$) corresponds to a Raman resonance (Ω_R).

Although CARS offers a means for non-invasive, rapid chemically specific probing of biological samples with subcellular resolution, it is not without its limitations. CARS is a four wave mixing (FWM) process as it involves the combination of three input waves (two of which are the same in degenerate CARS) to produce a fourth output wave, as depicted in Fig. 2.3. As will be described in more detail in Chapter 3, the induced non-linear polarisation for all FWM processes is proportional to the third-order nonlinear susceptibility fourth rank tensor $\chi^{(3)}$. In CARS, the signal intensity scales with the squared modulus of the induced non-linear polarisation and hence is governed by the terms of $\chi^{(3)}$, which is the sum of the resonant (Raman) and nonresonant (electronic) contributions. The Raman resonance only enhances the FWM signal when $2\omega_p - \omega_s$ is tuned to match the Raman band frequency. Water produces a strong non-resonant CARS signal over a broad spectral range which gives rise to a substantial background for biological samples in aqueous environments [105].

The nonresonant background not only gives rise to noisy images, but it also distorts the spectral lineshape [106]. This means that Raman peaks do not correlate well with their CARS spectral profiles; the CARS peak is shifted away from the Raman peak by a

factor that is proportional to the Raman bandwidth (that is, the full width half maximum of the Raman spectral peak). This leads to difficulty in correlating CARS images with particular Raman modes in a sample, particularly for the fingerprint region where bands often overlap too closely to be distinguished with CARS. The nonresonant background therefore greatly hinders quantitative analysis of samples using CARS. In addition, the squared dependence of the signal upon the number of bonds in the sample also complicates quantitative analysis.

A variety of techniques for suppressing the nonresonant background have been employed, such as frequency modulation CARS, polarization CARS, phase-sensitive heterodyne CARS, multiplex CARS and epi-detected CARS, with varying degrees of success [105-110]. The back-detected (epi) signal in CARS displays much less nonresonant background and is preferable for imaging sub-wavelength particles than forwards- CARS. Volkmer *et al.* calculated the CARS signals in the forwards and epi directions and found that the epi CARS signal dropped while the forwards CARS signal increased and levelled off as the volume of scatterers grew to approach the same order of magnitude as the focal volume [106].

For aqueous samples, the bulk water acts as a large scatterer in the forwards-detected CARS signal throughout the focal volume; this property makes epi CARS more suitable for investigating features in biological samples that are smaller than the pump wavelength. Forwards CARS on the other hand provides information about the larger biological structures. In thicker samples, scattering of the forwards-CARS signal allows epi-detection of back-scattered forwards-CARS which can provide information about the bulk structures, but the images produced in this way are typically difficult to resolve.

While the complimentary information provided in forwards and epi-detected CARS can provide a wealth of information about the sample, the nonresonant background sometimes leads to a forwards-CARS image that is analogous to those obtained by phase-contrast microscopy, with little chemical specificity [111]. The nonresonant background, distortion of Raman spectral line shapes and nonlinear dependence of the signal to the concentration of the excited bonds in CARS imaging are major drawbacks

for quantitative analysis of biological samples. For instance, being able to discern the relative concentrations of drugs and their carrier polymers would pave the way for rapid, accurate and inexpensive pharmacokinetic studies.

Stimulated Raman scattering (SRS) is another non-linear coherent Raman scattering process, but unlike CARS it is background free. SRS is a two-photon stimulated process which allows for high chemical specificity without any nonresonant background [112, 113]. See Fig. 2.3 for a comparison of CARS and SRS the energy band diagrams.

The theory of stimulated Raman scattering is given in Chapter 3, but the basic principles will now be explained. In stimulated Raman scattering, the Raman medium makes a transition from the initial vibrational state to the excited vibrational state as one pump photon at ω_p is annihilated (stimulated Raman loss, SRL) and one Stokes photon ω_s is created (stimulated Raman gain, SRG) [113]. The SRS process may then be detected as a loss to the pump beam or a gain to the Stokes beam, as first observed in 1962 by Woodbury and Ng [114] and by Jones and Stoicheff in 1964 [113]. SRS has long been recognised as a highly sensitive method for spectroscopic analysis of chemicals in the condensed and gas phases [112].

As a nonlinear microscopy technique, it wasn't until 2007 that SRS's capabilities for chemically specific imaging of biological samples, without the presence of a nonresonant background, became apparent. In addition to the inherent lack of a nonresonant background, in SRS the spectral lineshape is identical to that of spontaneous Raman scattering which leads to much higher chemical specificity than in CARS [112, 113]. Quantitative analysis in CARS is rendered nontrivial by the nonlinear relation between the number of chemical oscillators and the signal intensity. This is not an issue in SRS since the signal is linearly proportional to the number of Raman oscillators in the focal volume [112, 113, 115], however the downside to this is that SRS doesn't benefit from increased signal from molecules with high bond repetitions. Although SRS provides an excellent means for background-free chemically specific imaging, current methods for SRS microscopy require relatively long scan times.

2.8. Contribution of this Thesis to the field

The experiments in this thesis use nanotechnology to enhance Raman-based biophotonics techniques. Chapter 5 explores the application of naturally occurring nanostructures and their biomimetic analogues to SERS, providing a new means for rapid, chemically-selective highly sensitive wet protein assaying. Chapters 6 and 7 explore the application of CRS to cell imaging, with emphasis on studying the interactions of cells and nanoparticles, and brain tissue imaging with emphasis on using novel techniques to probe the structure of the blood-brain barrier. It is hoped that the results gleaned from the experiments in this thesis will be pertinent to a wide range of fields, from drug delivery to medicine, forensics to optical biopsies, giving an improved insight into the scope for novel biological applications of Raman-based photonics techniques.

3. Theory

THIS CHAPTER PROVIDES AN outline of the main theoretical principles that have guided the work in this thesis. Since the work undertaken herein is concerned with enhancing the application of Raman techniques in Biology, it is pertinent to first consider the theory of spontaneous Raman scattering, which is given in section 3.1. The first means of enhancing Raman scattering that is considered in this thesis comes about by surface enhanced Raman scattering (SERS), the mechanisms behind which are explained in section 3.2, followed by the principles behind photoluminescence of gold nanoshells in section 3.3. Finally, the enhancement of Raman scattering by coherent scattering processes will be discussed in section 3.4.

3.1. Theory of Raman Scattering

Scattering of light from an object results in the redirection of the incident beam and may occur via a complex elastic or inelastic interaction between the incident electromagnetic wave and the object. The scatterer's electron orbits are periodically perturbed by the incident EM wave, resulting in an induced dipole moment with the same frequency (ν_o) as the electric field of the incident EM wave. Light incident on a sample will predominantly be scattered elastically via Rayleigh scattering, where the scattered photons have both the same frequency (ν_o) and energy (ϵ_0) as the incoming photons. However, a small number of photons undergo inelastic scattering, where the scattered and incident photons have different energies. Raman scattering is an inelastic scattering processes which occurs when the incoming photon interacts with the electric dipole of the molecule, resulting in a change in the molecule's vibrational or rotational energy.

The strength of the dipole moment, \mathbf{P} , induced in a scatterer is given by

$$\mathbf{P} = \alpha\mathbf{E} \tag{3.1}$$

where α is the polarisability tensor of the molecule, and \mathbf{E} is the electric field strength of the incident EM wave. The electric field of the incident EM wave is given by

$$\mathbf{E} = \mathbf{E}_0 \cos(2\pi\nu_0 t) \quad (3.2)$$

Where ν_0 is the frequency of the incident EM wave, given by $\nu_0 = \frac{c}{\lambda}$. The time-dependent induced dipole moment for a vibrating molecule depends upon the molecule's vibrational frequency ν_0 and is obtained by substituting (3.2) into (3.1),

$$\mathbf{P} = \alpha \mathbf{E}_0 \cos(2\pi\nu_0 t) \quad (3.3)$$

The incident EM wave's perturbation of the electron cloud of a given molecular structure is affected by the vibrational state of the molecule's atoms, hence the polarisability is also a function of the molecule's vibrational state. The vibrational modes are quantized, the energies of which are given by:

$$E_{vib} = \left(j + \frac{1}{2} \right) h \nu_{vib} \quad (3.4)$$

where j is the vibrational quantum number ($j = 0, 1, 2, \dots$), ν_{vib} is the vibrational mode frequency and h is Planck's constant. If the molecular oscillation is sinusoidal, the displacement of the atoms from their equilibrium position is given by

$$dQ = Q_0 \cos(2\pi\nu_{vib} t) \quad (3.5)$$

where Q_0 is the maximum possible atomic displacement from the equilibrium position (the normal coordinate amplitude) and is a scalar quantity. Given that the maximum possible displacement of an atom about its equilibrium position is small in comparison with the bond length, the polarisability can be approximated using a Taylor expansion,

$$\alpha = \alpha_0 + \frac{\partial \alpha}{\partial Q} dQ \quad (3.6)$$

where α_0 represents the equilibrium position's molecular mode polarisability and the derivative

$$\frac{\partial \alpha}{\partial Q},$$

corresponds to the change in polarisability with change in normal coordinate. Substituting (3.5) into (3.6) yields

$$\alpha = \alpha_0 + \frac{\partial \alpha}{\partial Q} Q_0 \cos(2\pi\nu_{\text{vib}}t) \quad (3.7)$$

Substitution of (3.7) into (3.3) provides the following expression for the time-induced dipole moment,

$$\mathbf{P} = \alpha_0 \mathbf{E}_0 \cos(2\pi\nu_0 t) + \frac{\partial \alpha}{\partial Q} Q_0 \mathbf{E}_0 \cos(2\pi\nu_0 t) \cos(2\pi\nu_{\text{vib}}t) \quad (3.8)$$

Since $\cos a \times \cos b = \frac{1}{2} (\cos(a + b) + \cos(a - b))$, (3.8) may be rewritten as

$$\mathbf{P} = \alpha_0 \mathbf{E}_0 \cos(2\pi\nu_0 t) + \left(\frac{\partial \alpha}{\partial Q} \frac{Q_0 \mathbf{E}_0}{2} \right) (\cos[2\pi(\nu_0 - \nu_{\text{vib}})t] + \cos[2\pi(\nu_0 + \nu_{\text{vib}})t]) \quad (3.9)$$

The first term in equation (3.9) relates to the outgoing elastically (Rayleigh or Mie) scattered photon. The second term contains two cosines, one of which corresponds to a photon with a lower energy after scattering ($\nu_0 - \nu_{\text{vib}}$) and the other to a photon with a higher energy after scattering ($\nu_0 + \nu_{\text{vib}}$). These are the processes of inelastic scattering that are referred to as Raman scattering; the down-shifted frequency (longer wavelength) scattering is termed Stokes scattering and the up-shifted frequency (shorter wavelength) scattering is anti-Stokes scattering. It is the vibrational state of the molecules undergoing Raman scattering that determines the ratio of Stokes to anti-Stokes scattering.

The selection criterion for a Raman scattering event to occur requires that the term $\frac{\partial \alpha}{\partial Q}$ must be non-zero along Q . This can be physically interpreted as the requirement that the change in polarisability of the atoms corresponding to a particular vibrational mode must result from their vibrational displacement by the incident EM wave.

Although Raman scattering is an attractive method for obtaining chemically selective information about a sample, spontaneous Raman scattering is a weak process. For condensed matter, the typical scattering cross section (the number of inelastically scattered photons per cm of material) for Stokes scattering is approximately 10^{-6} cm^{-1} . Hence for every 1 cm of material, merely 1 in every 10^6 photons of the incident radiation propagating through will undergo scattering into the Stokes frequency [41]. The Raman scattered signal is therefore a much weaker process than fluorescence, typically by a factor of $\sim 10^6$ [41].

The Raman scattering signal scales linearly with the number of molecular bonds within the focal volume. This can allow straightforward quantitative analysis of many samples, but given the weak scattering cross sections of most samples, it can also limit the sensitivity to milli-molar concentrations of analyte [32]. The spectra obtained with Raman scattering are also superimposed upon a fluorescence emission background, which can make resolving weak peaks in the spectrum challenging. The background generated by fluorescence can often be $10^6 - 10^8$ times stronger than the Raman signal itself [116].

The problem of the fluorescent background has been addressed by many researchers in the field of Raman spectroscopy. Selection of an excitation wavelength that is far from any electronic resonances in the sample is one relatively simple method that is often used in biological applications of Raman spectroscopy. To that end, near infrared excitation wavelengths have been found to effectively reduce the fluorescent background since the Raman spectrum produced is in a lower energetic region of the spectrum than the emitted fluorescence [117]. The disadvantage of this approach is that weaker signals are produced with NIR excitation wavelengths, since the intensity of the Raman scattered light is inversely proportional to the fourth power of the laser

wavelength. Therefore, in selecting the optimum excitation wavelength there is a trade-off between the ideal signal intensity and suppression of the fluorescent background.

In contrast to choosing NIR excitation wavelengths to reduce the fluorescent background, in resonance Raman scattering, the laser is tuned so that either the incident or the scattered light frequency matches or is close to an electronic transition frequency. Fluorescence in the sample can arise from impurities, especially for spectroscopic analysis of chemical compounds, so it is vital that all necessary purification has been undertaken prior to spectroscopic study. For samples with low fluorescence, shifted excitation Raman difference spectroscopy (SERDS) is sometimes used. In SERDS, two excitation wavelengths separated by an amount similar to the width of the Raman bands (typically $10 - 20 \text{ cm}^{-1}$) are used to produce Raman spectra of a sample. These spectra are then subtracted from each other to produce a different spectrum, the peaks in which are then reconstructed via numerical analysis [118].

Other methods for reducing the effect of the fluorescence background include: photobleaching the sample prior to obtaining spectra (which could potentially damage some samples); using a confocal setup to limit the amount of fluorescence entering the microscope; Fourier transform filtering; temporal gating. More recent methods have included a combination of Kerr gating and SERDS [118]. However, by far the simplest means of overcoming some of the issues posed by the fluorescence background is to subtract it from the spectrum using a baseline subtraction. This can be achieved using automated algorithms, or using computer software.

Fluorescence background issues aside, many approaches for improving the Raman scattering signal have been investigated. These range from resonance Raman scattering, stimulated Raman scattering, coherent anti-Stokes Raman scattering, heterodyne CARS to name but a few. Within this thesis, spontaneous Raman scattering, surface-enhanced Raman scattering (SERS), coherent anti-Stokes Raman scattering (CARS) and stimulated Raman scattering (SRS) are used to investigate biological samples combined with nanoparticles and nanostructures.

3.2. Surface Enhanced Raman Scattering Theory

The SERS effect is due to two contributing processes. Firstly, the introduction of a metallic nanostructure to the vicinity of the molecule in question will alter the chemical environment and hence change the Raman cross section. This contribution is known as the chemical enhancement, and will be discussed in more detail in section 3.2.2. The second, and more significant, process involved in SERS arises from the increased electromagnetic field in the vicinity of the metallic nanostructures. The nature of this EM contribution will be explored in section 3.2.1.

3.2.1. Electromagnetic Contribution to Surface Enhanced Scattering

The mechanisms responsible for the EM contribution to SERS are widely accepted to be due to localised E-field enhancements arising from the excitation of localised surface plasmons in nanostructured metals in combination with the so-called “lightning rod” effect. The lightning rod effect is purely an electrostatic effect due to geometric features of the substrate causing SERS enhancement as a result of crowding of the electric field lines in the vicinity of sharp metallic features. It has been shown to produce a local field enhancement even under conditions where no resonant localised surface plasmon excitation is taking place [119, 120].

To appreciate the contribution to the electromagnetic enhancement effect in SERS by surface plasmons (SPs), it is appropriate to first consider the nature of the surface plasmon polariton, or SPP. The surface plasmons may be thought of as a non-radiative collective oscillation of free electrons in a metal at the interface between the metal and a dielectric. Localised surface plasmons, or LSPs, are a special case of SPs in isolated or electromagnetically coupled metal nanostructures, such as surface cavities or protrusions or particles etc.

In essence, the SPP arises as a result of coupling between incident electromagnetic radiation and surface charge oscillations. In order for the necessary surface polarisation charge to be generated, there has to be a component of the electric field perpendicular

to the interface. Consequently, the SPP is a transverse magnetic (TM) mode. The fields associated with SPPs are highly localised at the interface between the metal and the dielectric and decay exponentially into the surrounding media. Typically, SPP fields are greatly enhanced with respect to the incident radiation, which is the mechanism responsible for the EM contribution to SERS. The surface topography and thickness of the metal used in SERS substrates have a great impact on the properties of the SPP and hence the enhancement factor.

The penetration depth of a surface plasmon polariton, commonly referred to as the skin depth, is defined as the distance perpendicular to the interface between a metal and a dielectric over which the field intensity drops to a fraction $1/e$ of its initial value, into the metal or surrounding medium. Expressions for the skin depth of the SPP mode into the metal and into the surrounding medium (e.g. water, air etc.) have been derived for a grating structure on a metal surface [121], and are given by:

$$\hat{y}_1 = \frac{\lambda_0}{2\pi} \left| \frac{\epsilon_{1r} + \epsilon_2}{\epsilon_{1r}^2} \right|^{1/2} \quad (3.10)$$

$$\hat{y}_2 = \frac{\lambda_0}{2\pi} \left| \frac{\epsilon_{1r} + \epsilon_2}{\epsilon_2^2} \right|^{1/2} \quad (3.11)$$

where \hat{y}_1 and \hat{y}_2 represent the penetration depth into the metal and the dielectric medium respectively, ϵ_{1r} is the real component of the complex permittivity for the metal, ϵ_2 is the complex permittivity for the dielectric medium and λ_0 is the wavelength of the incident light.

The macroscopically two dimensional SERS substrates used in this thesis were kept under a droplet of saline to facilitate protein binding. Given the dielectric constant of aqueous medium of 1.78 [94] and an excitation wavelength of 785 nm, substitution of the dielectric constants of silver, gold and water into equations (3.10) and (3.11) shows the penetration depth of silver to be around 22 nm, gold to be approximately 25 nm and the penetration depth into water is ~ 380 nm for the silver substrate and ~ 320 nm for

gold. Hence, the maximum EM enhancement contribution to the SERS enhancement will be achieved for molecules of < 380 nm in length that are adsorbed onto the metal, or for free molecules in solution that are within this distance of the metal surface. For a lower excitation wavelength, these penetration depths would be shorter, which illustrates the benefit of using NIR excitation wavelengths for SERS. Antibodies are some of the most commonly used proteins in biochemistry and they are typically less than 20 nm in length. The largest naturally occurring protein, titin, on the other hand, has a contour length of over 900 nm [122]. Generally, the sizes of most biological molecules used for investigation in biochemistry fall within the < 380 nm range allowed by this skin depth.

3.2.2. Chemical Enhancement in SERS

Changes to the adsorbate electronic states due to the chemisorptions of the analyte are believed to bring about the chemical enhancement (CE) in SERS. This effect has been described in a number of ways. The adsorption of the molecule of interest at the metal surface may produce pathways of electronic coupling leading to charge-transfer intermediates with higher Raman scattering cross sections. Another possible explanation is that the adsorbate's molecular orbitals broaden and overlap the conducting electrons of the metal, thus altering the chemistry of the analyte.

Whatever the mechanism behind the chemical enhancement, this process has been shown to typically provide between 10 and 100 x enhancement to the signal intensity, and is hence generally considered to be much less significant than the EM contribution [42, 51, 61, 123]. Determining the degree to which chemical enhancement takes place requires detailed knowledge of the electronic structure of the molecule-substrate complex together with the molecule's orientation with respect to the metal's surface structure. Thus in practice, for the majority of SERS systems this information is not only difficult to quantify theoretically, but moreover is very difficult to measure experimentally. However, in spite of these difficulties, there is much on-going theoretical and experimental study of this contribution to the SERS effect although to date there are very few general experimental strategies that have been shown to isolate and quantify the CE effects.

3.3. Photoluminescence

Many metallic nanoparticles exhibit enhanced photoluminescent properties which are mediated by localised surface plasmon resonance under exposure to the very high local fields used in ultrafast illumination. This effect is not usually observed in SERS since the high local fields required for photoluminescence are generally not required for SERS experiments. In contrast to conventional fluorophores, the photoluminescence provided by gold nanoshells has been shown to be immune from photobleaching and does not suffer from the “blinking” effects of intermittent emission from quantum dots [30, 94]. Therefore as contrast agents, gold nanoshells offer a stable, sensitive alternative to quantum dots and traditional fluorophores.

The metal luminescence arises from radiative recombination of electron-hole pairs at specific points in the Brillouin zone [101]. Visible photoluminescence occurs when electrons are excited from the d-band to the sp-conduction band via *interband* transitions causing radiative recombination of electron-hole pairs. NIR emission results from lower energy *intraband* transitions in conduction states below the Fermi surface causing radiative recombination of electron-hole pairs. The quantum efficiency for this photoluminescence process in smooth gold (bulk) films is on the order of 10^{-10} . The photoluminescence yield has been shown to increase by up to 10^6 times when the metal film is roughened, or when metallic nanoparticles such as nanorods or nanoshells are used, in a similar fashion to the enhancements observed for Raman scattering from such nanostructures.

The enhanced photoluminescence may be explained by considering the same enhanced localised fields due to the lightning rod effect and plasmon excitation as described in section 3.2.1. The strong field gradients brought about by this EM enhancement have the potential to excite electronic transitions within the metal which would ordinarily be forbidden. In addition, these fields have large enough associated wavenumbers to carry sufficient momentum for direct intraband transitions within the conduction band to be allowed. The energy from these transitions is able to radiatively decay into the far field due to the localized surface plasmons.

Another consequence of the coupling between the nanoshells and incident electromagnetic energy at the surface plasmon frequency is intense local heating, which has been exploited for photothermal ablation of cells and tissues [89, 91, 124, 125]. Nanoshells have been found to be generally very thermally stable, i.e. their core/shell structure maintains its integrity under exposure to light of therapeutic intensities. This is not the case for exposure to very high incident intensities; the nature of the damage threshold depends very strongly on the experimental conditions.

3.4. Plasmon Wavelength Tuning in Gold Nanoshells

To appreciate how it is possible to tune the peak plasmon resonance wavelength of gold nanoshells, the scattering and absorption properties of metal particles smaller than the wavelength of incident light must be taken into consideration. These properties are related to the dielectric function, which is not the same in bulk metals as it is for colloidal metals. The method for calculating the dielectric function of metals smaller than the wavelength of light impinging upon them, is given in section 3.4.1.

Once the dielectric functions of the metal shell and the dielectric core are known, one may calculate the extinction, scattering and absorption spectra of nanoshells, based on the core diameter, the shell thickness and the refractive index of the surrounding medium. The method employed to calculate these spectra employs Mie scattering theory and is qualitatively described in section 3.4.2.

3.4.1. Dielectric Function of Particles of Gold in the Mie Regime

The dielectric function of a metal is given as the sum of both the contribution from the metal's free electrons and the contribution from the interband transitions, with the free electrons' contribution given by the Drude free-electron model. The Drude free-electron model is reminiscent of the Lorentzian model for a harmonic oscillator, but in this case the spring constant is zero [126]. We start with the equation for a free electron:

$$m_e \frac{\partial^2 \mathbf{r}}{\partial t^2} + m_e \Gamma \frac{\partial \mathbf{r}}{\partial t} = e \mathbf{E}_0 e^{-i\omega t} \quad (3.12)$$

where e is the charge of the electron, m_e is the effective mass of the electron, $\mathbf{E} = \mathbf{E}_0 e^{-i\omega t}$ is the external electric field and Γ is the damping constant. The electron's displacement \mathbf{r} from its mean position is obtained by solving equation (3.12).

Taking the dipole moment as $\mathbf{p} = e\mathbf{r}$ and denoting the number of free electrons per unit volume as n then the polarization is $\mathbf{P} = n\mathbf{p}$. If the medium is assumed to be isotropic ($\mathbf{P} \parallel \mathbf{E}$) then the dielectric constant $\epsilon_F(\omega)$ contributed by the free electrons is given by

$$\epsilon_F(\omega) = 1 + \frac{|\mathbf{P}|}{\epsilon_0 |\mathbf{E}|}, \quad (3.13)$$

where ϵ_0 is the vacuum dielectric constant. From (3.12) and (3.13) the following expression is obtained for the dielectric constant:

$$\epsilon_f(\omega) = 1 - \frac{\omega_p^2}{\omega^2 + i\Gamma\omega} = 1 - \frac{\omega_p^2}{\omega^2 + \Gamma^2} + i \frac{\omega_p^2 \Gamma}{\omega(\omega^2 + \Gamma^2)}, \quad (3.14)$$

where ω_p is the Drude, or volume plasma frequency:

$$\omega_p = \left(\frac{ne^2}{\epsilon_0 m_e} \right)^{1/2}. \quad (3.15)$$

The damping constant Γ is related to the Fermi velocity v_F and the electron mean free path l by the following relation:

$$\Gamma = \frac{v_F}{l}.$$

Gold is a real metal and hence the dielectric function is contributed to by not only the free electrons, $\epsilon_F(\omega)$, but also interband transitions, $\epsilon_{ib}(\omega)$. In the case of gold these transitions are $3d \rightarrow 4sp$ with free electrons in the $4s$ state and the resulting absorption edge is in the visible range, which gives rise to gold's colouration. Hence, for bulk gold, the expression for the dielectric function that takes the interband transitions and free electron contributions is given by:

$$\varepsilon(\omega) = \varepsilon_F(\omega) + \varepsilon_{ib}(\omega) = 1 - \frac{\omega_p^2}{\omega^2 + i\Gamma\omega} + \varepsilon_{ib}(\omega). \quad (3.16)$$

This expression holds for bulk gold, but the dielectric constant deviates from this in the case of small particles of metal. When the metal particle's size is smaller than the electrons' mean free path (which for gold is ~ 42 nm [127]), then the electrons may collide with the metal particle's boundary. To account for this effect, the damping constant is given by

$$\Gamma = \Gamma_{\text{bulk}} + \frac{Av_F}{r_1},$$

Where Γ_{bulk} is the bulk metal damping constant, A is a constant and r_1 is the radius of the particle. The value of A depends on both the shape of the particle and the theory used and is usually approximately unity. Taking account of the size effect, and using experimentally determined bulk dielectric constant $\varepsilon_{\text{exp}}(\omega)$, the dielectric constant is now given by:

$$\varepsilon(\omega) = \varepsilon_{\text{exp}}(\omega) + \frac{\omega_p^2}{\omega^2 + i\Gamma_{\text{bulk}}\omega} - \frac{\omega_p^2}{\omega^2 + i\Gamma\omega}.$$

To obtain the plasma frequency and the damping constant, the following functions are fitted to the dielectric function (obtained experimentally in the NIR region) which are valid for $\omega \gg \Gamma_{\text{bulk}}$ where the influence of the interband transitions may be ignored:

$$\text{Re}[\varepsilon_1(\omega)] \simeq 1 - \frac{\omega_p^2}{\omega^2}, \quad \text{Im}[\varepsilon_2(\omega)] \simeq \frac{\omega_p^2}{\omega^3} \Gamma_{\text{bulk}}.$$

For gold, the plasma frequency ω_p is $13.8 \times 10^{15} \text{ s}^{-1}$, the relaxation constant τ is $1/\Gamma_{\text{bulk}} = 9.3 \times 10^{-15} \text{ s}$, and the Fermi velocity v_F is $1.39 \times 10^8 \text{ cm s}^{-1}$ [126]. The electronic transitions in gold are related to the complex dielectric constant ($\tilde{\varepsilon} = \varepsilon_1 + i\varepsilon_2$) and the complex refractive index ($\tilde{n} = n + ik$) in the following manner: $\tilde{\varepsilon} = \tilde{n}^2$. Hence the real and imaginary components of the dielectric function are given by $\varepsilon_1 = n^2 - k^2$ and $\varepsilon_2 = 2nk$. Using the values for n and k as obtained experimentally by Johnson and Christy [128] and taking the usual case that A is 1, the dielectric function of gold

including the size effect is obtained. From this, it is possible to calculate the dielectric function for a shell of gold surrounding a dielectric sphere.

3.4.2. Absorption, Scattering and Extinction

For cases where the sphere is smaller than the incident wavelength of light, Mie's scattering theory may be used to calculate the nanoshell LSPR wavelength. This theory involves solving Maxwell's equations analytically without any approximations, and uses boundary conditions for the surface of the sphere to obtain the scattering and absorption coefficients for a given dielectric core radius and gold shell thickness [129].

The term "extinction" (also occasionally referred to as "optical density" or "attenuance" in the literature [130]) as used in this thesis is intended to refer to the total attenuation of light. The extinction may be calculated by taking \log_{10} of the ratio of the incident light intensity. The overall extinction spectrum from a nanoshell is a combination of the nanoshell scattering and absorption properties. The absorption and scattering coefficients for a gold nanoshell surrounded by a medium of known refractive index have been determined elsewhere [130] and these calculations will be used in this thesis to determine the theoretical scattering spectrum for the nanoshells used in Chapter 6.

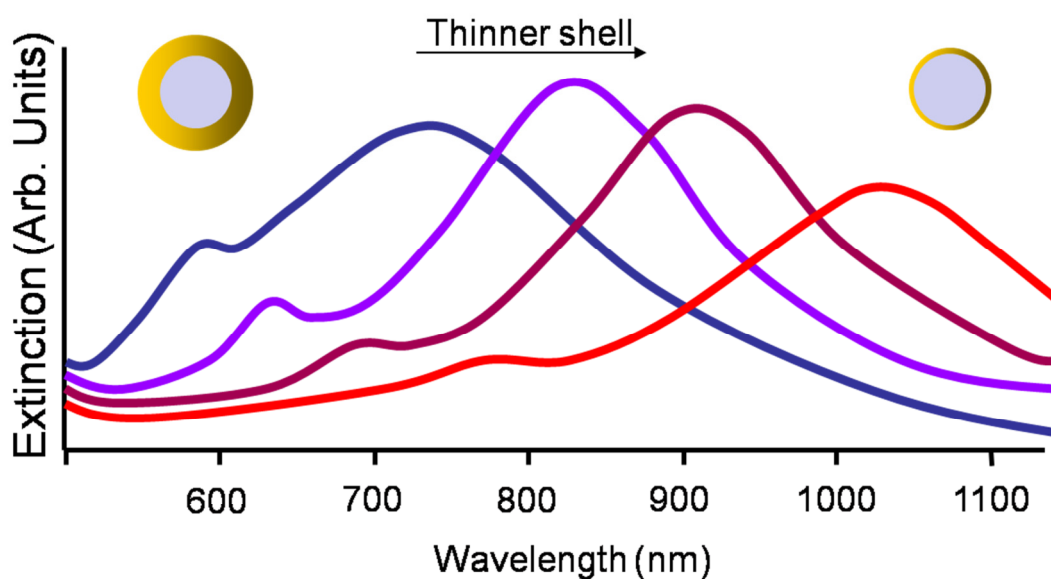


Fig. 3.1 Extinction spectra of nanoshells with varying shell thicknesses [95].

3.5. Coherent Raman Scattering

Coherent Raman scattering (CRS) processes can be used to enhance weak Raman bands in biological samples. The signal is boosted by nonlinear enhancement of the signal interactions of the incident laser light on a sample. In this thesis, two CRS processes are used; coherent anti-Stokes Raman scattering (CARS) and stimulated Raman scattering (SRS). The theory for both of these processes will now be given.

3.5.1. CARS Theory

CARS is a special case of four wave mixing, in which three electromagnetic fields interact to produce a fourth field. This may be physically understood by considering the individual field interactions within a dielectric medium. A description of the interaction between the first incident field and the medium is simply Rayleigh scattering as described by traditional linear optics. This first field will induce an oscillating polarization in the dielectric, which will be re-radiated with a phase shift determined by the individual dipoles' damping. The introduction of the second incident field also drives the dielectric's polarization. The resulting interference of these two waves causes harmonics at the sum and difference frequencies in the polarization. When the third incident field is applied, this also drives the polarization, which will beat with the first two incident fields, as well as with the sum and difference frequencies. The fourth field in four wave mixing arises from the beating with the sum and difference frequencies.

When modelling a material's linear optical response for a homogenous, linear and isotropic dielectric medium, equation (3.1) may be re-expressed as

$$\mathbf{P}(t) = \varepsilon_0 \chi^{(1)} \mathbf{E}(t) \quad (3.17)$$

where ε_0 is the permittivity of free space and $\chi^{(1)}$ is the linear susceptibility. The polarisability of individual particles as described in equation 3.1 is related to the polarization density and average susceptibility by the Clausius-Mossotti relation.

Although the equation 3.17 is valid for the linear process of Raman scattering, for nonlinear optics, one needs to consider higher order terms of the polarisation as expressed using a Taylor power series

$$\begin{aligned} \mathbf{P}(t) &= \epsilon_0 [\chi^{(1)} \mathbf{E}(t) + \chi^{(2)} \mathbf{E}^2(t) + \chi^{(3)} \mathbf{E}^3(t) + \dots] \\ &\equiv \mathbf{P}^{(1)}(t) + \mathbf{P}^{(2)}(t) + \mathbf{P}^{(3)}(t) + \dots. \end{aligned}$$

In this power series, $\chi^{(2)}$ and $\chi^{(3)}$ are the second- and third- order nonlinear susceptibilities, respectively, and $\mathbf{P}^{(3)}$ is the induced third-order non-linear polarisation.

The induced third-order non-linear polarisation may be expressed in the general form of:

$$\tilde{\mathbf{P}}^{(3)}(t) = \epsilon_0 \chi^{(3)} \tilde{\mathbf{E}}^3(t) \quad (3.18)$$

The applied field inducing this polarisation consists of three frequency components and their complex conjugates (c.c.)

$$\mathbf{E}(t) = E_1 e^{i\omega_1 t} + E_2 e^{i\omega_2 t} + E_3 e^{i\omega_3 t} + \text{c. c.} \quad (3.19)$$

If positive and negative (i.e. counter-propagating) frequency contributions are considered as distinct, there are 44 different frequency components in $\tilde{\mathbf{E}}^3(t)$. These frequencies are given as:

$$\begin{aligned} &\omega_1, \omega_2, \omega_3, 3\omega_1, 3\omega_2, 3\omega_3, (\omega_1 + \omega_2 + \omega_3), \\ &(\omega_1 + \omega_2 - \omega_3), (\omega_1 + \omega_3 - \omega_2), (\omega_2 + \omega_3 - \omega_1), \\ &(2\omega_1 \pm \omega_2), (2\omega_1 \pm \omega_3), (2\omega_2 \pm \omega_1), \\ &(2\omega_2 \pm \omega_3), (2\omega_3 \pm \omega_1), (2\omega_3 \pm \omega_2) \end{aligned} \quad (3.20)$$

and the negative of each. If the nonlinear polarization is represented as

$$\mathbf{P}^{(3)}(t) = \sum_{\mathbf{n}} P(\omega_{\mathbf{n}}) e^{-i\omega_{\mathbf{n}} t}, \quad (3.21)$$

then the complex contributions to the nonlinear polarization for each of the positive frequencies may be written as:

$$\begin{aligned}
\mathbf{P}(\omega_1) &= \epsilon_0 \chi^{(3)} (3E_1 E_1^* + 6E_2 E_2^* + 6E_3 E_3^*) E_1, \\
\mathbf{P}(\omega_2) &= \epsilon_0 \chi^{(3)} (6E_1 E_1^* + 3E_2 E_2^* + 6E_3 E_3^*) E_2, \\
\mathbf{P}(\omega_3) &= \epsilon_0 \chi^{(3)} (6E_1 E_1^* + 6E_2 E_2^* + 3E_3 E_3^*) E_3, \\
\mathbf{P}(3\omega_1) &= \epsilon_0 \chi^{(3)} E_1^3, \quad \mathbf{P}(3\omega_2) = \epsilon_0 \chi^{(3)} E_2^3, \quad \mathbf{P}(3\omega_3) = \epsilon_0 \chi^{(3)} E_3^3, \\
\mathbf{P}(\omega_1 + \omega_2 + \omega_3) &= 6\epsilon_0 \chi^{(3)} E_1 E_2 E_3, \\
\mathbf{P}(\omega_1 + \omega_2 - \omega_3) &= 6\epsilon_0 \chi^{(3)} E_1 E_2 E_3^*, \\
\mathbf{P}(\omega_1 + \omega_3 - \omega_2) &= 6\epsilon_0 \chi^{(3)} E_1 E_3 E_2^*, \\
\mathbf{P}(\omega_2 + \omega_3 - \omega_1) &= 6\epsilon_0 \chi^{(3)} E_2 E_3 E_1^*, \\
\mathbf{P}(2\omega_1 + \omega_2) &= 3\epsilon_0 \chi^{(3)} E_1^2 E_2, & \mathbf{P}(2\omega_1 + \omega_3) &= 3\epsilon_0 \chi^{(3)} E_1^2 E_3, \\
\mathbf{P}(2\omega_2 + \omega_1) &= 3\epsilon_0 \chi^{(3)} E_2^2 E_1, & \mathbf{P}(2\omega_2 + \omega_3) &= 3\epsilon_0 \chi^{(3)} E_2^2 E_3, \\
\mathbf{P}(2\omega_3 + \omega_1) &= 3\epsilon_0 \chi^{(3)} E_3^2 E_1, & \mathbf{P}(2\omega_3 + \omega_2) &= 3\epsilon_0 \chi^{(3)} E_3^2 E_2, \\
\mathbf{P}(2\omega_1 - \omega_2) &= 3\epsilon_0 \chi^{(3)} E_1^2 E_2^*, & \mathbf{P}(2\omega_1 - \omega_3) &= 3\epsilon_0 \chi^{(3)} E_1^2 E_3^*, \\
\mathbf{P}(2\omega_2 - \omega_1) &= 3\epsilon_0 \chi^{(3)} E_2^2 E_1^*, & \mathbf{P}(2\omega_2 - \omega_3) &= 3\epsilon_0 \chi^{(3)} E_2^2 E_3^*, \\
\mathbf{P}(2\omega_3 - \omega_1) &= 3\epsilon_0 \chi^{(3)} E_3^2 E_1^*, & \mathbf{P}(2\omega_3 - \omega_2) &= 3\epsilon_0 \chi^{(3)} E_3^2 E_2^*,
\end{aligned}$$

In each of the above equations, the frequency argument of the polarisation is equal to the sum of the frequencies on the right-hand side of the equation associated with the field amplitudes, when adopting the convention of the negative frequency being associated with a complex conjugate field amplitude. In addition, the numerical factor appearing in each term on the RHS of the equation equals the number of permutations to the field frequencies that contribute to the term in question.

These are all examples of parametric processes, meaning that the initial and final quantum states of the system are identical. Hence for parametric processes, according to the uncertainty principle, molecular bonds may only be removed from the ground state into virtual levels for brief periods of time on the order of $\hbar/\delta E$, where δE is the energy difference between the virtual level and the nearest real level. Non-parametric processes involve the transfer of a population between real energy levels, where the initial and final quantum states are not identical. Each of the processes in the above equations corresponds to a physical process. For degenerate cases, where two of the input fields are the same, these physical processes include third harmonic generation, sum frequency generation and second harmonic generation with difference frequency

generation. The CARS process is a special case of four wave mixing involving two incident coherent light beams of frequency ω_1 and ω_2 that are used to drive a vibrational Raman mode at frequency $\omega_R = \omega_1 - \omega_2$ the resulting signals generated are typically 10^5 times greater than in spontaneous Raman spectroscopy [102, 103]. The coherent beams, are generally referred to as the pump (ω_p) and the Stokes (ω_s) beams.

In CARS, the signal intensity scales with the squared modulus of the induced non-linear polarisation, $\mathbf{P}^{(3)} = E_p E_{pr} E_s \chi^{(3)}$ where E_p , E_{pr} and E_s are the pump probe and Stokes field amplitudes. As explained in Chapter 2, when using degenerate CARS, the same laser is used to provide both the pump and probe, so they both have the same frequency so $\mathbf{P}^{(3)} = E_p^2 E_s \chi^{(3)}$ and $I_{CARS} \propto I_p^2 I_s |\chi^{(3)}|^2$. The signal from CARS therefore scales linearly with the Stokes beam power and quadratically with the pump beam power. It is because of this nonlinearity that CARS signals are generated only by the regions of the sample that lie within the focal volume, in a similar manner to other nonlinear optical techniques. It is here that the photon flux is sufficiently great for a signal to be produced, hence CARS produces inherently 3D spatial resolution, negating the requirement for a confocal pinhole. The anti-Stokes signal is blue-shifted with respect to the incident light, which undergoes less scattering and allows for infrared excitation light which is therefore preferable for imaging thick tissue.

There are both resonant and non-resonant contributions to $\chi^{(3)}$. The non-resonant component to $\chi^{(3)}$ corresponds with contributions from bulk electronic vibrations that are independent of Raman shift, and the final term arises from two-photon enhanced contributions. The resonant contribution to $\chi^{(3)}$ is given by:

$$\chi_R^{(3)} = \frac{A_R}{\Omega_R - (\omega_p - \omega_s) - i\Gamma_R} = \frac{A_R}{\Delta - i\Gamma_R}, \quad (3.22)$$

where Ω_R corresponds to the Raman spectral line frequency with a half-width at half-maximum of Γ_R , and A_R is the Raman scattering cross-section constant, and Δ is referred to as the detuning. In a manner analogous to Raman shift representation, the detuning may be given as a frequency or (more commonly) in wavenumbers.

Combining these expressions gives

$$\chi^{(3)} = \frac{A_R}{\Delta - i\Gamma_R} + \chi_{NR}^{(3)} + \frac{A_T}{\omega_T - 2\omega_p - i\Gamma_T} \quad (3.23)$$

where

$$\chi^{(3)} = \chi_R^{(3)} + \chi_{NR}^{(3)} + \frac{A_T}{\omega_T - 2\omega_p - i\Gamma_T} \quad (3.24)$$

where ω_T is the frequency of the nonresonant two-photon electronic transition whose half-width at half-maximum is given by Γ_T , and A_T is the two-photon absorption cross section constant.

The two-photon enhanced term may be neglected when ω_p is tuned away from two-photon electronic transitions. This leads to an expression for the intensity of the CARS signal as follows:

$$I_{CARS} \propto |\chi^{(3)}|^2 = |\chi_R^{(3)}|^2 + |\chi_{NR}^{(3)}|^2 + 2\chi_{NR}^{(3)} \mathbf{Re}\{\chi_R^{(3)}\} \quad (3.25)$$

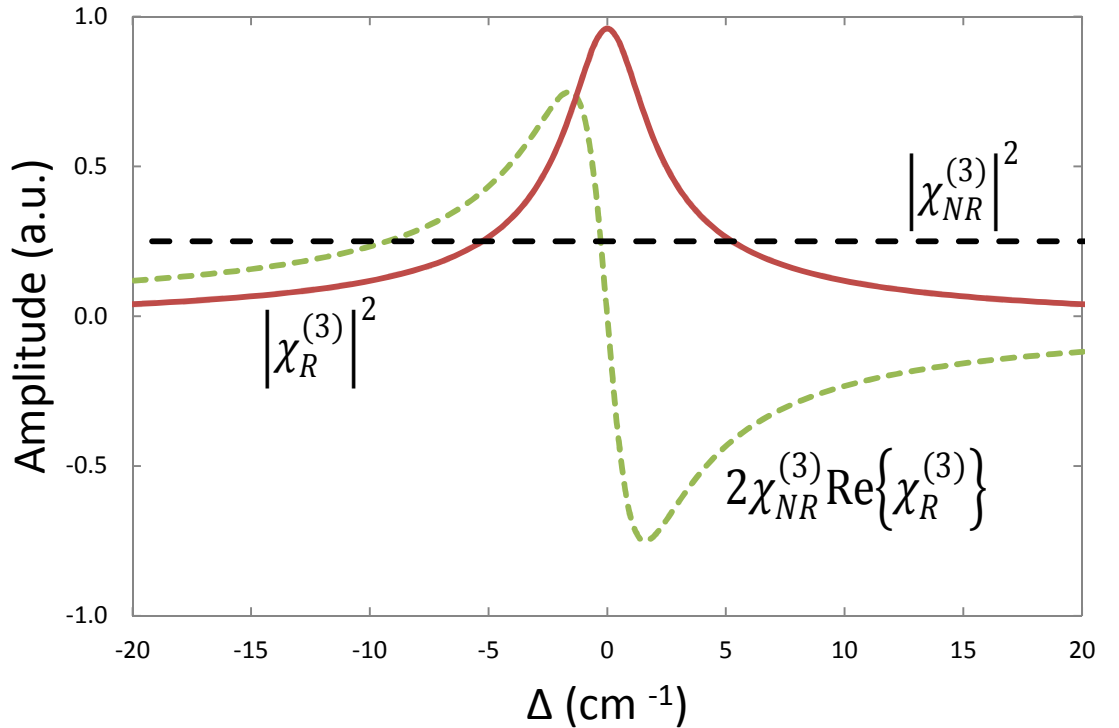


Fig. 3.2 The resonant, non-resonant and mixed contributions to the CARS signal as a function of detuning Δ , calculated using the equations in section 3.5.1, with a Lorentzian bandwidth Γ of 10 cm^{-1} .

The CARS spectrum is therefore composed of a resonant component $|\chi_R^{(3)}|^2$, a nonresonant component $|\chi_{NR}^{(3)}|^2$ and a combination of the two, the mixing term $2\chi_{NR}^{(3)}\text{Re}\{\chi_R^{(3)}\}$, as depicted in Fig. 3.2 and Fig. 3.3. The mixing term prevents simple subtraction of the nonresonant background, and causes the vibrational resonances in the CARS spectrum to have a dispersive line shape. When $(\omega_p - \omega_s) \gg \Omega_R$, the mixed term becomes negative, resulting in a decrease in the intensity of the CARS spectra when the Raman detuning is > 0 , as shown in Fig. 3.2.

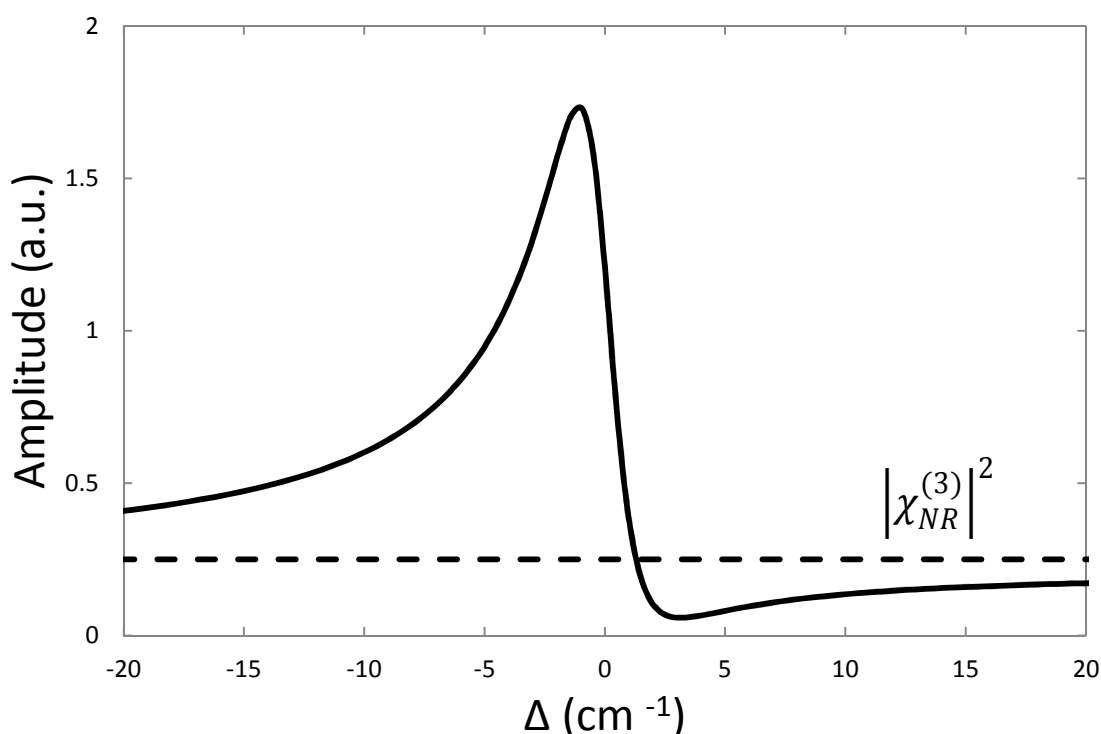


Fig. 3.3 The overall CARS signal intensity as a function of detuning Δ , calculated using the equations in section 3.5.1, with a Lorentzian bandwidth Γ of 10 cm^{-1} .

As illustrated in Fig. 3.3, the purely resonant contribution to the CARS intensity is the only term that produces a lineshape analogous to that of spontaneous Raman spectra. The intensity of spontaneous Raman scattering events has therefore been described by the following equation [131, 132]

$$I_{Raman} \propto \text{Im}\{\chi_R^{(3)}\} = \sum_R \frac{A_R \Gamma_R}{(\Omega_R - \omega)^2 + \Gamma_R^2}. \quad (3.26)$$

This equation should be used with caution since the nonlinear susceptibility refers to more quantum paths than are probed by the spontaneous Raman scattering process. However, this equation shows an important relationship between spontaneous Raman scattering and CARS; spontaneous Raman scattering probes the imaginary component of the resonant nonlinear susceptibility only. The nonresonant background can sometimes overwhelm the resonant signal in samples with weak vibrational resonances. This is especially true for biological samples where the nonresonant background from the aqueous environment can swamp the resonant signal. Several techniques have been developed to suppress the nonresonant background, including polarization-sensitive detection, time-resolved CARS, phase-sensitive techniques and epi-CARS, which involves relatively simple detection of the CARS signal in the backwards direction.

In spite of their signal arising from the same scatterers, epi-CARS and forwards-CARS signals exhibit significant differences that can be exploited for suppression of the nonresonant background. In epi-CARS, the signal waves are very phase mismatched which leads to destructive interference cancelling out the signal from the bulk medium. However, there are two cases where epi-signal may still be detected. The first arises from thick samples having different $\chi^{(3)}$ for the top half of the focal volume as for the bottom half. This results in breaking of the $\chi^{(3)}$ focus symmetry leading to incomplete destructive interference and back-reflection of signal by the interface between the different nonlinear susceptibilities. The second process by which epi-detected CARS occurs arises from objects smaller than the pump wavelength, with a different nonlinear susceptibility to their surroundings. Since the objects are smaller than the excitation wavelength, destructive interference is incomplete. Thus, while the nonresonant signal from the aqueous environment is suppressed due to destructive interference of the CARS signal, the small scatterer's signal is retained.

Assuming the pump and Stokes fields to be monochromatic plane waves travelling through a sample of thickness D along the z -axis, the CARS signal intensity propagating in the forward and backward directions is given by:

$$I_{CARS}(D) = \frac{\pi}{2n_{AS}c} \omega_{AS}^2 D^2 |\mathbf{P}^{(3)}|^2 \text{sinc}^2\left(\frac{|\Delta\mathbf{k}|D}{2}\right) \quad (3.27)$$

where $\mathbf{P}^{(3)}$ is the third-order induced polarization, c is the vacuum velocity of light, n_{AS} is the refractive index at the anti-Stokes angular frequency ω_{AS} [106].

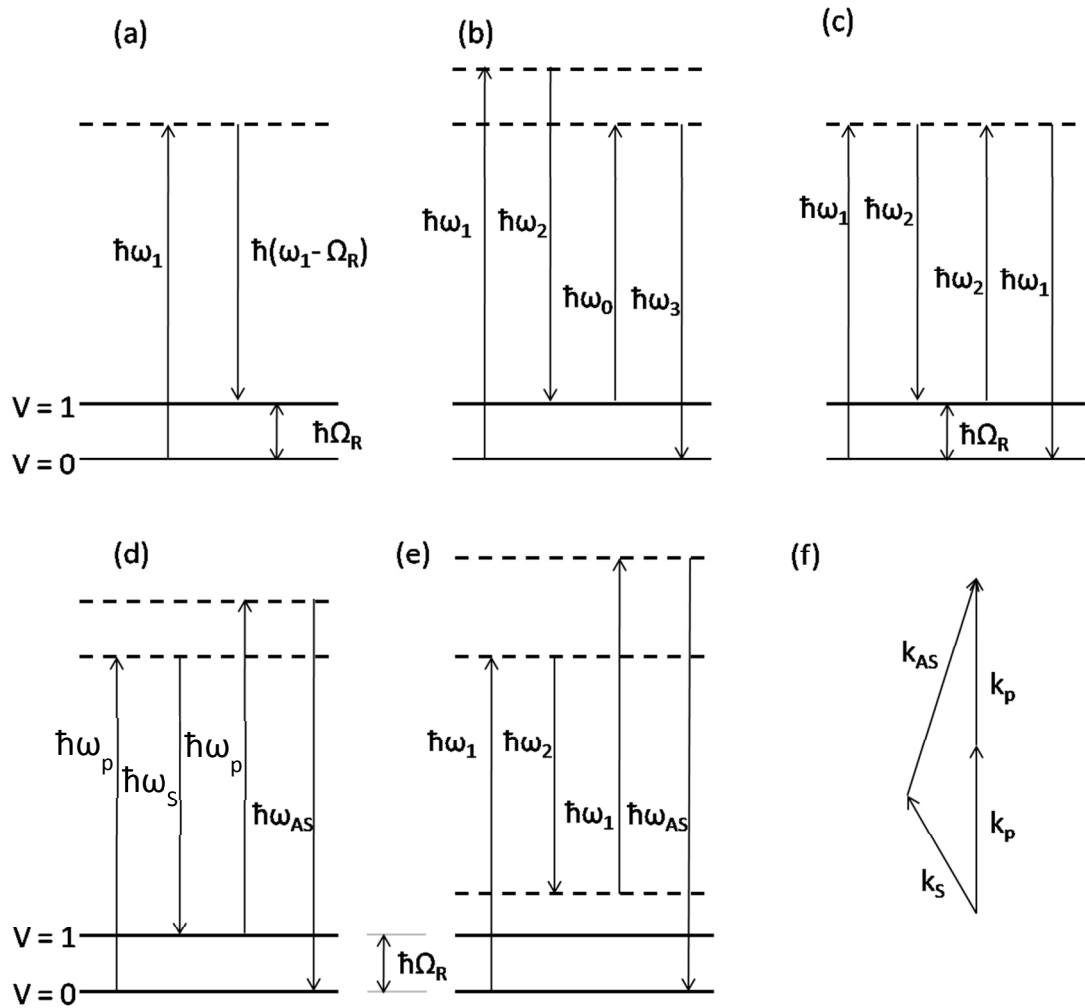


Fig. 3.4 Energy level diagram for (a) spontaneous Stokes Raman scattering, (b) general four wave mixing processes, (c) SRS, (d) resonant CARS, (e) nonresonant CARS from an electronic contribution, (f) the phase matching condition in CARS. The dashed lines denote virtual vibrational states.

The CARS phase mismatch in a slab sample of thickness D is represented by $\Delta\mathbf{k} = \mathbf{k}_{AS} - (2\mathbf{k}_p - \mathbf{k}_s)$ where \mathbf{k}_p , \mathbf{k}_s and \mathbf{k}_{AS} denote the wave vectors of the pump,

Stokes and anti-Stokes fields respectively as shown in Fig. 3.4 (f). These wave vectors are defined as $|\mathbf{k}_j| = 2\pi n_j / \lambda_j$ where λ_j is the vacuum wavelength and $j = P, S, AS$. The phase matching condition is $|\Delta\mathbf{k}|D \ll \pi$. The phase matching condition is satisfied in both the forward direction (\mathbf{k}_{AS} along the z direction) and backward direction (\mathbf{k}_{AS} along the $-z$ direction) for samples that are very thin, i.e. when $D \approx 0$. In this case, both the forward and backward CARS signals have equal intensity. For thicker samples, the forward signal begins to overwhelm the backward signal because of the constructive interference of the CARS waves emitted in the forward direction and the destructive interference of the CARS waves emitted in the backward direction [133].

If the dispersion of the refractive index is negligible ($n = n(\omega_{AS}) = n(\omega_P) = n(\omega_S)$), then ($|\Delta\mathbf{k}| = 0$) and the intensity of the anti-Stokes forward CARS signal, I_{AS}^F , has a quadratic dependence on D , $I_{AS}^F(D) \propto D^2$. Contribution to the signal from the solvent (large D) may, therefore, overwhelm the contribution from a thin sample (small D). In the case of epi-detected CARS ($|\Delta\mathbf{k}| = 4n\pi/\lambda_{AS}$), the intensity of the anti-Stokes signal oscillates as a function of D with a periodicity of $\lambda_{AS}/2n$, $I_{AS}^E(D) \propto \lambda_{AS}^2 \sin^2(2\pi n D / \lambda_{AS})$. The contribution from the solvent (large D) is significantly reduced as compared to that of the forward CARS signal. The fact that in the thin-sample-limit the forward- and backward-going CARS signals are equal, provides the basis for increasing the signal to background ratio for epi-detected CARS microscopy. In our setup the pump and Stokes signals are actually tightly focused beams and not plane waves as assumed in the above analysis; nonetheless, the physical picture described above is still true.

When imaging biological samples, care must be taken to keep photodamage to a minimum. This can be done by keeping laser powers low enough to keep transmitted energy to the sample at a safe level, but high enough to achieve a practical signal-to-noise ratio. For tissue samples, imaging is best undertaken over the wavelength range 700 – 1100 nm, due to the absorption of light by water, lipids and haemoglobin. At low laser powers, the observed quadratic dependence of photodamage to tissues in this wavelength range implies that two-photon absorption is the photodamage mechanism [134]. However at larger excitation powers, higher order mechanisms play a more significant role in photodamage. Picosecond pulses are generally preferred for biological imaging since greater powers can be used, and the two-photon photodamage effect is much more pronounced with femtosecond pulses.

For CARS imaging, there is a trade-off between obtaining larger laser powers from longer pulses and the efficiency of the CARS process, which drops as pulse width increases [134]. In CARS, the integrated signal intensity per pixel scales as

$$S_{\text{CARS}} \propto \frac{t_{\text{dwell}}}{(f\tau)^2} \langle P(t) \rangle^3, \quad (3.28)$$

where t_{dwell} is the pixel dwell time, f is the repetition rate, τ is the temporal width of the pump and Stokes pulses, and $\langle P(t) \rangle$ is the total time-integrated average power of the incident radiation. The largest CARS signals are hence obtained by using shorter pulses, when the average power of the pulse train is kept constant. The optimum pulse length has been found to be between 1 – 10 ps, since spectral band widths that are longer than the Γ lead to a decrease in the signal to noise ratio, due to the nonresonant background [112].

3.5.2. Stimulated Raman Scattering Theory

Stimulated Raman scattering (SRS) is another example of a coherent Raman process, with spatially and temporally overlapped pump and Stokes beams incident on the sample. As illustrated in Fig. 3.4 (c), when the frequency difference of the two beams matches a molecular vibration, a Stokes photon is generated by stimulated emission within the molecule. Therefore in SRS, the signal is not detected as an anti-Stokes shifted photon as in CARS, but as a gain or loss to the intensity of the pump or Stokes beams respectively.

SRS may be quantum mechanically described as a two-photon stimulated process that only occurs when the pump and Stokes beams are tuned so that their frequency difference matched a Raman-active mode in the sample. During SRS, one pump photon at ω_p is annihilated (stimulated Raman loss: SRL) as it excites the ground state electron into a virtual energy level, and one Stokes photon at ω_s is created (stimulated Raman gain: SRG) when the incident Stokes beam induces the electron to de-excite to

an energy level Ω above ground level, where Ω is the Raman mode frequency. During this process, the Raman medium makes a transition from the initial electronic ground state to the final vibrationally excited state. As a result of these processes, SRS is detected in the form of a gain or a loss of the Stokes and pump laser beams, as was first observed by Woodbury and Ng in 1962 [17] and by Jones and Stoicheff in 1964 [18],

The benefits offered by SRS over CARS for imaging are very attractive. Firstly, since the signal intensity scales linearly with the intensity of both excitation lasers and with the concentration of Raman active molecular vibrations within the focal volume, quantitative analysis is much simpler with SRS than with CARS. Secondly, since the SRS spectrum matches that of the spontaneous Raman spectrum, the distorted spectral line shape present in CARS is no longer an issue. This, combined with the inherent lack of a non-resonant background in SRS greatly increases the contrast of the images.

The spatial resolution in SRS is diffraction-limited and therefore analogous to that of two-photon fluorescence. SRL and SRG are measured at the same frequencies as those of the input beams, therefore the phase matching criterion is automatically fulfilled. This allows deconvolution with a point spread function similar to that of fluorescence microscopy. This simplifies image interpretation as compared with that involved in CARS, where the signal is “shaped by a complex interplay between the object size and coherent buildup dynamics” [112, 135].

To determine the signal intensity of SRL, following the treatment in [113] the pump and Stokes beams are considered as monochromatic plane waves which are collinearly propagating along the z-axis through an isotropic Raman-active sample with thickness L . When the difference frequency of the pump and Stokes beams, $\Delta\omega = \omega_p - \omega_s$ is tuned so that it matches a particular molecular vibrational frequency Ω (i.e. the Raman frequency), amplification of the Raman signal is achieved by means of stimulated excitation of molecular transition rate. The signal field generated in the slab of thickness L , $\mathbf{E}_{\text{sig}}(\omega_p, L)$ will be in the same mode as that of the input pump field $\mathbf{E}_p(\omega_p)$, yielding a total intensity at the detector of $I_p(\omega_p, L) \propto |\mathbf{E}_p(\omega_p) +$

$\mathbf{E}_{\text{sig}}(\omega_p, L)|^2$ [136]. The SRL signal is detected as a change in the optical pump intensity, which in the weak signal limit $\mathbf{E}_{\text{sig}}(\omega_p, L) \ll \mathbf{E}_p(\omega_p)$ is given by [137]

$$\begin{aligned} \Delta I_p(\omega_p) &= I_p(\omega_p, L) - I_p(\omega_p, 0) \\ &\approx -\frac{3\omega_p\mu_0}{n_p n_S \varepsilon_0} \text{Im} \left[\chi_{1111}^{(3), \text{SRL}}(-\omega_p; \omega_S, \omega_p, -\omega_S) \right] I_p(\omega_p, 0) I_S(\omega_S, L). \end{aligned} \quad (3.29)$$

In equation (3.29), the input intensities are assumed as being independent of the interaction length, n_p and n_S are the refractive indices of the medium at ω_p and ω_S respectively. I_S and I_p are the intensities of the Stokes and pump beams respectively. Because the imaginary part of equation (3.29) is greater than or equal to 0, the equation thus describes a pump intensity attenuation, which is shown schematically in Fig. 3.5. It is clear that by exchanging the p and S subscripts in equation (3.29), and using the SRL imaginary component (which is identical except for a “-” sign), the situation for SRL is described instead. When considering optically inactive and transparent media, using incident frequencies away from electronic transitions in the sample, if only the molecular ground state of the sample is populated, the selection rules are identical for both SRS and spontaneous Raman scattering.

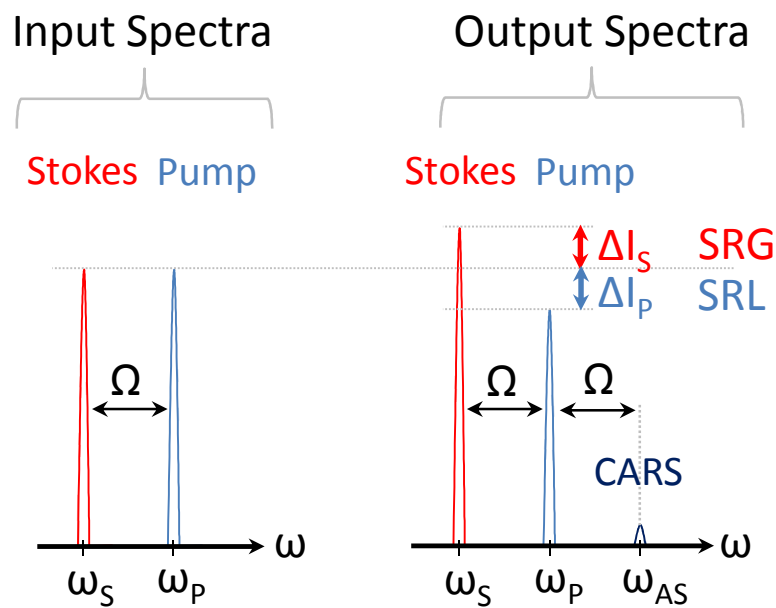


Fig. 3.5 Spectral profile for SRS, adapted from [112].

The signal in SRS thus scales linearly with the pump and Stokes laser intensities, and is linearly proportional to the spontaneous Raman scattering cross section and hence the number density of the Raman-active modes within the focal volume. Additionally, the signal is inherently insensitive to the real nonresonant background that is such an issue with CARS.

3.5.3. Application of CRS to Biophotonics

In this thesis, a variety of chemical bonds in biological samples were probed using CRS. For CARS, most notably the CH₂ stretching bond that is highly prevalent in lipids was used, due to the squared dependence of the signal upon the number of active bonds in the sample volume. The main limitations to detection of the anti-Stokes photons arise from the range of wavelengths for pump and Stokes pulses that can be produced, and from the choice of filters used to filter out the pump and probe beams from the signal, as well as the sensitivity of the detector (in this thesis, photomultiplier tubes are used, the characteristics of which are described in Chapter 4). A short summary of some of the principle Raman bands used for vibrational imaging and spectroscopy in biological samples, together with the excitation wavelengths that can be used to probe them, are given in the table below.

Vibrational Bond	Raman Band (cm ⁻¹)	CARS pump, Stokes and anti-Stokes wavelengths	SRS pump, Stokes and anti-Stokes wavelengths
CH ₂ stretching (e.g. lipids, proteins, carbohydrates etc.)	2845 - 2900	$\lambda_p = 924 \text{ nm} - 921 \text{ nm}$ $\lambda_s = 1254 \text{ nm} - 1260 \text{ nm}$ $\lambda_{AS} \sim 731 \text{ nm} - 725 \text{ nm}$	$\lambda_p = 813 \text{ nm} - 816 \text{ nm}$ $\lambda_s = 1064 \text{ nm}$ $\lambda_{AS} \sim 663 \text{ nm} - 658 \text{ nm}$
CD stretching in deuterated molecules	2200 - 2300	$\lambda_p = 952 \text{ nm} - 948 \text{ nm}$ $\lambda_s = 1205 \text{ nm} - 1212 \text{ nm}$ $\lambda_{AS} \sim 787 \text{ nm} - 778 \text{ nm}$	$\lambda_p = 862 \text{ nm} - 854 \text{ nm}$ $\lambda_s = 1064 \text{ nm}$ $\lambda_{AS} \sim 724 \text{ nm} - 714 \text{ nm}$
Centre of Amide I band (proteins)	1650	$\lambda_p = 978 \text{ nm}$ $\lambda_s = 1166 \text{ nm}$ $\lambda_{AS} \sim 842 \text{ nm}$	$\lambda_p = 921 \text{ nm}$ $\lambda_s = 1064 \text{ nm}$ $\lambda_{AS} \sim 787 \text{ nm}$
Fingerprint Region (amino acids, ring breathing vibrations etc.)	500 - 2000	$\lambda_p = 1036 \text{ nm} - 961 \text{ nm}$ $\lambda_s = 1093 \text{ nm} - 1190 \text{ nm}$ $\lambda_{AS} \sim 985 \text{ nm} - 806 \text{ nm}$	$\lambda_p = 1010 \text{ nm} - 877 \text{ nm}$ $\lambda_s = 1064 \text{ nm}$ $\lambda_{AS} \sim 961 \text{ nm} - 746 \text{ nm}$

4. Instrumentation

IN THIS CHAPTER, DETAILS of the main items of instrumentation used throughout this thesis are given. All spontaneous Raman spectra shown in chapters 5, 6 and 7 were taken using the Raman laser microspectrometer described in section 4.1 of this chapter. The CRS experiments described in chapters 6 and 7 of this thesis used the microscope and laser source described in section 4.2 of this chapter. Samples were prepared and characterised using the metal evaporators, the scanning electron microscope, the ultraviolet curing system and the spectrometer described in sections 4.3, 4.4, 4.5 and 4.6 respectively. Lastly, cell culturing was undertaken using the equipment explained in section 4.7 of this chapter.

4.1. Raman Laser Microspectrometer

The system used to take spontaneous Raman spectra was a Renishaw RM1000 Raman microscope (Renishaw, Wootton-Under-Edge, UK) equipped with a 1200 line/mm grating providing a spectral resolution of 1 cm^{-1} . A near infrared laser provided excitation at 785 nm with up to 300 mW power. The power of the light at the focus, as well as the laser scan times and spectral region of interest, were adjusted using a desktop computer installed with Renishaw v.1.2 WiRE software.

A variety of microscope objectives were available for use with this system, but the most suitable for our applications was a 40 x 0.55 NA microscope objective lens which was used to focus light onto the substrate. The sampling area provided by this lens was $< 10 \text{ }\mu\text{m}^2$. Prior to each experiment, the alignment of the laser passing through the microscope was checked and adjusted if necessary. Calibration of the system was undertaken before every set of experiments and once every 6 hours, by taking a spectrum of a silicon wafer and using the Raman band at 520 cm^{-1} as a reference peak. In this thesis, a least squares curve fitting function using multiple Voigt (Gaussian-Lorentzian mix) curves was used to assign peaks to Raman spectra.

4.2. Coherent Raman Scattering Setup

In nonlinear microscopy, the signal intensity scales nonlinearly with the illumination intensity, so the highest signals are obtained when high intensity lasers are used. However, high laser intensities can cause photodamage to delicate biological samples, so it makes sense to use pulsed lasers with high peak intensities and low average powers in order to limit the sample's exposure to the incident laser. The ideal pulse length of the laser depends on the application. In CRS, as explained in chapter 3, pulse lengths of between 1 and 10 ps are optimal, and the two incident lasers need to be perfectly spatially and temporally overlapped in order to produce CRS signal. Producing such perfectly overlapped beams can be a challenge when using traditional electronic locking mechanisms, and given that a range of wavelengths needs to be used in CRS to probe a variety of Raman bands, it becomes impractical to adjust the overlap manually.

Optical parametric oscillators (OPO) have proved to be well suited to CARS, since they use nonlinear optical crystals to convert an incoming photon into two output photons via non-critically phase matched optical parametric generation. To convert a high energy pump photon into two lower energy photons, OPOs use a nonlinear gain medium with a large second order susceptibility, and the wavelengths of the signal and idler beams may be altered by adjusting the phase matching qualities of the crystal, either by changing its temperature or orientation with respect to the pump beam. The output photons are the so-called "signal" and "idler" photons, where the higher frequency is the signal. The sum of the output photon frequencies equals that of the input photon, $\omega_i + \omega_s = \omega_p$. The signal and idler beams are intrinsically spatially and temporally overlapped, and this combined with the tunability provides an ideal source of the pump and Stokes beams used in CARS.

For the pulsed laser source, a Levante OPO (High-Q Picotrain, Hohenems, Austria) pumped with a neodymium-vanadium source was chosen. The Nd:Vanadium source used (High-Q Picotrain, Hohenems, Austria) provides a 6 ps pulse width laser beam with a wavelength of 1064 nm which is frequency doubled to 532 nm. The power from this source is up to 10 W with a repetition rate of 76 MHz. The OPO was used to

convert the incoming 532 nm pump beam into two outputs (the signal and idler beams) which are required for CARS generation. These pump (signal) and Stokes (idler) beams are tuneable from 690 to 990 nm and 1150 to 2300 nm respectively.

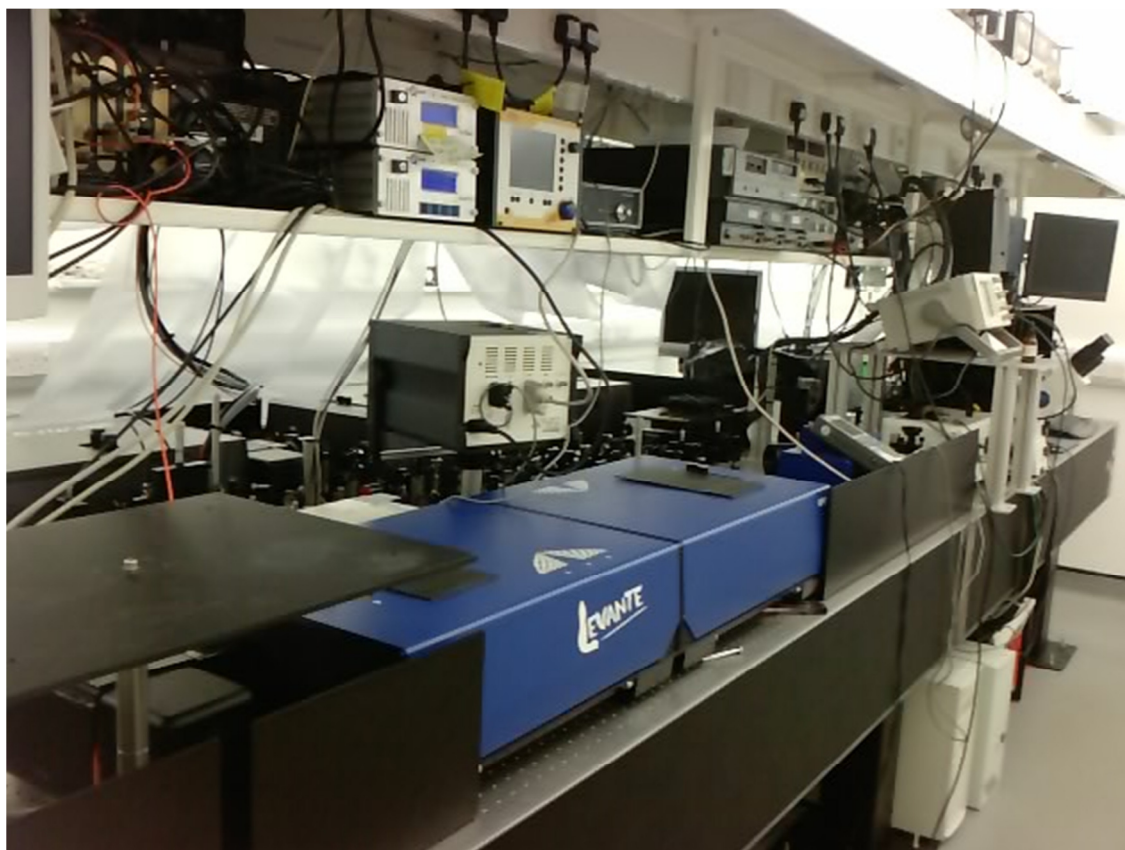


Fig. 4.1 The Coherent Raman scattering system at the University of Exeter.

The microscope used was a modified commercial Olympus IX71 inverted microscope with a customised confocal Fluoview 300 scan unit, as depicted in Fig. 4.2. This microscope allowed imaging in the forwards and back-scattered directions. Within the scanning unit, the standard galvanometer scanning mirrors were replaced with silver galvanometric mirrors to maximise the NIR throughput, and the tube lens was replaced with an MgF₂-coated lens. A silver mirror with high reflectivity through the visible and NIR wavelengths (21010, Chroma Technologies) was used to replace the confocal dichroic.

In this thesis, the objectives used with this microscope are an Olympus UPLSAPO 60 x 1.2 NA water immersion objective (UPlanS Apo, Olympus UK) and a 40 x 0.8 NA

objective (UPlanS Apo, Olympus UK). Although the 60 x objective gives a maximum scan size of $260 \times 260 \mu\text{m}$, due to chromatic aberration arising from the different pump and Stokes wavelengths CARS signals are only obtained in 80% of this field of view.

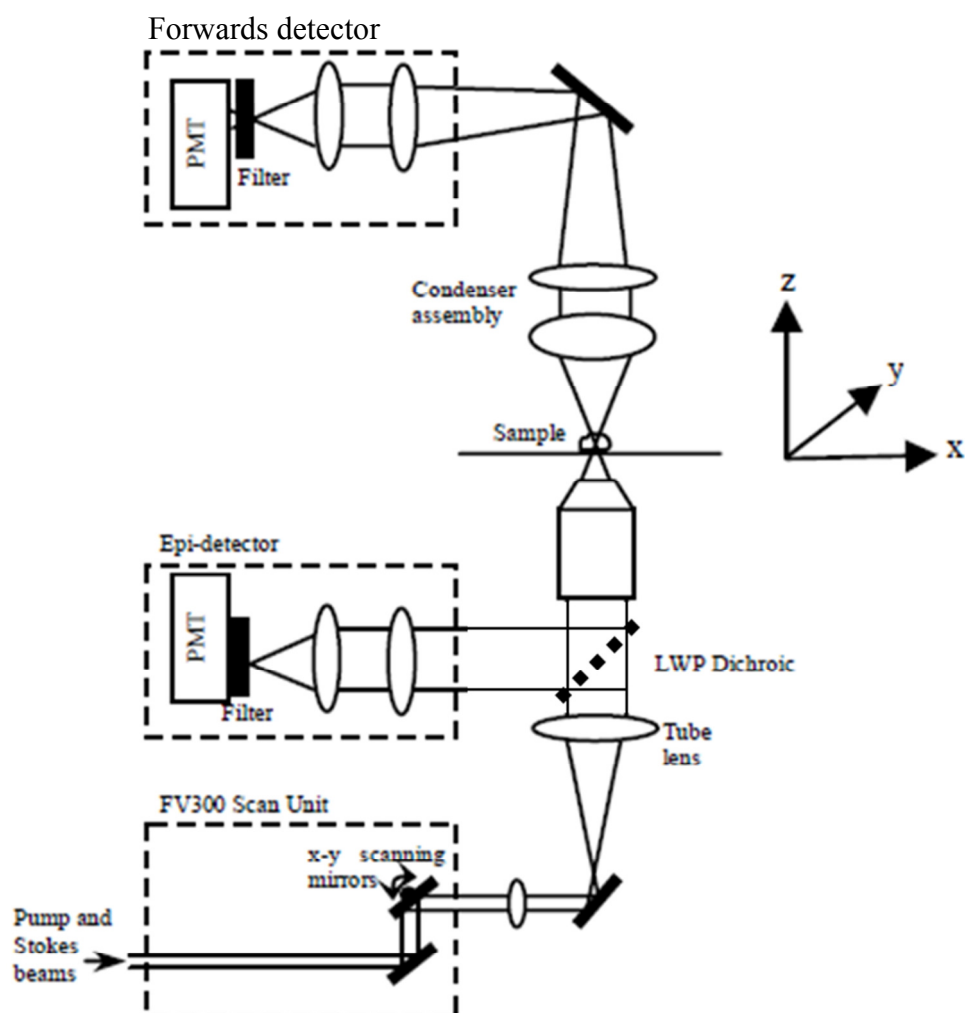


Fig. 4.2 Schematic diagram of the CARS microscope [138].

The optical beam paths for the 1064 nm, signal and idler beams are shown in the schematic diagram in Fig. 4.3. The power of the 1064 nm beam entering the electro-optic modulator (EOM) is adjusted to ensure that the safe threshold of $< 1 \text{ W}$ is maintained, thus averting damage to the EOM. The delay stages allow for control over the overlap between the beams, to enable optimum CARS and SRS signal to be obtained. Correct alignment of all three beams is crucial to producing a high intensity signal, and a higher signal to noise ratio in the resulting sample images.

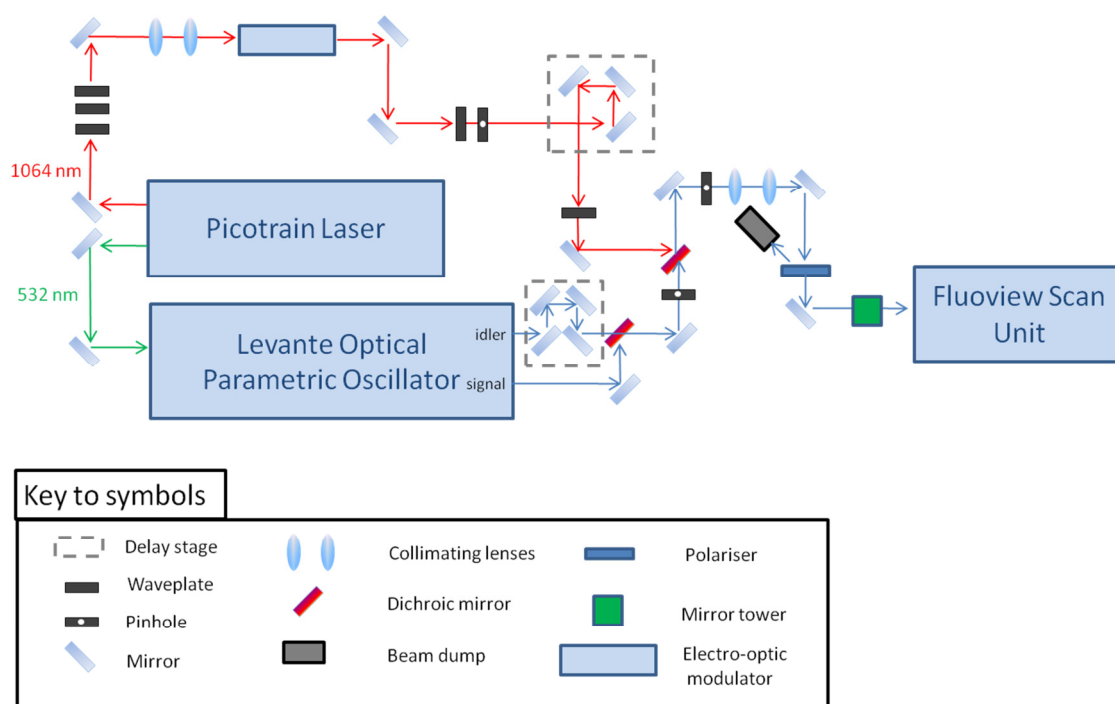


Fig. 4.3 Schematic diagram of the optical bench.

As explained earlier in the theory of epi-CARS, detection of both forwards- and epi-detected CARS signal is desirable. To that end, the forward-CARS signal was collected by an air condenser (NA=0.55) and directed onto a red-sensitive photomultiplier tube (R3896, Hamamatsu) via a mirror and collimating lenses. The epi-CARS signal was collected using the objective lens and was separated from the pump and Stokes beams by a long-wave pass dichroic mirror (z850rdc-xr, Chroma Technologies) before being directed onto a second R3896 photomultiplier tube at the rear microscope port. The transmission profile for this filter is shown in Fig. 4.4; note that 50% transmission efficiency is obtained at ~ 850 nm, dropping off rapidly for longer wavelengths.

The anti-Stokes signal was isolated at each photodetector by a single band-pass filter centered at 750 nm (HQ750/210, Chroma Technologies), the transmission profile for which is given in Fig. 4.5. The original detectors internal to the scan unit were replaced by external, non-descanned detection, which gave the advantage of increased efficiency for deep tissue imaging. In descanned imaging, used for confocal microscopy, emitted light returns to the detector along the same path as the excitation light. Non-descanned

imaging by contrast allows for the collection of more scattered photons from the sample, reduces the path length and requires fewer optical components, thus increasing the collection efficiency.

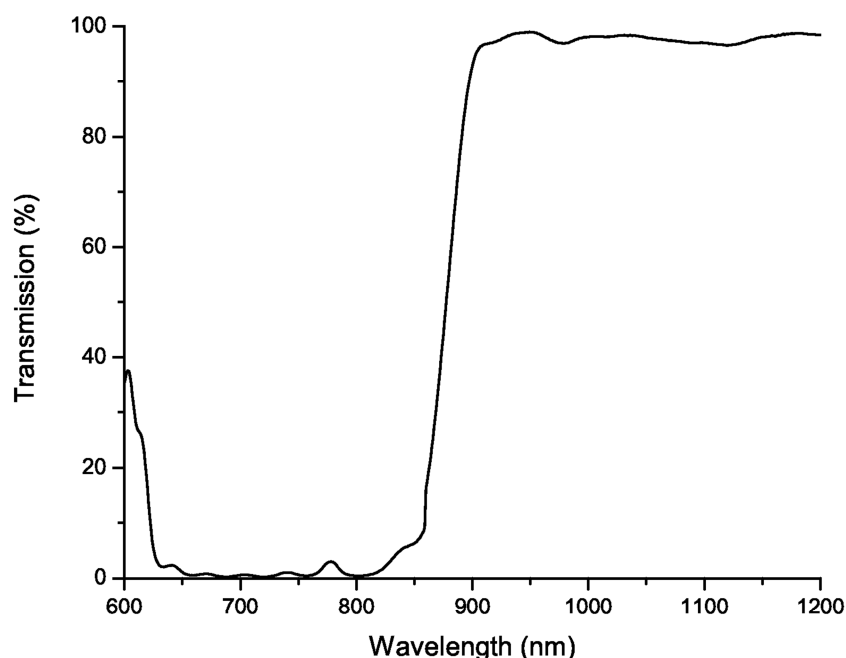


Fig. 4.4 Transmission profile for Chroma Z850rdc-xr long pass dichroic filter, data supplied by the manufacturers.

The SRS setup in Exeter's Biomedical Physics group has been developed using a pump beam provided by the same OPO as used in our CARS setup, which is tuneable between 690 and 990 nm. The Stokes beam is provided by a remnant of the non frequency-doubled 1064 nm mode-locked Nd:Vanadium source which is also used to pump the OPO (High-Q Picotrain, Hohenems, Austria). The repetition rate of these two wavelengths is 76 MHz with a pulse width of 6 ps.

The frequency bandwidth provided by pulses at 6 ps is ideal for SRS since the spectral resolution is 3 cm^{-1} , which is less than the width of a typical Raman peak from a room-temperature sample. The combination of the pump and Stokes beams in SRS can potentially probe Raman peak range between 5090 cm^{-1} and 702 cm^{-1} although the

range that is detectable is limited by the filters used to separate the Stokes beam from the pump beam. In these excitation conditions, the SRG and SRL signals are smaller in intensity than the low-frequency laser noise ($\Delta I_p/I_p$ and $\Delta I_s/I_s < 10^{-4}$).

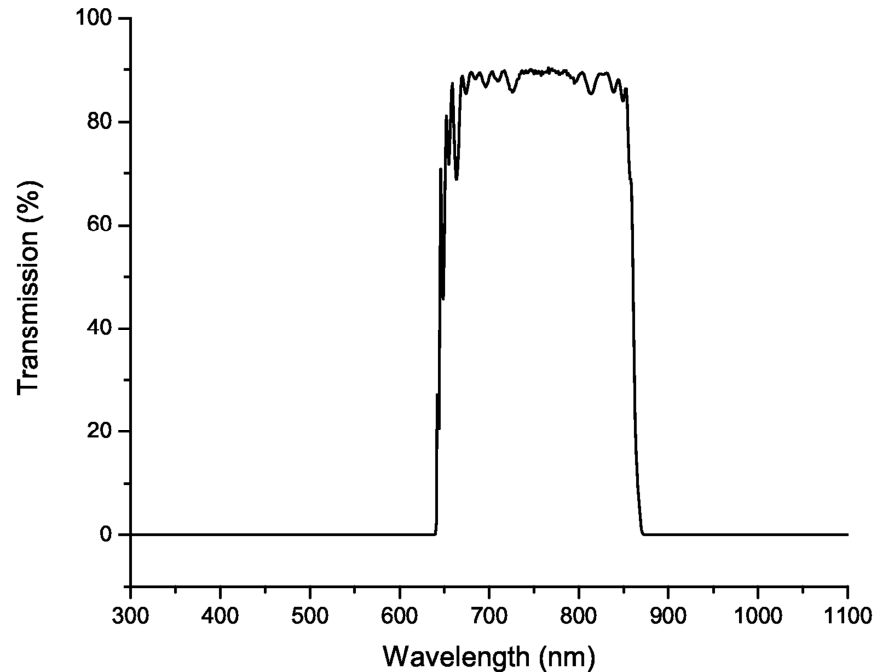


Fig. 4.5 Transmission profile for Chroma HQ750/210 750 nm bandpass filter, data supplied by manufacturers.

Because the laser noise is at low frequencies, this issue can be overcome using a high-frequency phase-sensitive detection scheme. In our setup, we opted for modulation of the Stokes beam intensity at a frequency of 1.7 MHz using an electro-optical modulating Pockel's cell (Leysop, EM200). By detecting the subsequent modulation in intensity of the pump beam at this frequency using a lock-in amplifier (Stanford Research, SR844RF), the SRL signal was measured. The laser intensity profile for SRG and SRL is depicted schematically in Fig. 4.6.

The pump and Stokes beams were directed into the microscope in exactly the same manner as for our CARS setup using a modified commercial inverted microscope and confocal laser scanner (IX71 and FV300, Olympus UK), so that F-CARS images could be taken of samples after SRS images by just removing the SRS detector and re-

installing the condenser. Both the pump and Stokes beams were expanded to fill the back aperture of the microscope objective before being combined on a dichroic beam combiner and directed into an inverted microscope. The objective lens used depended on the sample to be imaged. Larger tissues were generally imaged using the 40 x 0.8 NA objective (UPlanS Apo, Olympus UK) lenses whereas cells and smaller structures were imaged using the 60 x lens.

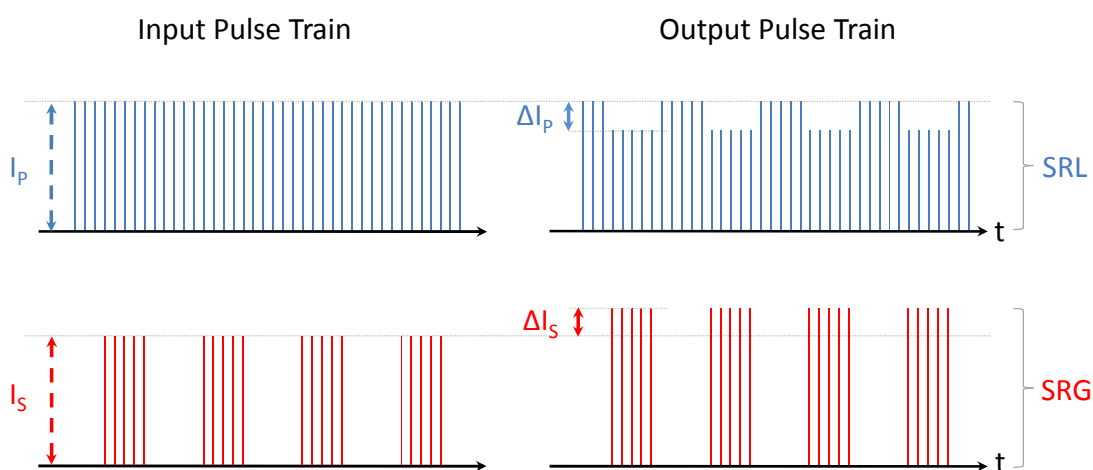


Fig. 4.6 Laser intensity profile for SRS.

The transmitted pump beam was collected in the forward direction by a second objective lens (Nikon Fluor 60 x, 1.0NA) and spectrally isolated from the Stokes beam by a band-pass filter (Chroma, CARS 890/220 nm). The modulation of the pump intensity due to SRL is detected by a wide area Si photodiode (Thorlabs, FDS1010) with a reverse bias of 64V. The output current is then filtered using a low-pass filter (Mini-Circuits, BLP-1.9+) to suppress the strong signal due to the laser pulsing (76 MHz), and then terminated with a 50 Ω resistor. A radio-frequency lock-in amplifier (Stanford Research, SR844RF) is used to demodulate the pump-intensity. The analog R (i.e. modulus) or X (i.e. in phase component) output of the lock-in amplifier is fed into a modified input of the microscopy A/D converter.

The detection scheme we used is based on stimulated Raman loss since the photodiode detector is more sensitive to the pump beam than the Stokes beam. Images were recorded with a pixel dwell time of 100 microseconds, equal to the fastest integration

time available with the lock-in amplifier. For focusing using faster scan rates, the output from the diode was diverted prior to the lock-in amplifier and used to provide a transmitted light image of the sample. The collinear pump and Stokes beams are focused with a high NA objective onto a common focal spot and the SRS detector is positioned so that the back focal plane is at the diode's surface.

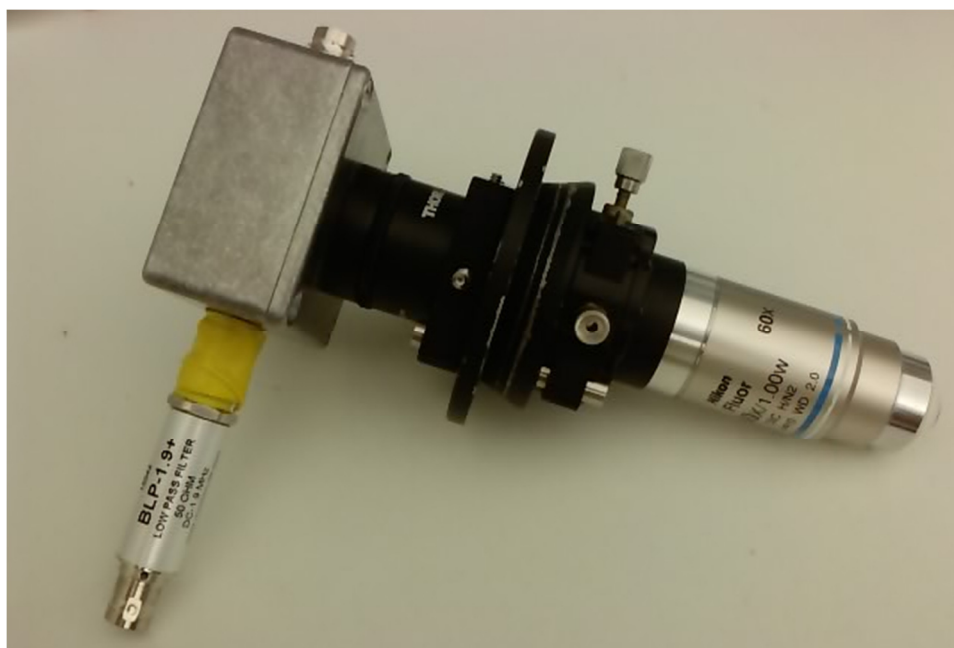


Fig. 4.5 Custom-built SRS detector.

4.3. Spectrometer

CARS spectra were obtained using the same setup as described for CARS imaging, except with a spectrometer (Andor Technology, Shamrock sr-303i) with a 303 mm focal length, coupled to the Olympus microscope. The signal from the sample was collected in the epi-direction and spectra were recorded using a CCD camera (Andor iDus). The grating chosen for our experiments was the one for which the blaze (the wavelength at which the diffraction grating works most efficiently) was optimal for the wavelength range being investigated. This grating had 150 lines/mm, 800nm blaze and a dispersion of 21.4 nm/mm. The relative quantum efficiency of this grating as a function of wavelength is given in Fig. 4.6.

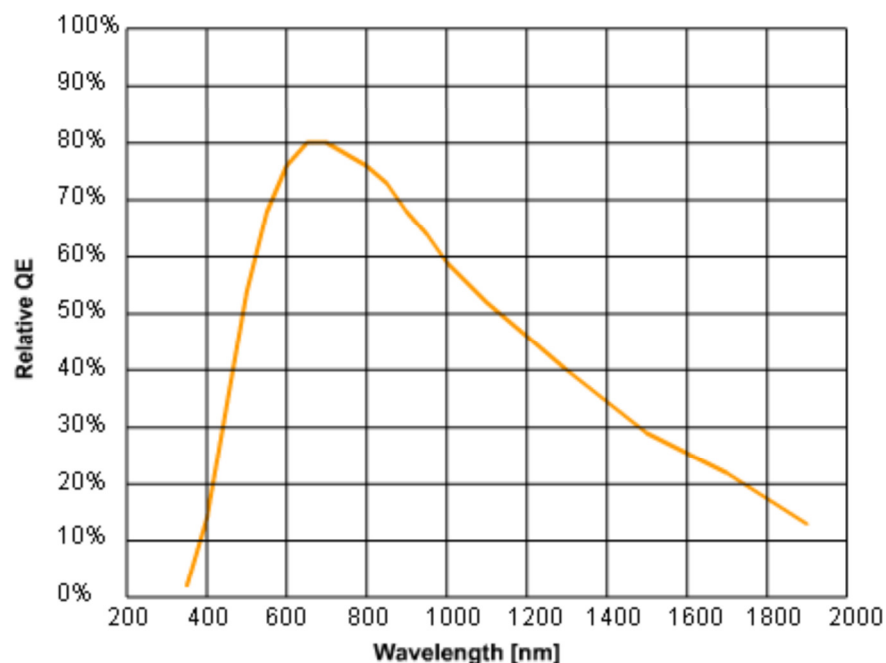


Fig. 4.6 Transmission of the grating in CARS spectrometer, data supplied by manufacturers.

4.4. Metal Evaporators

The metal-coated samples used in Chapter 5 were prepared using a thermal metal evaporation method. Two evaporators were used, a separate one each for silver and gold evaporations, both of which were assembled by members of the technical workshop at the University of Exeter. The principle behind the operation of these two evaporators was to heat a quantity of metal suspended on a conducting filament or tray (a “boat”) in a vacuum by passing an electric current through the boat, causing it to heat sufficiently to allow controlled evaporation of the metal. The filament (or boat) was typically made from W or Mo, metals which have much higher melting points than those which are to be evaporated. For both evaporators, the mains electricity supply was connected to a step-down transformer to allow currents of up to 100 Amperes to pass through the filament/boat. Using this technique, the maximum possible filament/boat temperature was ~ 1500 °C, which far exceeds the melting points of gold and silver, which are 1064.18 °C and 961.78 °C respectively.

The silver evaporator comprised a steel-walled cylinder connected to a turbo molecular high vacuum pump, whereas the gold evaporator used a glass bell jar connected to a

diffusion vacuum pump. Turbo pumps and diffusion pumps use high speed turbines or heated oil vapours respectively, to impart kinetic energy to gas molecules, hence enabling their removal from the system. In both setups, the thickness of metal deposited was monitored using quartz crystal thickness monitors. Since the oscillating frequency of the crystal is dependent on the thickness of metal deposited, by electronically measuring the change in resonant frequency of the crystal, the thickness of the metal film may be inferred. To calibrate the system, after every 10 evaporations, or when 500 nm metal had been deposited (whichever occurred soonest), 100 nm metal was evaporated onto an optically flat surface and its thickness was verified using atomic force microscopy. The calibration factor was then used in subsequent evaporations, until the next calibration took place.

4.5. Scanning Electron Microscope

To characterise the nano-structures used in this thesis, scanning electron microscope imaging was undertaken using a computer-operated Hitachi S-3200N SEM (Japan). The instrument has a large specimen chamber with a back-scattered electron detector. Samples are mounted on a platform within the specimen chamber, which is pumped down to vacuum. Imaging of back-scattered electrons takes place while a tungsten filament provides an electron probe which is scanned across the metal-coated sample. The movement range of the stage is 80 mm x 40 mm, and the image resolution is 3.5 nm in the high vacuum mode of operation, 5.5 nm in the low vacuum mode. The magnification range with this instrument is 20 – 300,000 x.

4.6. Ultraviolet Curing System

An ultraviolet curing system was used in Chapter 5 to enable samples to be affixed to glass microscope slides using ultraviolet-curing glue. The system used was an EXFO (formerly EFOS, Ontario, Canada) Novacure N2001-A1, employing a double-branched light guide to transmit light from a mercury vapour short arc lamp to the sample, delivering intensities of up to 20,000 Wcm⁻².

The glue chosen, Norland Optical Adhesives, NOA68 was selected for its ability to withstand prolonged exposure to acids and other liquids, without losing adherence to glass, as well as being able to maintain integrity under vacuum and exposure to the high temperatures within the thermal evaporation chamber during metal deposition. NOA68 is a clear, colourless viscous liquid photopolymer that cures under exposure to rapid UV light; typical curing times used in this thesis were in the range of 20 – 40 seconds, depending on the thickness of the glue used. After curing, the glue is aged at 50°C overnight to promote covalent bond formation between the glue and the glass, thus reducing the likelihood of the sample separating from the glass slide.

4.7. Cell Culture

Experiments requiring the use of live cells in this thesis made use of equipment in the cell culturing laboratory at the University of Exeter's Biomedical Physics group. This included a Faster BH EN2003 laminar flow hood, which was used to provide a sterile environment in which to transfer and replace liquids in cell cultures, and a Heraeus Instruments function line incubator which was connected to a CO₂ supply to provide a 5% CO₂ atmosphere warmed to 37 °C in which the cell cultures were kept. The incubator atmosphere was kept humidified by a pan of water with CuSO₄ dissolved therein. The CuSO₄ in the water pan was added for its properties as an anti-microbial agent. Other steps taken to prevent cell infection included removal of condensation from within the incubator on a daily basis, and cleaning of the incubator and floor hood on a fortnightly basis.

Cells were cultured in standard plastic sterile cell culture flasks with filtered caps and canted necks, with culture areas of 25 cm² (T25, Fisher Scientific) or 75 cm² (T75, Fisher Scientific). For multiphoton imaging of the cells, the cultures were seeded onto either single poly-D lysine coated glass coverslip-bottomed plastic dishes designed for use with inverted microscopes (Fluorodish, WPI instruments) or 24 well plates based on a similar design but supplied uncoated (MatTek Corporation) at least 24 hours prior to experimentation. The time delay was required to ensure maximum adherence of cells to the coverslips.

5. Surface Enhanced Raman Scattering Using Biological & Biomimetic Nanostructures

THIS CHAPTER GIVES AN account of experiments performed using a novel model SERS protein assay technique designed for aqueous samples, using metal-coated nanostructured butterfly wings and their biomimetic analogues as substrates. Insect wings, particularly those of butterflies, frequently exhibit complex nano-structured features. The experiments that follow examine the possibility for exploiting such structures to produce more effective SERS substrates than those made using standard production methods, such as electron beam lithography. In section 5.1 of this chapter, the established methods for SERS in the socially and scientifically important field of protein assaying are described, together with their advantages and limitations. In section 5.2 the experimental methods employed to prepare and characterise SERS substrates using butterfly wings biomimetic nano-structured arrays are described. Results obtained from scanning electron microscopy of the samples used are given in section 5.3. together with the enhancement factors, bio-conjugation and assaying results. The potential applications and impact of this work are discussed in section 5.4.

The metal-coated wing SERS substrates examined in this chapter were found to allow detection of protein binding events over a hitherto unprecedentedly large concentration range, which makes them viable alternatives to more common methods for assaying. Previously SERS substrates have required desiccation of the sample. These experiments represent an important advancement in the field, enabling hydrated biological samples to be examined with SERS for the first time.

5.1. SERS Protein Assays

Recently, several reports have demonstrated the potential of Surface Enhanced Raman Scattering (SERS) as a label-free readout for monitoring protein binding events [19, 37,

70] . The potential for low detection limits and higher sensitivities available with SERS have been exploited in recent biological assay research, [68, 139, 140] but this has been limited by the irreproducible enhancement provided by the substrates available for aqueous experiments, such as colloidal metals. Due to the requirement for conjugation of colloidal metallic particles to give substantial enhancements and the change of enhancement with aggregation, colloidal-based SERS methods are not reproducible, and metallic particles are prone to settling out of suspension during scanning.

Many available SERS substrates require the analyte to be deposited and dried prior to scanning. This is unsuitable for most biological analytes, such as proteins, since the process of desiccation alters their configuration and hence their Raman spectrum [141]. Drop-coated deposition has been claimed to produce un-enhanced Raman spectra of proteins analogous to those obtained from aqueous proteins [142] by providing a “natural” environment. However, with protein structure being strongly dependent upon the hydration of the molecule, it is essential that aqueous conditions are maintained in order to perform rigorous investigation of biological proteins. Protein binding systems are complex interactions which require optimal protein structure for binding to occur. Variation in pH, hydration and temperature can have an adverse effect on protein structure, thus preventing binding events which can lead to a dramatic reduction in the detection threshold [38].

SERS assays using proteins have traditionally required highly complex systems with multiple interactions to produce a detectable event [19, 37], usually with colloidal noble metal particles or a SERS chemical label providing the means of detecting binding events. These assays can provide high sensitivity to low levels of analyte in solution, but the interaction of metal colloids and chemical SERS marker molecules has the potential to adversely affect the biological molecules of interest. Intricate multiple-stage assays are undesirable for complex biological systems, where assays are required to be highly robust if they are to be of use. More cutting-edge assays have used dielectric-core metal-coated nanoshells bio-conjugated to antibodies [19, 143-145]. These assays produce excellent sensitivity combined with low levels of undesired biological interaction between the label and the analyte. However with the nanoshells free in solution, SERS spectra can be difficult to reproduce unless the analyte is spun

down using centrifugation or immobilized in some manner; these processes can be damaging to some biological samples.

The ideal substrate for SERS would provide highly reproducible SERS enhancement factors of the order of 10^6 or higher. Other requirements include the ability to perform rapid SERS biological assays whilst the samples are hydrated, which are sensitive over a range of concentrations that are comparable with ELISA and other highly sensitive assaying techniques, as discussed in Chapter 1. A principle challenge to providing these qualities in a SERS substrate is designing a suitable nanostructure that is not prohibitively expensive to produce or use in high through-put applications. The nanostructured biological features found in nature are potential sources of inspiration for such SERS substrates.

Scientists in a broad variety of fields exploit various forms of nanostructures inspired by nature [146]. Naturally occurring nanostructures that have evolved for functions involving visual appearance have been the subject of a remarkable surge in research interest [147-151]. This has built upon a range of somewhat earlier studies [152, 153]. Numerous insects, birds and plants exhibit a wide array of complex periodic and quasi-periodic ultrastructure. Their nanostructures can contribute to many biological functions: highly unsaturated colour appearances for short or long range conspecific communication [154, 155]; angle-independent colour [156] and specular or diffuse broadband appearances [157] for specialised camouflaging; linearly [155] or circularly polarised reflection [158] for high-level communication, represent a few of these.

A recent investigation into the optical properties of cicada wings found that the “quasi-periodic” nanostructured anti-reflective coating on the chitinous wing surfaces provided an excellent SERS substrate, with enhancement factors of approximately 10^6 [74]. Given the wide range of possible structures on the vast array of species of insect found in nature, it is reasonable to assume that other species could be used for the purpose of SERS. The particular species of butterfly investigated in this chapter was pre-selected for investigation based on a preliminary study of its wing surface. This chapter demonstrates that conical cuticular nanostructures found on the metalized surface of the purple and blue regions of the *Graphium weiskei* butterfly (Fig. 5.2) display

excellent properties for highly biocompatible protein assaying using SERS. A model protein binding system analogous to antibody/antigen binding using avidin and biotin was chosen for the initial SERS protein assay.

Avidin and biotin may be conjugated to a variety of proteins and are used as the basis for many immunoassays because they are well characterized, have high specificity and an almost unparalleled binding strength [159-161]. The metal coated wing substrates were found to provide Raman enhancement of proteins bound to their surface, even when kept under a droplet of saline. This prevented denaturation of the proteins due to dehydration and hence these substrates exhibit a high degree of compatibility with biological proteins. Synthetic replicas of these nanostructures can be produced by a simple application of reactive ion etching, a process which is adaptable, tuneable and suitable for economical large scale fabrication. These biomimetically conceived substrates exhibit equally sensitive surface enhancement and biocompatibility to the wing substrates.

5.2. Materials and Methods

The SERS enhancement factors were ascertained using self-assembled thiophenol monolayers as a well-defined model system, a schematic diagram of which is given in Fig. 5.1. The biocompatibility of the butterfly wing substrates was demonstrated by obtaining SERS spectra of avidin glycoproteins bound to the functionalised metal surface whilst under aqueous buffer. To show the potential application of these substrates for detection of low concentrations of analyte, a reproducible wet binding assay was undertaken with varying concentrations of biotin in solution.

All glassware was cleaned with aqua regia (concentrated hydrochloric acid mixed with concentrated nitric acid in a 3:1 ratio), rinsed exhaustively with nanopure water (PURITE, Oxford, UK) and subsequently rinsed with absolute ethanol and dried under nitrogen prior to use. Aqua regia was selected for its ability to dissolve noble metals, in addition to removing virtually all other surface contaminants.

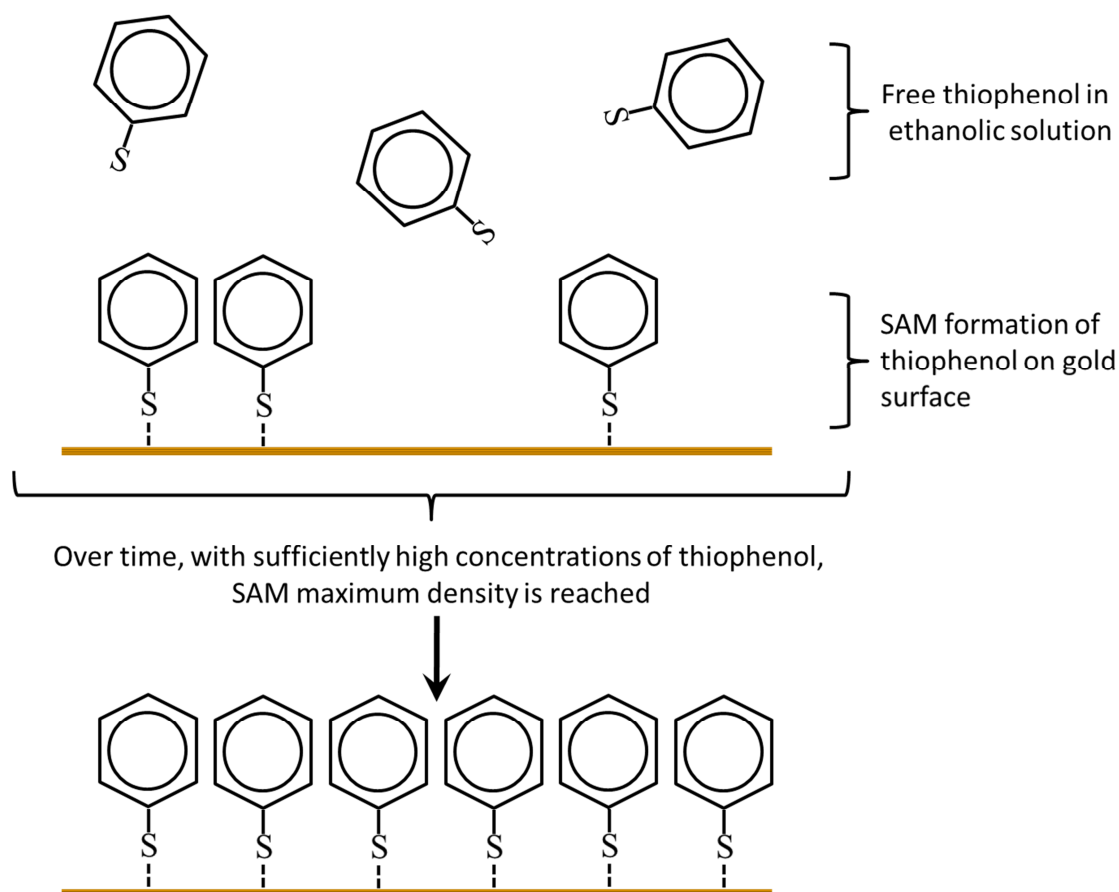


Fig. 5.1 Schematic diagram illustrating the formation of a self-assembled monolayer (SAM) of thiophenol on a gold surface.

5.2.1. Preparation of natural nanostructure substrates

A variety of naturally occurring nanostructures were investigated previously in a preliminary study by researchers at the University of Exeter, including butterfly and moth wings. Of the structures studied, male *G. weiskei* butterfly wings were found to be the most promising, on the basis of SEM characterisation of the wing surface and initial SERS enhancement factor analysis.

G. weiskei were purchased from World Wide Butterflies Ltd (wwb.co.uk). The *Graphium* wings exhibited a variety of colours, including brown, green, purple, blue and pink, as shown in Fig. 5.2. SEM images of the wings were taken in order to characterise the nanostructures in each region. Sections of the wings selected for use as SERS substrates were dissected and cut into 2mm x 2mm sections.

Various adhesives for fixing the wing sections to standard glass microscope slides were investigated, including cyanoacrylates and epoxy resins. The suitability of the glues' adhesion to glass was determined by testing their robustness against immersion in acidic and alcoholic solutions for two hours. The most appropriate adhesive was found to be Norland Optical Adhesive (Cranbury, USA), which did not peel from the glass slides, unlike the other glues tested.

To fix a wing section to a cleaned glass microscope slide, ~ 20 μL optical adhesive was applied to one end of the slide and allowed to spread out into a droplet ~ 1 cm in diameter. Using tweezers, each wing section was then carefully placed onto the adhesive droplet (nanostructured side uppermost). In order to prevent air bubbles forming underneath the wing section, care was taken to ensure that it was deposited smoothly. The optical adhesive was then cured using a UV spot curing system (Novacure, USA). A ring of optical adhesive was then rapidly applied around the wing section and cured immediately, forming a "well" around the wing section.

The prepared slides were kept in an incubator at 50°C overnight to facilitate covalent bonding between the glass and the adhesive. The wing sections on the slides were cleaned of dust and other surface contaminants by repeated immersion in ethanol followed by drying under nitrogen. A continuous film of either gold or silver (99.999% purity, GMBH) was then thermally evaporated over the wing surface at 10^{-6} mBar using a custom-built resistance heated vacuum thermal evaporator as described in Chapter 4, at deposition rates of between 1.0 nms^{-1} and 0.5 nms^{-1} . When examined using SEM and white light microscopy, the high temperatures required to evaporate the metal were not found to be sufficiently high to damage the wing sample nor distort its surface.

The thickness of the metal films and the deposition rates were monitored using a quartz crystal microbalance, and were later verified using atomic force microscopy (Ntegra NT-MDT, Russia). Various metal thicknesses were investigated, ranging from 10 nm – 100 nm. Metal thicknesses under ~15 nm were found to produce layer that were not continuous, whereas metal thicknesses of 20 nm and over were continuous. For protein binding experiments, a continuous layer of metal is required, to provide a stable surface